Colloidal Suspensions in Shear Flow

a Real Space Study

Colloidal Suspensions in Shear Flow

a Real Space Study

Colloïdale suspensies in afschuifstroming

Metingen in de reële ruimte

(met een samenvatting in het Nederlands)

Proefschrift

ter verkrijging van de graad van doctor aan de
Universiteit Utrecht op gezag van de rector magnificus,
prof. dr. W. H. Gispen, ingevolge het besluit van het
college voor promoties in het openbaar te verdedigen
op woensdag 27 september 2006 des namiddags te 12.45 uur

door

Didi Derks

geboren op 29 augustus 1978 te Oploo

Promotor: Prof. dr. A. van Blaaderen

Co-promotor: Dr. A. Imhof

Cover: Sheared colloidal crystal (front), colloidal gas-liquid interface (back), lay-out by Olivier Neijboer & the author.

This work is part of the research programme of the 'Stichting voor Fundamenteel Onderzoek der Materie (FOM)', which is financially supported by the 'Nederlandse Organisatie voor Wetenschappelijk Onderzoek (NWO)'.

ISBN-10: 90-393-4347-0
ISBN-13: 978-90-393-4347-0

Subject headings: colloidal suspensions / shear flow / confocal microscopy / shear melting / interfaces under shear / phase separation under shear.

Printed in the Netherlands by Labor Grafimedia b.v. − Utrecht

Contents

1

Introduction to Flowing Suspensions

“Everything flows ($\pi\alpha\nu\tau\alpha$ $\rho\epsilon\iota$), and nothing stands still”: This wisdom was spread by the Greek philosopher Heraclitus around 500 BC, and certainly applies to the following. In the limited world covered by this thesis, $\pi\alpha\nu\tau\alpha$ refers to a variety of colloidal suspensions that have the common property to consist of (sub)micron sized particles suspended in a continuous molecular medium. Flow ($\rho\epsilon o\varsigma$) can easily change the microstructure of these soft matter systems, and it is the aim of the current work to find out in what way.

Particles (or droplets) are classified as colloids purely based on their size, and can consist of any type of material. They fill the size range between atoms and molecules, which are smaller, and granular materials, like sand grains, which are larger. The main characteristic of colloids is the diffusive motion they perform when suspended in a molecular liquid. This random motion was for the first time observed by the botanist Robert Brown in 1828, who was investigating the pollen of plants with an early light microscope. To his surprise, he saw that those seeds were constantly in motion. He made sure that this was not due to convection or any other flow present in his sample, and was even more astonished when he pulverized several types of rocks and observed that this inanimate material was moving as well [1]. Eighty years later, Albert Einstein solved the mystery of this ‘Brownian’ motion. He showed that the diffusion of colloids is caused by many impacts of the surrounding molecules which are several orders of magnitude smaller [2]. For bigger objects these collisions nearly average out to zero, but colloids are small enough to experience a net momentum transfer, resulting in the typical random walk as was described by Brown. All this motion is caused by thermal energy: Small, fast moving, molecules are in thermal equilibrium with the big, slow, colloids.

Thermal motion is essential for colloidal systems, since it drives them to equilibrium structures, in analogy to molecular systems. Colloidal suspensions exist in many varieties and their properties can for a great deal be attributed to the size, shape and charge of the particles, and can further be tuned by additives like salt or polymers [3]. Thanks to the many control parameters, colloidal phase behavior can not only mimic that of molecular systems, but can even be richer, as was recently shown to be the case for binary mixtures of oppositely charged colloids [4].

Throughout this thesis, we will study model systems of colloidal suspensions consisting of monodisperse particles. In general, these particles may interact in several ways. For instance, there are Van der Waals attractions arising from interactions between fluctuating dipoles. The interaction strength is related to the refractive index (or dielectric constant) contrast between colloids and dispersion medium. Furthermore, electrostatic repulsions are present in systems of equally charged colloids. The range over which these charged particles interact depends on the concentration of (micro-)ions in the system. These ions screen the charges on the particles, and their concentration determines the ‘softness’ of the interaction potential. In watery systems, the electrostatic repulsions stabilize the colloidal suspension against aggregation. In apolar systems, in which colloids carry less charge, colloidal stability is achieved by covering the particle surface with polymer chains. The overlap of these polymer ‘hairs’ of two almost touching particles then causes a steric repulsion, that keeps the particles apart.

In this Chapter, we will first introduce the three colloidal model systems that will make their appearance later in this thesis. Second, we zoom in on the preparation of the home-made plexiglass spheres that are extensively used in this work. Furthermore, we discuss the main imaging technique, i.e. confocal scanning laser microscopy, and show that effects of shear flow in soft matter are expected to occur at such time and length scales, that they are suited for studies in real space. Finally, we present an outline for the rest of the thesis.

1.1. Colloidal model systems

The trick to prepare a well-defined model system usually lies in minimizing most of the possible interactions, and focus on one type in particular. For example, to obtain a system of 'hard spheres' the Van der Waals attractions are minimized by choosing a solvent with a similar refractive index as the particles. At the same time, electrostatic repulsions are screened away by the addition of sufficient salt. The only important interaction remaining is then the steric repulsion. The properties of such system are discussed below. Subsequently, we consider systems of attractive spheres, and rods.

1.1.1. Hard spheres

In hard sphere systems particles can not overlap, but do not interact otherwise. In other words, the hard sphere potential is zero everywhere, except upon touching: Then the repulsion steeply raises to infinity. For a system in which the particles also have no dimensions, the pressure p, number density (N/V) and temperature T are related through the ideal gas law: $pV = Nk_BT$, with k_B the Boltzmann constant. In an attempt to adjust this equation of state for hard spheres one should, instead of the whole volume V, only take into account the volume available (to insert a new particle). This available, or free, volume is smaller than V, because the present particles exclude part of the space for others (see Fig. 1.1). At low volume fraction the total excluded volume is directly related to the size and the number of particles. At higher volume fractions the excluded volumes of individual particles overlap, which effectively leaves more free space (Fig. 1.1). It is, however, not trivial to calculate the (average) overlap volume at a certain concentration, since it depends on the specific positions of the particles, and all

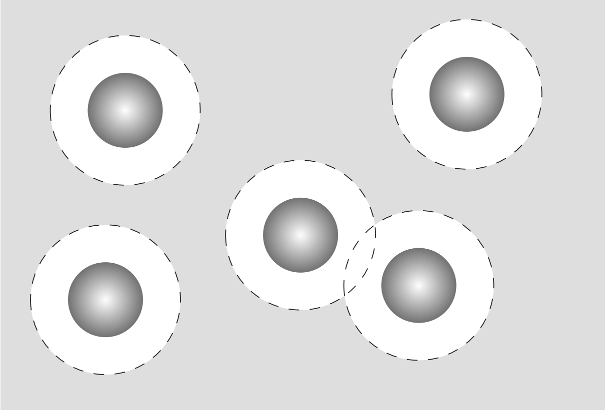

Figure 1.1. A hard-sphere system effectively gains *free* volume (light gray area) when the excluded volumes of the individual particles (white zone) overlap.

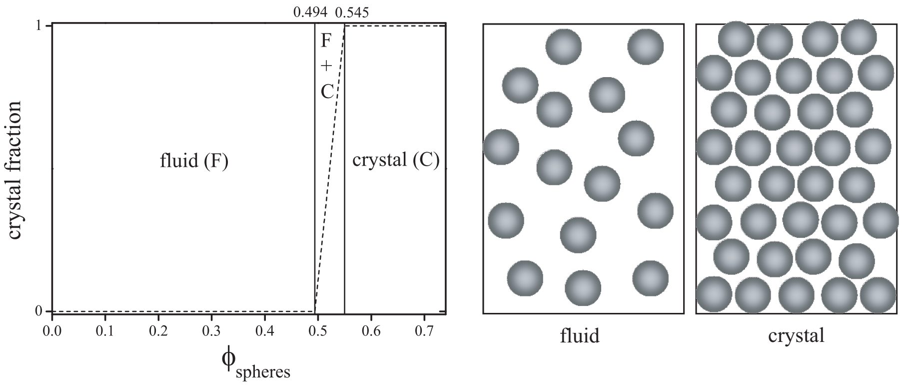

FIGURE 1.2. Phase diagram of hard spheres. Whether or not the system is ordered depends solely on their volume fraction ϕ_{spheres}. The dashed line shows the fraction of crystals in the system.

possible configurations should be considered. For this reason, even today no analytic expression for the equation of state of hard spheres exists, although good approximations are available [5, 6].

As a consequence, the first proof for a crystal-fluid transition in hard sphere systems had to come from simulations. In 1957, both Wood and Jacobsen [7] and Alder and Wainwright [8] showed that systems with repulsive interactions alone could indeed display an order-disorder transition. The transition is driven purely by entropy: Particles gain free volume, and lower the free energy, by organizing themselves in ordered arrays. In 1968, when more more powerful computers had become available, Hoover and Ree obtained accurate values for the freezing and melting volume fractions [9]: $\phi_{\text{freezing}} = 0.494$ and $\phi_{\text{melting}} = 0.545$. At intermediate concentrations both phases coexist (see Fig. 1.2).

Experimental confirmation for this phase behavior came in 1986. At that time, Pusey and Van Megen realized a system of (nearly) hard spheres by suspending sterically stabilized plexiglass particles in an apolar, refractive index matching, solvent [10]. From then onwards, these poly(methyl methacrylate) (PMMA) spheres became more widely used in colloid science, and also scattering experiments of this system under shear were reported [11]. Nowadays, PMMA-particles are well-established as model (hard) spheres, and also play a key role in this work.

1.1.2. Attractive spheres

Molecular systems usually display a richer phase behavior than the hard sphere systems discussed before. Water, for example, can exist as vapor, (liquid) water or

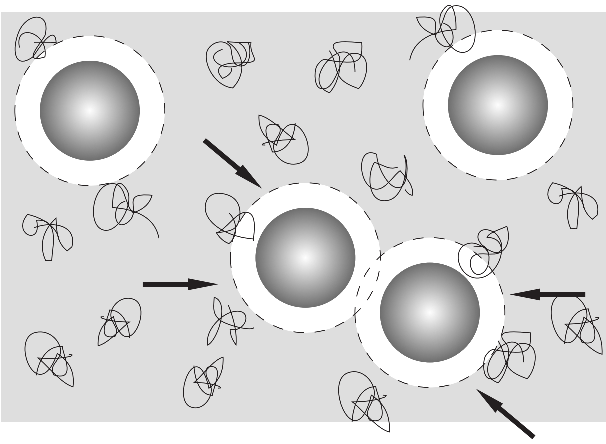

Figure 1.3. The depletion attraction between colloidal spheres. Each colloid excludes part of the volume for polymers (white area). Overlap of these depletion zones increases the *free* volume (light gray area) for the polymer.

ice. Both in the vapor and liquid the molecules are disordered and the phases only differ in density. Attractions are essential for the fact that those two disordered phases can exist next to each other. The molecular attractions arise from dipole-dipole interactions. Apparently, at certain circumstances, the system finds its lowest free energy by splitting up into dense phase (liquid) and a less dense phase (gas). Although colloids can also interact via (induced) dipole interactions, we have in these systems a much easier tool to control the strength and the range of attraction. The addition of (non-adsorbing) polymers induces an attraction between two colloidal particles, or two parallel plates, as was first demonstrated by Asakura and Oosawa [12], and later by Vrij [13].

In the most simple description of a colloid-polymer mixture, the colloidal spheres interact as hard spheres, while the tenuous polymer coils are allowed to overlap. The interaction between a polymer and a sphere is again hard sphere like: A polymer chain can not penetrate a sphere. This means that around each sphere there is a zone from which the polymer is depleted (see Fig. 1.3). When colloids come so near that their depleted zones overlap, polymers can not enter the region in between anymore. This causes an osmotic pressure difference that pushes the particles further together. So, though there are still only repulsions present in the system, the spheres *effectively* attract. This depletion attraction is thus a purely entropic effect. Another way to see why it is favorable for two spheres to come

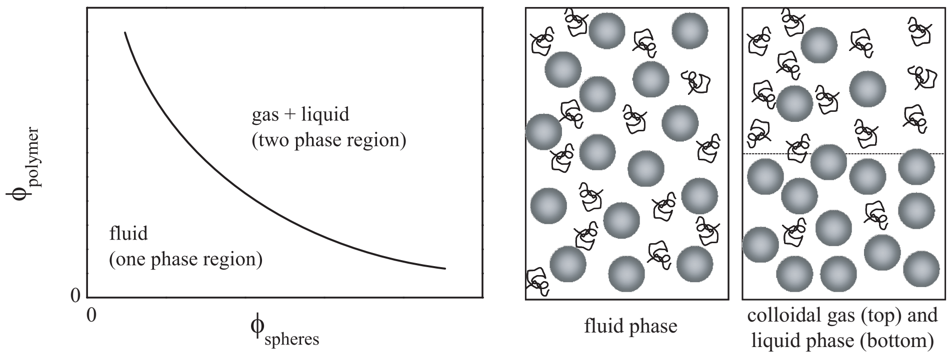

fluid phase

colloidal gas (top) and liquid phase (bottom)

FIGURE 1.4. Schematic phase diagram of colloid-polymer mixtures. At low concentrations of colloids and polymers one phase is observed. At higher concentrations the system splits up in a phase with many colloids and few polymers (colloidal liquid) and a phase with a lot of polymers and few colloids (colloidal gas). Though not indicated, a (hard sphere like) freezing transition is expected at higher colloid volume fraction.

together, is by realizing that when the depleted zones overlap, the polymers gain free volume. In finding the most stable state the system may therefore split up into a colloid rich (polymer poor) phase and a colloid poor (polymer rich) phase.

Whether or not the depletion attraction can lead to phase separation depends on strength and range of the attraction. Phase separation into colloidal liquid and colloidal gas occurs if the interaction strength between the spheres is of order $k_B T$, and its range lies in the order of the colloidal diameter. In Fig. 1.4 we sketch the phase diagram of a system with such interaction potential.

The typical strength of the attraction ($k_B T$) together with the colloidal length scale (R) are also responsible for the ultra low interfacial tension σ associated with colloidal gas-liquid interfaces: $\sigma \propto k_B T/R^2$. The interfacial tension in colloid polymer mixtures is typically a million times smaller than in molecular systems.

For this thesis, a system of attractive spheres is realized experimentally by preparing a mixture of poly(methyl methacrylate) colloids and non-adsorbing poly(styrene) in the apolar solvent decalin.

1.1.3. Rods

Suspensions of colloidal rods are known to show a transition from an isotropic to a nematic state, when exceeding a certain particle concentration. In the isotropic phase particles are randomly oriented, while in the nematic phase they are aligned. What drives the isotropic to nematic phase transition is the fact that rods can gain

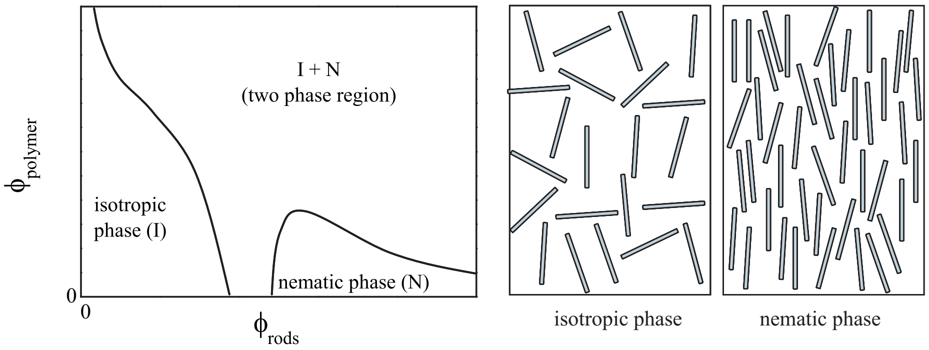

Figure 1.5. Schematic representation of the phase diagram of rod-polymer mixtures. In the sketch of isotropic and nematic phase only the rods are shown, polymers are left out.

translational freedom by giving up part of their orientational freedom, when they align in a nematic phase. The isotropic to nematic transition occurs already at low volume fraction of rods, since a long thin rod will exclude a volume, much larger than its own, for other rods. The larger the aspect ratio (length over diameter), the lower the volume fraction at which the transition occurs. Theoretically, the phase behavior of hard rods was already derived by Onsager in 1949 [14]. Later, the theory was extended for semi-flexible rods though the ideas stay basically the same.

Like in the sphere suspensions discussed before, non-adsorbing polymers effectively induce attractions between rods. The attraction range is determined by polymer size, and can lead different phase diagrams [15]. In the simplest scenario, the phase behavior is basically the same as for hard rods, with the only difference that the coexistence range, where both the isotropic and nematic phase are present, is broadened (Fig. 1.5). Our experimental rod suspension, consisting of *fd*-virus to which dextran is added as a polymer, displays this kind of phase behavior. In case the polymers would have been smaller, or larger, an additional coexistence region of two types of nematic, or two types of isotropic phases, respectively, would have been observed. In addition, more ordered phases, such as smectic phases, are also possible.

1.2. The art of making colloids: The chemistry

For our studies it is important to have at our disposal model systems that are highly monodisperse. In nature, nice examples of (reasonably) monodisperse colloidal systems can be found. For instance, one can think of natural opal, which consists of ordered arrays of equally sized colloidal silica spheres. Popular examples from the field of biology are DNA or viruses. The rod suspensions we just introduced consist of *fd*-virus ($L = 880$ nm, $d = 6.6$ nm, with a persistence length of 2.2 μm). These rods are produced by first growing a colony of *E-coli* host bacteria, which are subsequently infected by the virus. The virus then reproduces itself at the expense of its host [15].

Another route to obtain colloidal systems with the desired properties is via chemical synthesis. One of the first procedures to obtain monodisperse colloidal spheres was introduced by Stöber *et al.* in 1968 [16]. They presented a straightforward way to produce monodisperse silica spheres from a mixture of tetraalkoxysilanes, ammonia, alcohol and water. This method can produce particles in a size range from 50 nm to 2 μm, and became the method of choice. Silica colloids can be coated with an extraordinary wide range of chemicals. This makes it possible to disperse them also in apolar solvents and to tune their interactions. For the preparation of colloidal systems in the apolar solvents the work of Antl and co-workers has also been of great importance [17]. In this basically single step method, poly(methyl methacrylate) (PMMA) spheres were synthesized via a dispersion polymerization reaction. By a slight modification of the procedure one can also obtain fluorescent spheres [18], that are highly suited for studies with confocal microscopy. Furthermore, the PMMA-spheres have the advantage that not only their refractive index can be matched to the dispersion medium, but their density as well. The latter motivates our choice for PMMA-particles, since in our microscopy study we need to avoid sedimentation in systems of large spheres (diameter > 1 μm) to keep an homogeneous volume fraction.

The initial reaction mixture contains methyl methacrylate monomers (MM) dissolved in an apolar solvent in the presence of a graft copolymer built up by MM-backbone with poly(12-hydrostearic acid)-chains, that will stabilize colloidal particles as soon as they are formed. The concentration of monomers is high, typically about 40 weight percent. When the temperature is raised, the unstable compound azo-bis-isobutyronitrile (ADIB) that is added in a small quantity, dissociates, and initiates a radical polymerization reaction of the methyl methacrylate monomers. As the MM-chains grow longer, their solubility decreases, and at a certain stage the polymers collapse into solid particles. For obtaining equally sized particles, it is important that this nucleation occurs in a short time interval. After nucleation, the particles continue to grow further, till all the monomers have reacted. During this diffusion limited growth, and after, the graft copolymer stabilizes the particles against aggregation. The stabilizer is an important component for the PMMA-synthesis, and needs to be prepared beforehand.

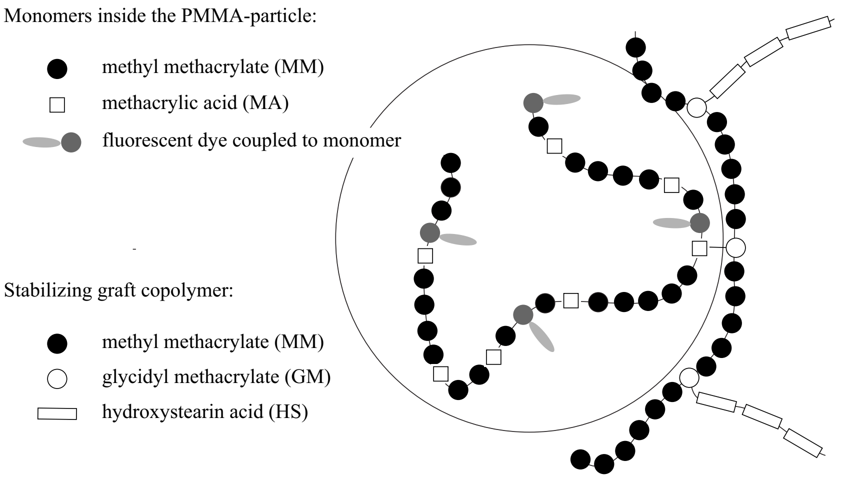

Figure 1.6. Composition of a poly(methylmethacrylate) (PMMA) particle [18]. The polymer mainly consists of units of methyl methacrylate, with occasionally a monomer with an attached fluorescent dye, and a methacrylic acid unit, which can be chemically coupled to the graft copolymer in a separate step. The side chains of this polymer, poly(12-hydroxystearic acid) (PHS), sterically stabilize the particles.

Initially, the stabilizer is physically adsorbed to the particles. Adding a small fraction of methacrylic acid (MA) during the polymerization reaction, allows to chemically attach the stabilizer chains to PMMA-particle in a next step (Fig. 1.6). This so-called locking makes further handling of the colloids easier, since the stabilizing PHS will stay on the particle surface, also when the colloids are (many times) transferred to different dispersion media. Thanks to the sterical stabilization, it is also possible to store the PMMA colloids in a dried form, as powder, and to redisperse them later in the desired solvent.

An elegant way to make fluorescent PMMA particles is to chemically incorporate a dye in the polymer chain. This can be done by preparing fluorescent monomers beforehand. Different dyes can be incorporated. For the systems used in Chapters 2 and 3, rhodamine-B-isothiocyanate was first coupled to aminostyrene. The reaction takes place in ethanol, and occurs immediately. The styrene group in the resulting rhodamine-amino-styrene (RAS) copolymerizes with the methacrylate monomers. Rhodamine labeled particles appear pink and can be excited either with the 543 nm line of a helium-neon laser, or the 567 nm line from an argon krypton laser. To obtain (yellow) particles that can be excited with the argon laser line of 488 nm, the fluorescent monomer NBD-MEAM (4-methylaminoethylmethacrylate-7-nitrobenzo-2-oxa-diazol) can be incorporated [18].

Almost all particles used in this thesis are produced in a single step process that results in fully labeled particles. However, it is possible synthesize more advanced core-shell particles, in which only the core is fluorescent [19]. In order to keep the particles core-shell, it was required to fix the polymer chains inside the particle: Otherwise, the diffusion of the polymer chains eventually spreads the dye over the whole particle volume. This was achieved by a constant well-proportioned addition of the cross-linking monomer ethylene glycol dimethacrylate (EGDM), which has two methacrylate groups that both participate in the polymerization reaction and connect different parts of the chain.

1.3. CONFOCAL MICROSCOPY

The major experimental technique to investigate the colloidal suspensions used in this thesis is confocal scanning laser microscopy (CSLM). The confocal microscope was invented in 1955, and patented in 1961, by Marvin Minsky [20]. Minsky's motivation to build a high resolution microscope was born at the time of his graduate studies when he, in his search to understand the working mechanism of the human brain, unsuccessfully, tried to visualize (stained) neurons. These cells are densely packed and highly interwoven, and by using a conventional light microscope Minsky encountered the problem of scattering: Light rays from points out of the focal plane transformed the outcoming image into a 'meaningless blur'.

An ideal microscope would examine each point of the sample and measure the light scattered or absorbed by that point. Minsky realized, years later, that this could be achieved by illuminating the sample point by point, instead of all at once. In addition, the light coming from out-of-focus points (that is already largely reduced compared to bright field microscopy) can be rejected by placing a pinhole just before the detector. In this way, the view is confined to a thin slice of the sample, and the signal to noise ratio is enormously improved. Minsky did not leave this as an idea, but actually succeeded in building a prototype himself. His invention remained relatively unrecognized for decades, and his ideas became accessible for a larger public only in 1988, when he was invited to write an article about it [21]. Finally, the introduction of lasers and computer controlled scanning and imaging techniques made that confocal microscopes became commercially available. At present, confocal microscopy is widely used in soft matter physics, while its main application still lies in the field of biology.

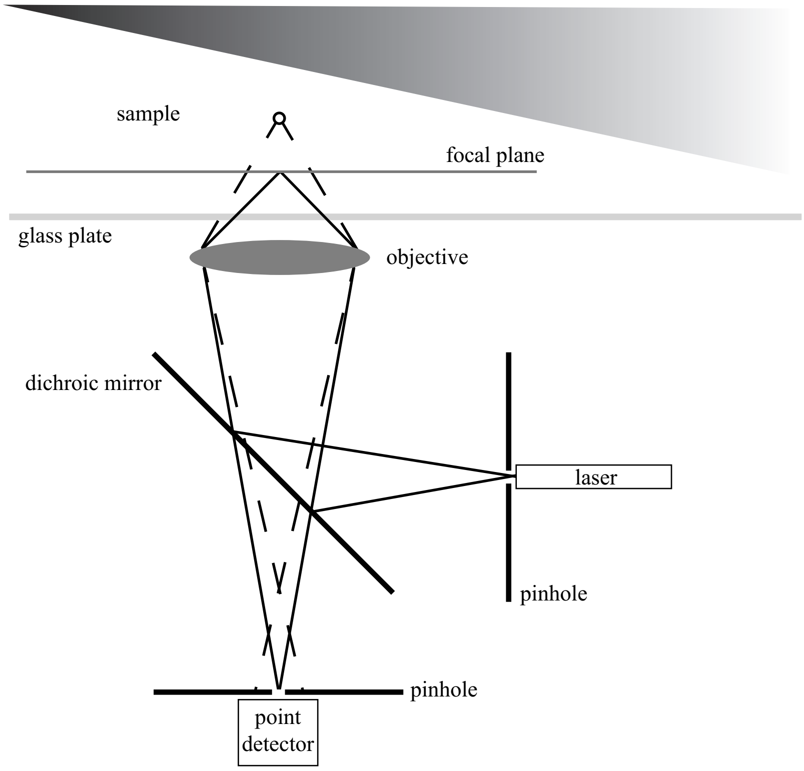

Figure 1.7. Beam path in an (inverted) confocal scanning laser microscope in fluorescence mode. The excitation beam is reflected at the dichroic mirror and focussed in a point in the sample. Emitted light from this point initially follows the same path backwards, then passes the dichroic mirror and hits the detector. Light that due to scattering was emitted from another point in the sample, will be filtered out, since most of it will not pass the pinhole in front of the detector.

Confocal microscopy can be applied in both transmission and reflection mode, but (arguably) the most powerful way to use a confocal microscope is in fluorescence mode. The quality of images then depends on fluorescence of the probes, and scattering is no longer required for seeing the objects in the first place. This allows to reduce scattering by matching the refractive index of solvent and object. This method is ideal for imaging colloidal suspensions in real space, and makes it possible to quantitatively study three dimensional colloidal systems on the single particle level. In fluorescence microscopy, the excitation and emission beam can be splitted based on their wavelength using a dichroic mirror. The beam path in a confocal fluorescence microscope is displayed in Fig. 1.7.

The in-plane resolution r of the microscope is determined by the wavelength and the numerical aperture (NA) of the objective lens: $r \propto \lambda/\mathrm{NA}$. For our study of micrometer-sized fluorescent colloids in a refractive index matching solvent ($n = 1.5$), we use high numerical aperture objectives (NA = 1.4). In combination with light of a typical wavelength of 500 nm this results in a resolution of $\sim$ 200 nm. In the vertical direction the resolving power of a confocal microscope is about 3 times lower than in-plane. This means that (fully labeled) particles larger than a micrometer, like the 1.7 μm diameter spheres we use in Chapter 3, can be resolved in three dimensions.

The price for the higher resolution in a confocal scanning microscope is paid by the time it takes to build up an image: Scanning microscopy is much slower than conventional microscopy. Recent developments in confocal microscopy are therefore mainly motivated by the wish to increase the frame rate, while keeping a high signal to noise ratio. An alternative for the scanning microscope is found in the spinning disk confocal. Here, a rotating Nipkow disk containing an array lenses depicts the all points of the image simultaneously, increasing the imaging rate with at least a factor 10. In this thesis, we make use of a scanning microscope, which in its working principle still strongly resembles Minsky's original version.

1.4. Colloids in flow

The behavior of colloids in flow is important in different kinds of applications. Common examples of colloidal suspensions are milk or paint, and the understanding of their flow behavior has impact on the coating and food industry. More fascinating applications are found in (future) high-tech products in the field of photonics [22] or microfluidics [23]. In photonics, shear can assist in fabricating large monocrystalline structures, built up by colloidal particles (size of the wavelength of light). In microfluidics, the understanding of flow of 'complex fluids' in micro-channels becomes increasingly important for the implementation of these devices in sensors and 'lab-on-a-chip' applications. Also from a fundamental point of view, the combination of colloids and flow is interesting: Due to their long length and time scales colloidal systems can easily and controllably be brought out-of-equilibrium. This might lead to both new behavior, and the understanding of already observed phenomena, like shear melting, on a single particle level.

Shear flow is a rather simple type of flow, which is characterized by only one non-zero velocity component, and a velocity gradient (= shear rate $\dot{\gamma}$) perpendicular to the velocity direction. For instance, the flow of a viscous liquid between two sliding parallel plates is such a shearing flow: The flow direction parallel to plates, whereas the gradient is perpendicular. Poiseuille flow, i.e. pressure flow in a tube, is another example. Here, the velocity gradient is directed along the tube radius. In our investigations we use a cone-plate shear cell to study flowing colloidal suspensions. The rotating cone and plate drag along the confined fluid, and set up a well defined shear flow.

The shear cell used for the measurements in this thesis is recently developed and suited to be placed on top of a microscope. The main characteristic of the cell is that the rotational velocity of both cone and plate can independently be controlled. Cone and plate rotate in opposite directions, so that at a certain height in the sample a plane is not moving. The relative speeds of cone and plane determine the height of this stationary layer. This gives the possibility to quantitatively study a sheared colloidal suspension in the bulk of the suspension.

The time constant characterizing the applied flow is given by the inverse shear rate ($1/\dot{\gamma}$). In general, the importance of shear is expressed by the dimensionless Deborah number

$$\mathrm{De} = \dot{\gamma}\tau, \tag{1.1}$$

comparing the deformation rate to the "characteristic" relaxation time of the system τ. Soft matter systems are easy to manipulate by flow, meaning that low shear rates can already have an effect, because the typical relaxation times are long.

In colloidal suspensions the applied shear is often compared to the diffusion time of the particles: When the deformation is applied slowly with respect to the Brownian relaxation time τ_B, the system has time to relax back to its equilibrium structure, and no significant change of the microstructure is expected. The Brownian relaxation time is related to the time it takes for a particle to diffuse over a distance of it own size (R): $\tau_B = R^2/D$, with diffusion coefficient $D \propto k_BT/\eta R$. More specifically, the relative importance of shear is then measured by the Péclet number:

$$\mathrm{Pe} = \dot{\gamma}\tau_B = \frac{\eta\dot{\gamma}R^3}{k_BT}. \tag{1.2}$$

When Pe exceeds unity, diffusion of particles will no longer be rapid enough to relax the shear distorted microstructure back to equilibrium. For micrometer-sized particles, the Brownian time lies typically in the order of seconds, so that this already occurs at experimentally easily accessible shear rates.

The diffusion time is not the only characteristic relaxation time in colloidal suspensions. In phase separated systems interfaces bring along there own characteristic time. The time scale connected to such an interface is not only related to the viscosity η, but also to its interfacial tension σ. One can argue that in these situations the interface will be affected as soon as $\dot{\gamma}\tau_{\mathrm{cap}} > 1$, where the $\tau_{\mathrm{cap}} = \eta L_{\mathrm{cap}}/\sigma$ the capillary time, and L_{cap} the capillary length. Capillary relaxation time and Brownian relaxation time differ especially near the critical point.

1.5. SCOPE OF THIS THESIS

In this thesis we investigate the behavior of the three model systems introduced in Section 1.1 in shear flow by means of confocal microscopy. First of all, the experimental setup will be described in detail (Chapter 2). The first experiments with this cell are presented and it is shown how flow profiles in a sheared colloidal suspension can be deduced from microscopy images. In Chapter 3, we focus our study on hard sphere colloidal crystals in shear flow. To that end, we use rhodamine labeled poly(methyl methacrylate) spheres, with a diameter of 1.7 μm. This allows quantitative investigations on the particle level. In this way, we obtain more insight in the process of shear melting.

We continue our study with slightly more complex systems: mixtures of colloids and polymers. This mixture undergoes a gas-liquid phase separation. The poly(methyl methacrylate) spheres used here are an order of magnitude smaller (50 nm and 150 nm in diameter in Chapter 4 and 5, respectively), and can not be individually resolved by confocal microscopy. However, the length scales connected to the interface are in the order of micrometers, which *does* allow quantitative microscopy investigations. We first concentrate on the demixing process under shear (Chapter 4), and then on the fluctuations on the sheared interface itself (Chapter 5).

Finally, in Chapter 6, we consider a system of colloidal rods in shear flow. Here, we use the shear flow to reach a well defined, aligned, homogeneous initial state and follow the phase separation process after quenching to zero shear. By varying the rod concentrations we obtain more information on the phase diagram of these systems. We conclude the thesis with a summary (also in Dutch).

2

The Counter Rotating Cone-Plate Shear Cell

ABSTRACT

We report on novel possibilities to study colloidal suspensions in a steady shear field in real space. Fluorescence confocal microscopy is combined with the use of a counter-rotating cone-plate shear cell. This allows imaging of individual particles in the bulk of a sheared suspension in a stationary plane. Moreover, this plane of zero velocity can be moved in the velocity gradient direction while keeping the shear rate constant. The colloidal system under study consists of rhodamine labelled PMMA spheres in a nearly density and refractive index matched mixture of cyclohexylbromide and *cis*-decalin. We show measured flow profiles in both the fluid and the crystalline phase and find indications for shear banding in the case of a sheared crystal. Furthermore, we show that, thanks to the counter-rotating principle of the cone-plate shear cell, a layer of particles in the bulk of a sheared crystalline suspension can be imaged for a prolonged time, so that their positions can be tracked.

2.1. INTRODUCTION

The relation between microstructure and flow behaviour of soft condensed matter systems has been a subject of intense research. Subtle changes in microstructure resulting from shear may lead to strong shear thinning or shear thickening behaviour. In many cases, however, shear may even lead to sudden and dramatic changes in the long range order of a complex fluid. Shear-induced structural transformations occur in colloidal dispersions, block copolymers and micellar solutions. Recent reviews can be found in Refs. [24–27]. Most information on shear-induced microstructures has been obtained with scattering measurements. It has become increasingly clear, however, that real-space observations on the length scale of the individual particles are necessary to understand these nonequilibrium phase transitions. Modern advanced microscopy techniques, such as confocal fluorescence microscopy, make it possible to study the structure and dynamics of colloidal particles in three dimensions [28–30]. Extension of these methods to colloidal dispersions under shear is expected to lead to new insights in shear-induced phase transitions that have been investigated in the past and new phenomena that cannot be so easily inferred from a k-space analysis. The former include the formation of crystalline order under oscillatory shear [31], shear melting of colloidal crystals [32], shear-banding in dispersions of spherical [33, 34] and rod-like colloids [35].

Apart from the fundamental importance of understanding structural transformations in external shear flow, further motivation is found in the great importance of shear during industrial processing of colloidal systems such as foods, paints, and emulsions. In addition, shear-induced large single crystal formation can be used to prepare new advanced materials such as photonic crystals [22, 36].

In order to apply shear in a controlled way and to study the sheared system on a microscopic level a microscope needs to be equipped with more advanced tools than is necessary for the study of the equilibrium structure and dynamics of colloidal suspensions. With the development of shear cells that can be mounted on top of microscopes, investigations in real space became possible. Recently, the effects of shear have been investigated in different types of set up. Palberg *et al.* [34] combined a plate-plate shear cell with video microscopy. The cover slip correction was adjusted such that the focusing depth was several times the interparticle spacing. This enabled them to study the distribution functions for the projections of particle positions into the flow-vorticity plane. The tracks of individual particles could not be determined in this way. Tolpekin *et al.* [37] used a rotating plate-plate cell in combination with confocal microscopy to investigate the formation and break-up of aggregates in colloid-polymer mixtures under shear.

They used desmearing by image processing to correct for effects of particle motion by the flow. They had to stop the flow in order to study the structure of aggregates in 3D. Similarly, Varadan [38] *et al.* studied colloidal gels under shear by imaging immediately after stopping the flow. Quantitative data on individual particles during flow were obtained by Hoekstra *et al.* for attractive particle systems as well as for repulsive systems, because they limited their set-up to 2D [39].

For a real space study of a 3D-system under shear the main difficulty is that the particles move through the field of view of the microscope too rapidly, making it impossible to track them, except very close to the stationary wall where the flow velocity is small enough. Although the development of faster confocal scanning techniques, for example with the use of a spinning Nipkow disc [40], can mean a big step forward, the real answer to this problem lies in the use of a counter-rotating shear cell. In this approach the two parts of the cell rotate in opposite directions, such that a stationary plane is formed in the interior. Objects in this plane can then be observed for extended periods of time. This concept was used already by Taylor to study droplet break-up during emulsion formation [41]. Recent implementations of the counter rotation concept to study the behaviour of noncolloidal particles under shear are given in Refs. [42, 43]. However, these investigations were limited to low-magnification microscopy and dilute samples.

We have used a new counter-rotating cone-plate shear cell suitable for high-magnification confocal fluorescence microscopy to study the behaviour of concentrated dispersions of micrometer sized hard-sphere like colloids under shear. By adjusting the ratio of angular velocities of plate and cone the stationary plane can be placed anywhere in the bulk. This allows us to observe microstructure and particle dynamics in the bulk of the dispersion for extended periods of time.

This Chapter is organized as follows. First we introduce the counter rotating shear cell in combination with the confocal microscope and describe the preparation of the colloidal dispersions in Section 2. Then, in Section 3, we demonstrate the instrument by measuring microscopic flow profiles in sheared colloidal fluids and particle dynamics in colloidal crystals.

2.2. EXPERIMENTAL SECTION

2.2.1. Counter rotating shear cell

The measurements were performed with the Wageningen Centre of Food Science (WCFS) continuous Shear Cell configuration [44,45]. This cone-plate shear cell was placed on top of an inverted microscope. In Fig 2.1 a side view of this setup is given, showing the essential parts of the shear cell. A schematic representation is given

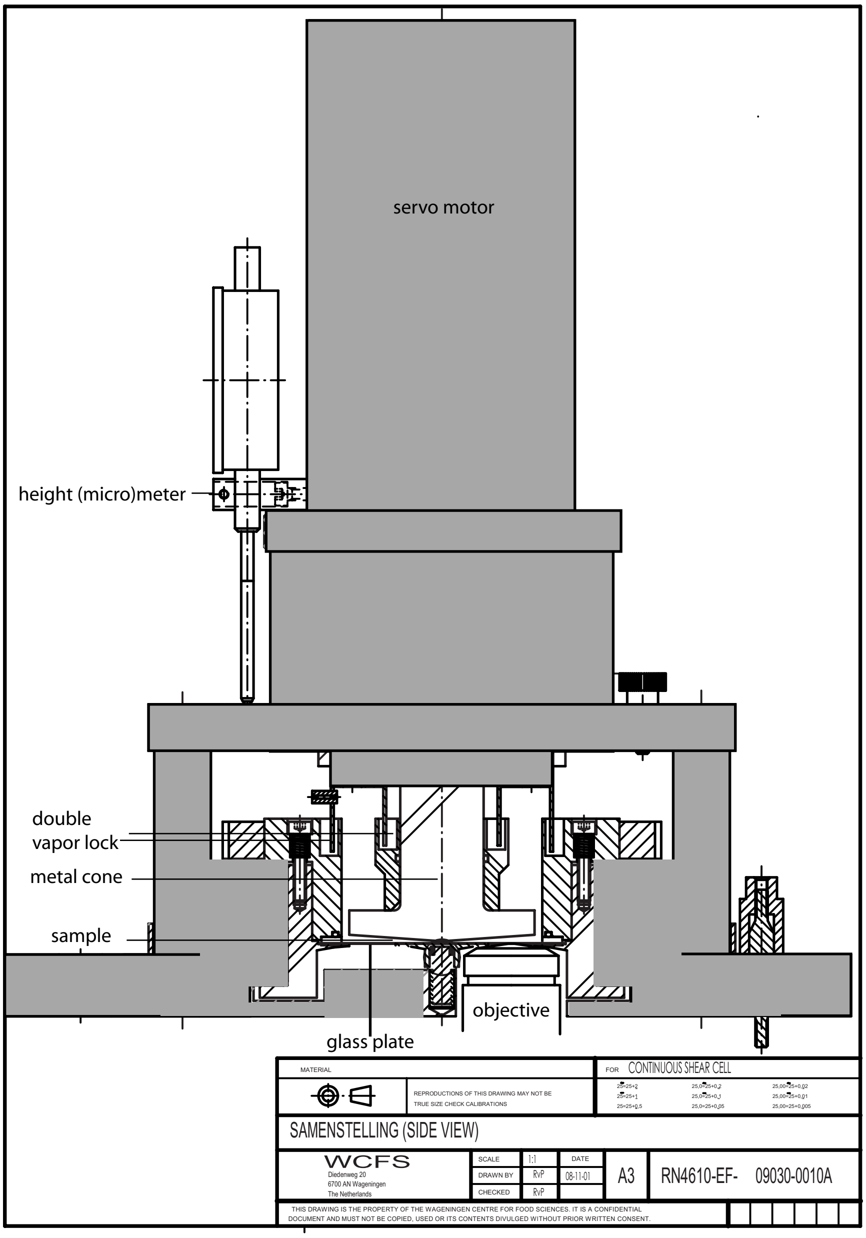

FIGURE 2.1. Side view of the WCFS Continuous Shear Cell configuration. Samples can be mounted by releasing the cone unit (including motor). Reproduced with permission of the Wageningen Centre of Food Science (WCFS).

in Fig. 2.2a. The angle β between cone and plate was 4° (±0.01°). [1] The cone and plate were driven independently by servomotors and rotated in opposite directions. The height of the stationary plane (zero velocity plane) could be adjusted by tuning the ratio of the rotational speed of the cone and the plate, while the shear rate $\dot{\gamma}$ was kept constant. A key property of a cone-plate configuration is that the shear rate is the same at all radial positions: $\dot{\gamma} = \Delta\omega / \tan\beta$, where ω is the angular velocity and $\Delta\omega = \omega_{\mathrm{cone}} - \omega_{\mathrm{plate}}$.

In this set up the radial position of the microscope objective was fixed. At this position the gap between cone and plate was 1.70 mm (±0.01 mm). The cone was made of stainless steel. The plate consisted of a circular glass slide of a diameter of 8 cm and a thickness of 180 μm. The glass plate was clamped between two Teflon rings and supported in the centre by a metal disk. The inner diameter of the cell itself was 6.50 cm. The cell was equipped with a double vapour lock. The inner vapour lock was filled with the solvent, and the outer one with water. Shear rates in a range of 10^{-2} to 10^{2} s^{-1} could be applied.

During a full rotation we measured a variation in the gap of ±10 μm. This was mainly caused by a slight wobbling of the glass plate. The wobble in the cone was measured to be only ±1 μm. This means that at typical shear rates the height of the glass plate, and thus the height of the stationary layer, fluctuates only very slowly. For example: at a shear rate of 5 s^{-1} and $\omega_{\mathrm{cone}}/\omega_{\mathrm{plate}}$ of 50 the height of the glass plate fluctuates by about 1.2 μm over a time span of 1 minute. This is slow enough to allow adjustment of the height of the focal plane if necessary.

2.2.2. Confocal microscopy and image analysis

Particle imaging was performed using an inverted Leica confocal scanning laser microscope (CSLM), type TCS-SP2. The microscope was operated in fluorescence mode. We used the 543 nm line of a green He-Ne laser for excitation of the rhodamine labelled particles (and droplets). 3D imaging was made possible by the use of a piezo-focusing drive (Physik Instrumente P-721) of the objective lens. The scanning range of this drive was 100 μm. Measurements were performed with a 100× oil immersion objective with a numerical aperture of 1.4 and a working distance of 100 μm (on top of the 180 μm thick microscope slide). The microscope allows imaging of planes parallel as well as planes perpendicular to the glass plate. In the following the velocity gradient $\vec{\nabla}$ is directed along the z-axis; the flow $\vec{v}$ is

---

[1] In a later version of the setup the cone was made replaceable, such that cones with angles β of 2° or 1° became possible as well. In this way the sample volume could be reduced from ~ 4 mL to ~ 1 mL. In addition, a larger part of the gap from cone to plate could be covered using an high NA oil immersion objective. The main disadvantage of smaller angles is the increase in relative errors, mainly caused by a slight misalignment of the glass plate.

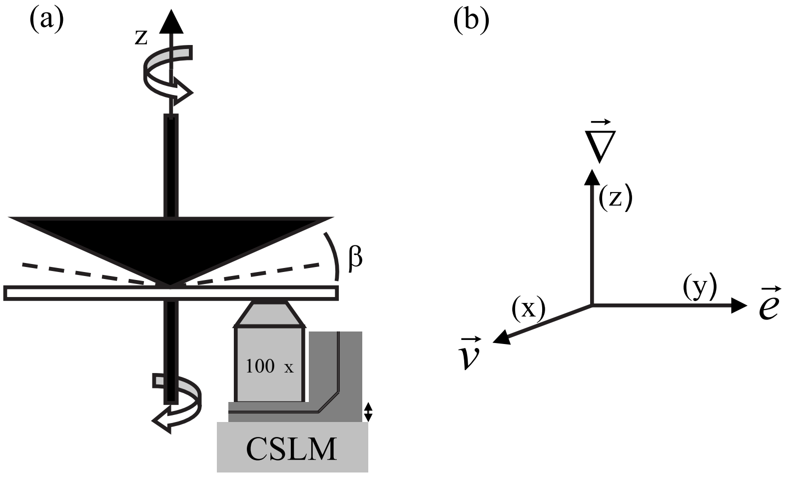

FIGURE 2.2. (a) Schematic representation of the experimental setup. A cone-plate shear cell is placed on top of an inverted microscope. The metal cone and glass plate rotate in opposite directions. The dashed line indicates the zero-velocity plane. The objective is mounted on a piezo-drive. In (b) the directions of the velocity gradient $\vec{\nabla}$, the flow $\vec{v}$ and the vorticity $\vec{e}$ are shown.

directed along the x-axis and the y-axis points into the vorticity direction $\vec{e}$ (see Fig. 2.2b).

The coordinates of the colloidal particles were found in xy-layers using similar routines to those described by Grier and Crocker. In this way the particle coordinates could be obtained with sub-pixel accuracy. In our experiments the xy-pixel size is 73 nm. The accuracy of finding particle locations is estimated to be 10 nm. The particles were tracked in time by comparing the coordinates found in every two successive frames from a time series of xy-images [46]. We used additional procedures to find velocity profiles in the shear field. Two routines were developed for measuring image drift due to the flow in time-series of images taken parallel to the glass plate (perpendicular to the velocity gradient direction).

The first method uses particle coordinates and tracks as found above [46]. Then we consider every two successive frames and select all the particles that are present in both frames. Subsequently, we calculate the difference between the centre of mass of the selected particles in these two frames. Accumulation of these differences gives again the position shift as a function of time.

In the second method to measure drift we calculate the cross-correlation function of every two successive images. This function has a well-defined maximum at the value corresponding to the average displacement of all the particles. The position of this maximum is tracked to obtain the drift averaged over all particles in the frame as a function of time.

The two methods gave very similar results but were used for slightly different purposes: the first method for measuring the exact average velocity of the particles in the plane of zero velocity, and the second method for measuring the flow profile (from time series of different layers). Note that the second method has the advantage of being faster since no particle finding is necessary.

2.2.3. Preparation of emulsions and colloidal suspensions

Emulsions were prepared by making solutions of 10 wt % fish gelatine (Multi Product) and 10 wt % dextran (MW 282,000) (Sigma) in water at 60 °C, and mixing these in a ratio 1/1 at room temperature. This way an emulsion of 10 μm sized gelatine rich droplets in a continuous dextran rich phase was obtained. Rhodamine-B (0.01 wt %) was added to the mixture which preferentially stains the gelatine rich phase [45, 47].

The colloidal particles used for this work were polymethylmethacrylate (PMMA)-spheres prepared by dispersion polymerisation [17]. The spheres were sterically stabilized by a graft copolymer of poly(12-hydroxystearic acid) (PHS) onto a PMMA backbone [17]. The reaction mixture initially consisted of the monomers methylmethacrylate (MM; Fluka) and methacrylic acid (MA; Fluka) dissolved in an apolar solvent: 2 : 1 (w/w) hexane (Aldrich) / Exxsol D 100 (Exxon Chemical Europe Inc.) mixture. The monomer concentration in the initial mixture was typically 40 wt %. The particle size was tuned by adjusting the ratio [monomer]/[PHS-stabilizer]; a higher ratio resulted in larger particles. In the final locking step the stabilizer was chemically attached to the particles [17].

The particles were fluorescently labelled by adding a dyed monomer, which copolymerised with MM and MA. This fluorescent monomer was made beforehand by coupling rhodamine-B-isothiocyanate (RITC, Aldrich) to amino-styrene (Aldrich), as described by Bosma *et al.* [18]. In the present work several colloidal systems were used. The system labelled as D34 had a diameter σ of 1.67 μm and relative polydispersity ξ of 5 % (determined by static light scattering); D35: $\sigma = 1.50$ μm and $\xi = 6$ %; DX22: $\sigma = 1.32$ μm and $\xi = 6$ %. The last mentioned system consisted of core-shell cross-linked particles. Details about the synthesis of cross linked particles with a fluorescent core and a non-fluorescent shell can be found in a recent paper by Dullens *et al.* [19].

After the synthesis these systems were dried and redispersed in a 3 : 1 (w/w) mixture of cyclohexyl bromide (Fluka) and *cis*-decalin (Aldrich). In this mixture

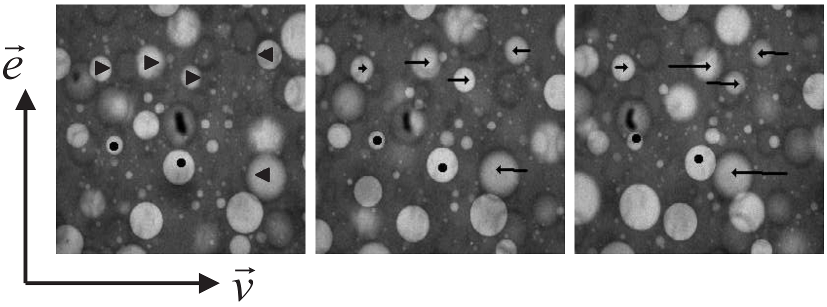

FIGURE 2.3. Confocal images (xy, 75 μm x 75 μm) of a sheared gelatine-dextran emulsion (applied shear rate = 1 s^{-1}). Snapshots were taken at time intervals of 10 seconds. Stationary drops are marked with filled circles; moving drops are marked with arrows pointing in the direction in which the drop moves.

the mass density of the particles and the solvent were nearly matched, so that the sedimentation or creaming of the particles was suppressed as much as possible. In addition, the refractive index of the particles was almost equal to that of the solvent (as well as to the refractive index of the glass plate of the shear cell and the immersion oil). The latter is important for imaging particles (in fluorescence mode) in bulk. In this solvent mixture the PMMA spheres were found to carry a charge [48, 49]. For these measurements the charges were screened by addition of an oil-soluble salt, i.e. tetrabutyl ammoniumchloride (Sigma Aldrich) at a concentration of 260 μM. In this way the particles approximated hard-spheres, crystallizing at a volume fraction of 0.47.

2.3. RESULTS AND DISCUSSION

To illustrate the concept of the counter-rotating cell we first show measurements carried out on a gelatine-dextran emulsion. The droplet size distribution in the prepared macro-emulsion is very broad. A typical droplet size is about 10 μm, which means that its Brownian motion can be neglected. Successive confocal images of a sheared emulsion are shown in Fig. 2.3. These xy-images were taken parallel to the glass plate and thus are perpendicular to the velocity gradient direction (= z-direction).

As a result of the applied shear field some droplets were seen to travel upward while others move downward. Some did not move at all, because their centre of mass was in the plane of zero velocity. For large objects such as these emulsion droplets we developed a computer controlled feedback mechanism that enabled tracking of an individual particle for a prolonged period of time. As soon as the selected droplet leaves the zero-velocity-plane due to collisions with other droplets or due to slight mechanical drift, it starts drifting up or down with respect to the image plane. The computer then adjusts the ratio of the rotational speed of cone and plate ($\omega_{\mathrm{cone}}/\omega_{\mathrm{plate}}$) such that the drift is eliminated. The necessary angular velocities were calculated by determining the displacement of the droplet between two successive frames using image cross-correlation, under the constraint that the shear rate (and thus $\omega_{\mathrm{cone}} - \omega_{\mathrm{plate}}$) remained constant. In this way an emulsion droplet can be tracked indefinitely so that its deformation by the flow and by interactions with other droplets can be observed.

Unlike in a sheared macro-emulsion, in a sheared colloidal suspension all the particles in focus travel at nearly the same velocity. The reason is that the centre of mass of all the imaged particles lies at the same depth to within about 1 μm (the diameter). Another essential difference with the emulsion droplets is that the colloidal particles perform Brownian motion. In colloidal dispersions the particles move in and out of the zero-velocity-plane too rapidly for them to be tracked at the frame rates that we are using (maximum 4 frames s^{-1} for 256 x 256 pixels). Colloidal crystals represent an exception to this, because here the particles are confined to their lattice positions. We will demonstrate this later. In colloidal fluids we can gain most information on the flow profiles by imaging parallel to the velocity gradient (= z-direction) and the flow direction (= x-direction). Scanning frames in such a way results in images in which the particles seem to be deformed into slanted ellipses (see Fig. 2.4). The deformation originates from the fact that scanning an image takes time. The image is scanned line by line from bottom to top: $z(t) = \alpha t$, with α the scan rate: thus the top and bottom will be displaced relative to each other by an amount $x_{\mathrm{top}} - x_{\mathrm{bottom}} = v(z)\Delta t = v(z)(z_{\mathrm{top}} - z_{\mathrm{bottom}})/\alpha$, where $v(z)$ is the velocity of a particle of diameter of which the centre of mass is situated at height z in the shear field. This equation can be rewritten as:

$$\frac{x_{\mathrm{top}} - x_{\mathrm{bottom}}}{\sigma} = \frac{v(z)}{\alpha}. \tag{2.1}$$

The latter expression equals dx/dz and describes the inclination of the imaged particles as a function of the height. This slope can be determined by analysing the confocal images. In order to do so we first aim to find the apparent shape of the imaged particles $x(z)$. We wrote a routine that calculated the cross-correlation function of every two successively scanned lines. In the next step the position of the maxima of these cross-correlation functions were tracked and accumulated, resulting in the final shape $x(z)$.

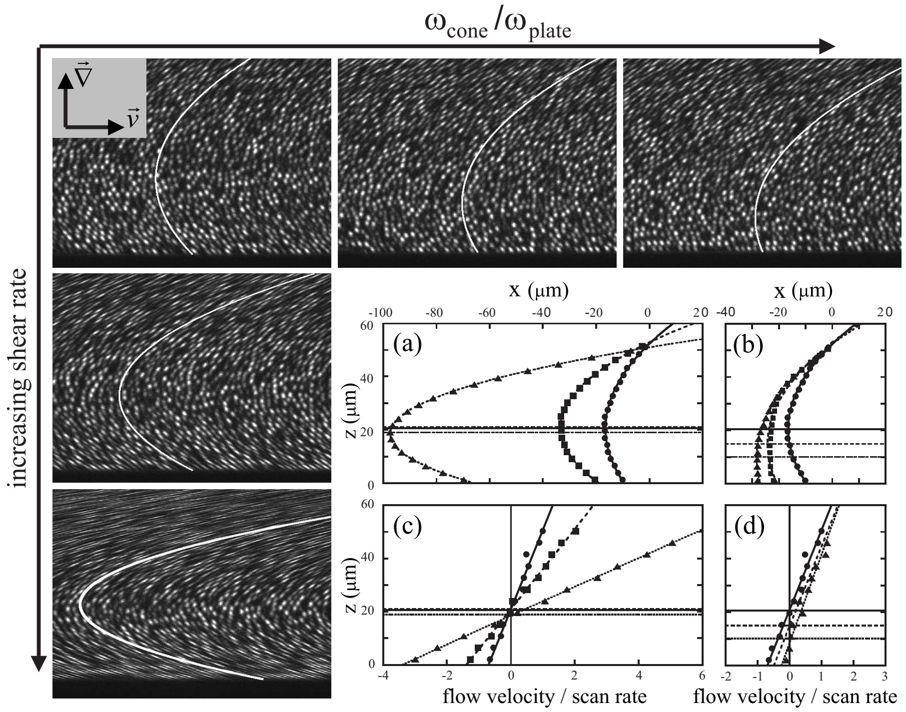

FIGURE 2.4. Confocal images (xz, 75 μm $\times$ 60 μm, 512 $\times$ 512 pixels) of a colloidal fluid at various shear conditions. The applied shear rates are 1.67, 3.36 and 8.39 s^{-1} (top to bottom); the applied ratios ($\omega_{\mathrm{cone}}/\omega_{\mathrm{plate}}$) are 84, 129 and 175 (left to right). Images are overlaid (in white) with the particle shape calculated from initial conditions following Eq. 2.2. Graphs (a) and (b) show the measured shape $x(z)$ from the images, resulting from image and data analysis (using the cross-correlation of lines). The velocity profiles obtained (dx/dz) are shown in graphs (c) and (d).

The results of this analysis are shown in the two upper graphs in Fig. 2.4. Graph (a) shows the curves obtained for experiments at three different shear rates corresponding to the images on the left side. Graph (b) shows the apparent shape for experiments done at different ratios $\omega_{\mathrm{cone}}/\omega_{\mathrm{plate}}$ (and constant $\omega_{\mathrm{cone}} - \omega_{\mathrm{plate}}$) corresponding to the images displayed at the top. The derivatives dx/dz of these curves directly yield the flow profile (Eq. 2.1). These flow profiles are plotted in graph (c) and (d). It can be seen that increasing the shear rate while keeping the ratio $\omega_{\mathrm{cone}}/\omega_{\mathrm{plate}}$ fixed keeps the zero-velocity plane at the same height to within

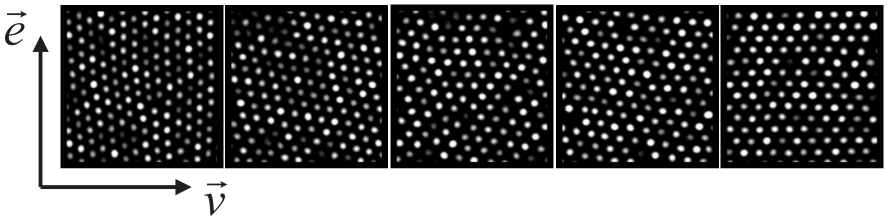

Figure 2.5. Reorientation of the hexagonal layer after applying a shear field. The applied shear rate yields 0.167 s^{-1}. Snapshots are taken at $t = 0$, 65, 130, 195 and 390 s; the shear is initiated at $t = 5$ s. Images are 18.75 μm × 18.75 μm (128 × 128 pixels.) The particles used here are core-shell particles (DX22) with a diameter of 1.32 μm.

2 μm (c). On the other hand, increasing the ratio lowers the stationary layer while the shear rate stays constant (d). When we deal with a simple shear flow the flow profile is given by $v(z) = \dot{\gamma}(z - z_{\text{zvp}})$, where $z_{\text{zvp}} = h/(|\omega_{\text{cone}}/\omega_{\text{plate}}| + 1)$. In our case, the gap h is 1.70 mm. The expression for the deformation now becomes parabolic:

$$x(z) = \frac{\dot{\gamma}}{\alpha} z \left(\frac{1}{2} z - z_{\text{zvp}} \right). \qquad (2.2)$$

Hence, for a linear velocity profile over the whole gap, the apparent shape of the imaged particles is completely determined by the applied shear rate and the applied ratio $\omega_{\text{cone}}/\omega_{\text{plate}}$. In Fig. 2.4 these calculated curves are plotted over the confocal images. The calculated shape agrees very well with the images, which means that the measured velocity profiles are indeed linear. For the data in Fig. 2.4 the scan rate α is 34 μm s^{-1}. Therefore it takes about 40 ms to scan a particle from top to bottom. The Brownian motion during this time period is small enough not to disturb the analysis: the root mean square displacement is about 100 nm ($= \sigma/15$), assuming infinite dilution, and will even be significantly less because of particle interactions and hydrodynamics.

In addition to fluids, it is also interesting to study colloidal crystals in shear flow. The first observation when applying a shear field to a crystal consisting of hexagonal stacked layers is that the layers reorient themselves in the steady shear field. Regardless of the original crystal orientation, the applied shear orients the hexagonal planes in such a way that close-packed lines point into the flow direction. The process of re-orientation is demonstrated in Fig. 2.5.

In a colloidal crystal most of the particles are confined to lattice positions, so they can be tracked in the plane of zero-velocity for a long period of time. To stay away from the shear melting transition the applied shear rates here had to be an order of magnitude lower than the shear rates that we applied to the colloidal fluid.

The advantage of these low shear rates is that the particles can be not only imaged in the plane of zero velocity, but also in wider z-range around this plane. In fact, time series of xy-confocal images were captured in about 10 layers around the zero velocity plane. For each layer we used cross correlation of successive images to calculate the motion due to flow (see Experimental Section). A typical example is shown in Fig. 2.6a. The slopes of the lines correspond to the velocities of these layers. For experiments done at four different shear rates these velocities are plotted in Fig. 2.6b as a function of height (expressed in terms of number of layers from the glass plate). The slopes of the lines in this graph give the actual shear rates in the four experiments. From Fig. 2.6a it can be seen that every layer moves with a velocity that is intermediate between the velocities of its two neighbouring layers. In other words: all layers slide over each other; no two layers ever move in unison. We found this in all experiments and therefore we conclude that in the lower 100 μm, where we could image, the flow profile in colloidal crystals is linear down to the particle level.

On comparing the measured shear rates with the applied ones we found, as expected from Fig. 2.4, good agreement for the colloidal fluid samples (Fig. 2.7a). However, in case of the sheared crystal, we observed a remarkable difference. The measured shear rates are much higher than those applied (Fig. 2.7b). The discrepancy cannot be explained by wall slip because this would lead to measured shear rates that are too low. We conclude that, although we have no direct evidence yet, the velocity profile cannot be linear throughout the whole gap. We believe that this is an indication for shear banding.

The measurements shown here were performed with an objective with a free working distance of 100 μm. This did not allow us to image particles throughout the whole gap, which is 1.7 mm. Future work will involve the use of longer working distance objectives so that information can be gained over a larger distance in the gap.

In the following we discuss results concerning particle dynamics in the plane of zero velocity of a sheared crystal. The combination of a counter rotating shear cell and confocal microscope gives the opportunity to image one stationary layer exclusively in a 3D bulk system under shear. In this way we are able to analyse the dynamics of the colloidal particles in real space in great detail.

At moderate shear rates (up to several s^{-1}) the particles in an ordered layer in the zero velocity plane can stay in focus for a sufficiently long time to measure

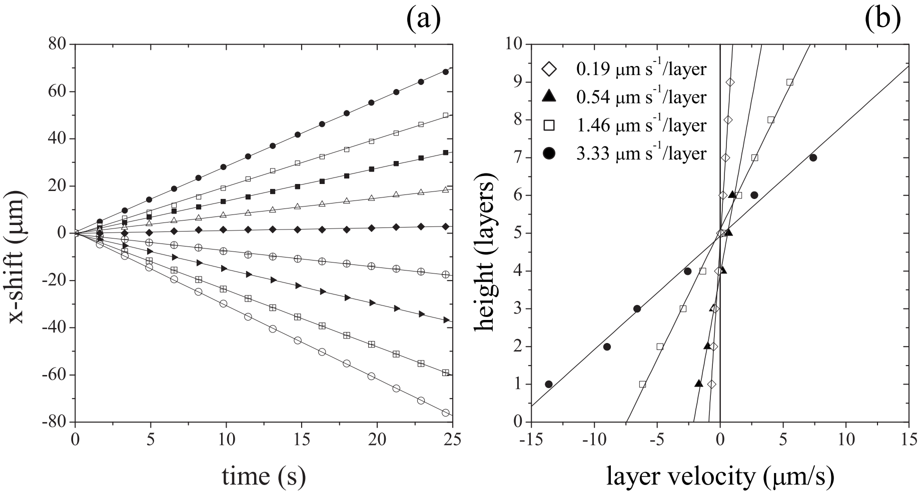

Figure 2.6. The velocity profile in the sheared crystal is measured layer by layer. (a) Image analysis of time-series of xy-images results in the y-position shift as a function of time. (○) corresponds to the layer closest to the glass plate; (●) corresponds to the 9th layer (counted from the glass wall). (b) Slopes from (a) give the layer velocity as a function of height. Data from (a) correspond to (□) in (b). The measured shear rates obtained are expressed in μm s^{-1}/layer. Assuming a layer spacing d of $\sqrt{2/3}$ times the measured interparticle spacing λ in the xy-plane ($\lambda = 1.80$ μm; $d = 1.47$ μm), these numbers correspond to actual shear rates of 0.13 s^{-1}, 0.37 s^{-1}, 1.0 s^{-1} and 2.3 s^{-1}. For these experiments we used particles with a diameter of 1.67 μm (D34).

individual particle trajectories. The higher the shear rate the more difficult it is to keep the particles in focus, for several reasons. Firstly, the glass plate is moving at higher speed and as a result more variations in height are encountered during the time of the experiment. Secondly, the height of the crystalline plane is fluctuating more. Thirdly, rearrangements in the layer, a precursor to shear melting, become more frequent.

To study the particle dynamics in the zero velocity plane time series (typically 256 frames) were captured over a region of 18.75 μm × 18.75 μm (256 × 256 pixels) with a high scan rate (3.9 frames s^{-1}). Fig. 2.8a shows a representative image from such a series. Image analysis gave the coordinates of the particles in the successive frames. Subsequently, these coordinates were ascribed to the individual particles, producing all the trajectories. Directly plotting these tracks gives a tangle of curves from which not much can be learned. After subtracting

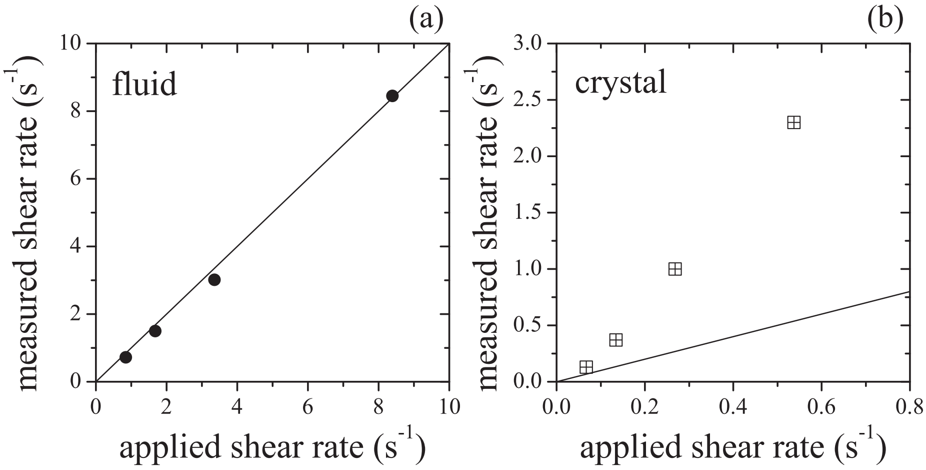

FIGURE 2.7. Measured shear rate vs. applied shear rate for the sheared fluid (a) and crystal (b). Solid lines represent: measured shear rate = applied shear rate. Plotting the measured shear rate as function of the applied shear rate demonstrates an interesting discrepancy from the applied shear rate in case of the crystal, while the fluid shows normal behavior. For the crystal the shear rate in this region is much higher than expected.

the collective motion obtained by averaging over all the particles we end up with spatially separate tracks, from which we observe particles moving around their average lattice position (Fig. 2.8b).

The average collective motion of the frames is obtained by calculating the shift in the position of the center of mass between two successive frames, weighting all the particles that appear in both frames. This collective motion does give us information on how the layer as a whole moves in the applied shear flow. As we learned from the measurements of flow profiles in a crystal, all the layers do slide over each other. So, if we want to learn how the particles behave when the layers slide over each other, we should also study the collective motion in more detail (see Chapter 3).

Of course it would be most informative if the positions of particles in several layers could be measured simultaneously, and correlated. This was approximated by taking time series as before, but alternately scanning one layer (z_{layer1}) and the layer above (z_{layer2}). Note that there are some differences with the 2D time-series described above. One difference is that strictly speaking only one layer can be in the zero-velocity-plane, while in the other layer the particles will move a bit more.

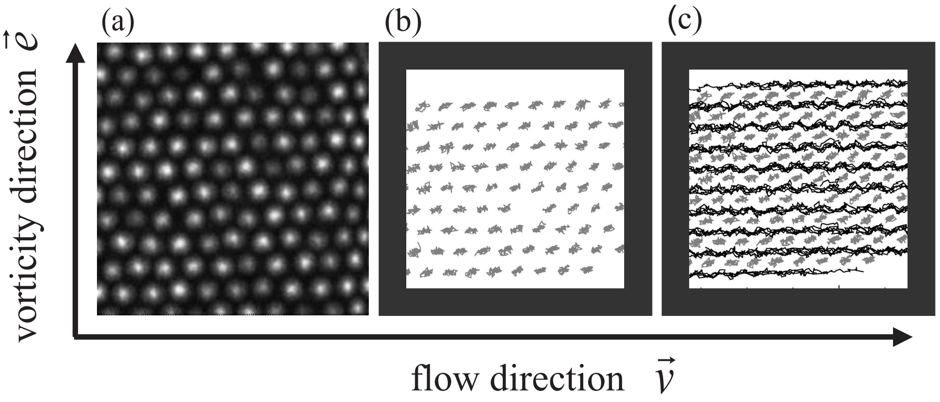

Figure 2.8. Image analysis and particle tracking in the zero-velocity-plane reveals the dynamics of the sheared crystal. Moreover dynamical information from two layers at the same time is gained. The zigzag motion of the particles from one layer over the adjacent layer is clear for the image at the right. Image size is 18.75 μm x 18.75 μm (256 x 256 pixels). The colloids used have diameter of 1.50 μm (D35).

Another difference is that the time interval between two images of the same layer is longer than for a 2D time series. Both effects reduce the maximal shear rate that still can be applied in order to obtain analysable data.

In Fig. 2.8c we plot the tracks of both layers. Here the small residual drift of the stationary layer was subtracted from the particles in both layers, producing their relative motions only. In this way we see the particles in the adjacent layer slide over (and move through the holes in between) the particles in the stationary layer. From this plot it can qualitatively be seen that the particles perform a zigzag motion when the layers are sliding over each other, as was already inferred by Ackerson *et al.* from light scattering data [11].

2.4. Conclusions

A counter rotating shear cell combined with confocal microscopy opens many possibilities for studying colloidal systems, as well as larger non-Brownian objects, in a shear flow in real space quantitatively on a single particle basis. Flow profiles can be measured on a microscopic level in colloidal fluids and crystals. Indications for shear banding in sheared hard-sphere like crystals were found. Particles in the zero velocity plane of a sheared colloidal crystal can be tracked. Finally, we have shown the possibility of capturing and tracking two layers (almost) simultaneously:

as an example we demonstrated the zigzag motion with which close packed planes of hard-spheres slide over each other.

Acknowledgements

The continuous shear cell was designed in close collaboration with the Wageningen Centre for Food Science (WCFS), Forschungszentrum Jülich (FZ-J), the University of Twente and Unilever Research, from which we would especially like to thank Yves Nicolas, Marcel Paques (WCFS) and Jan Dhont (FZ-J). We thank Paddy Royall for critically reading the manuscript.

3

Dynamics in Sheared Colloidal Crystals

Abstract

We investigate particle dynamics in nearly hard sphere colloidal crystals when these are submitted to a steady shear flow. The displacements of both the single colloids and of the crystalline layers as a whole are studied by using a home built counter rotating shear cell in combination with confocal microscopy. Our real space observations confirm the global structure and orientation as well as the collective zigzag motion as found by early scattering experiments. Moreover, we find that random particle displacements increase with shear rate. Shear induced melting takes place when their mean square displacement has reached about 13 % of the particle separation. Furthermore, we show that local rearrangements become more and more pronounced with increasing shear rate. From images of the flow-gradient plane parts of the system are seen to alternate between a more and less ordered state, eventually leading to shear melting.

3.1. INTRODUCTION

When does a crystal melt into a fluid? And how does shear flow affect this condition? In 1910 Lindemann addressed the first question: He proposed that as soon as the molecular fluctuations exceed ∼10 percent of the intermolecular spacing the order will be destroyed [50]. This Lindemann criterion was shown to hold also in colloidal crystals as has been demonstrated using computer simulation [51, 52] and experiments [52–54]. In soft matter systems we have the possibility to easily modify the melting transition by applying external fields. In this Chapter, we show that these fluctuations leading to melting do not necessarily have to arise from an increase of thermal agitation on approaching the melting line, but are also increased by subjecting the crystal to shear flow. This eventually leads to complete shear induced melting of the 3D-crystal. The Lindemann melting criterium was already used in the context of shear flow by Lindsay and Chaikin [55] who observed the shear melting transition through a sudden viscosity increase, and Ackerson and Clark who observed a reduction of long ranged order with light scattering [32]. However, the increased fluctuations were be hypothesized rather than observed. More recently, Lindemann-like arguments were used to describe the phase behaviour of 2D-systems of magnetic particles [56]. In the latter experiments the interparticle interaction can directly be tuned by the applied magnetic field strength, whereas the effect of shear flow is indirect and occurs via the interplay with the suspending fluid.

Shear-induced transitions are by no means unique to colloidal dispersions, but have been discovered in many other forms of soft condensed matter [24]. For example the microstructure of wormlike micellar systems appears to be highly sensitive to shear flow. In these surfactant systems a shear-induced isotropic-to-nematic transition [57] was observed as well as a shear banding transition where bands of high and low viscosity phases coexist under shear [58]. Interestingly, indications for shear banding were also found in colloidal systems [33,59,60]. Here, the system splits into bands of crystalline and shear-melted structure, with the latter growing at the expense of the former as the shear rate is increased. Other transitions observed in colloidal systems include shear-induced ordering [11,61,62], changes of crystal symmetry [63], and shear thickening [64]. The processes leading to the formation of shear-induced structures are still a subject of intense research. For this colloidal suspensions have the advantage, above most other soft matter systems, that individual particles can be visualized in situ while undergoing shear with (confocal) microscopy. This opens up the possibility to study the essential microstructural response of the dispersion during shear flow directly.

In the 1980s the effect of shear flow on colloidal crystals was investigated extensively by means of light scattering techniques. In this way the global structure and orientation of the sheared systems was obtained [11, 32]. In the last decade the use of microscopy techniques became more established [33], though real space investigations to study the effect of shear flow on the particle level in dense colloidal suspensions suspensions are not very numerous yet. Cohen *et al.* showed that strongly confined systems in shear flow gave rise to unexpected new crystal structures [65]. Also there was reported on the effect of a very low strain on the dislocation dynamics in colloidal crystals [66]. The difficulty with the study of a 3D system in a steady shear flow is that particles simply flow out of the field of view of the microscope, drastically limiting the time a particle can be followed (or be recognized to be the same particle). This problem we circumvent here by using a counter rotating shear cell in which the stationary layer can be positioned away from the glass wall (see Chapter 2).

Shear melting has been found to occur in two stages: first there is the transition from a crystal in which the particle positions are bound to the 3D lattice sites to a situation in which (hexagonally ordered) layers slide more or less freely over each other [11], [Chapter 2]. The in-plane order is preserved till considerably higher shear rates, but will eventually vanish at higher shear rates as well. In this paper we will first investigate this sliding layer motion and look at the collective displacement of particles in a layer. Second, we focus on how shear affects the random particle displacements and on the rearrangements of the individual particles within such a layer. Finally, we relate this increase in fluctuations to the loss of crystalline order upon approaching the shear melting transition.

3.2. EXPERIMENTAL METHODS

We used rhodamine labeled poly(methylmethacrylate) (PMMA)-spheres with a diameter of 1.67 μm made by dispersion polymerization and sterically stabilized by a layer of poly(12-hydroxystearic acid) (PHS) [17, 18]. The particles were dispersed in a 3 : 1 w/w mixture of cyclohexylbromide and *cis*-decalin, saturated with tetrabutylammoniumbromide (TBAB) yielding a nearly density and refractive index matched system in which the colloids behave nearly hard-sphere like ($\phi_{\text{crystal}} = 0.47$) [48]. The volume fraction of colloids was chosen to be well within the crystalline region of the phase diagram at a volume fraction 0.57.

In order to create a well-defined shear flow a home-built counter rotating cone plate shear cell was used. This setup was mounted on top of an inverted confocal microscope (Leica TCS SP2), and consists of a (replaceable) metal cone that makes an angle of either 1 or 4 degrees with a glass plate that has a diameter of 6.5 cm.

The counter rotating principe allows us to locate the stationary layer (zero velocity plane) in the bulk of the system. More details of the set up can be found in Chapter 2. The z-position of the 100× 1.4 NA oil immersion objective was controlled by a piezo-focusing drive (Physik Instrumente P-721) allowing imaging of the sample up to 100 μm from the glass wall.

The sample was filled into the cell and a pre-shear of 0.5 s^{-1} was applied for 30 minutes. After stopping the pre-shear, the crystal was left to equilibrate for an additional hour, before starting the shear experiments described here. Time series were taken in the flow-vorticity (xy-) plane as well as the flow-gradient (xz-) plane. The minimum capturing time of one frame is 0.26 s. Particle coordinates were determined using routines similar to those of Crocker and Grier [46]. Local shear rates were determined from flow profiles by measuring the velocity of a number of layers around the zero velocity plane as explained in Chapter 2.

3.3. RESULTS AND DISCUSSION

3.3.1. Collective motion of layers

When the cell was filled with the dense suspension a polycrystalline arrangement of random stacked hexagonally close packed (rhcp) crystals was formed with the hexagonal layers parallel to the (horizontal) glass wall. The pre-shear treatment further aligned the crystal such that in each xy-plane the closest packed line points (with a deviation of ±3°) into the direction of flow. This was shown in Chapter 2 (Fig. 2.5). A typical resulting structure can be seen in the two confocal images in Fig. 3.1 for two different shear rates. These are snapshots from movies taken at approximately the eighth layer counted from the glass plate. In our experiment we applied a constant shear rate $\dot{\gamma}$ which implies that we force the layers to slide over each other. (This is in contrast to constant stress experiments in which at sufficiently low stress the 3D-crystal structure can be maintained, because it has a yield stress.) Time series of the hexagonal plane show that particles in the layers oscillate collectively in the vorticity direction. This is visualized in the graphs in the right part of Fig. 3.1. On the vertical axis we plotted in greyscale a histogram of the y-positions of all particles in a horizontal cross section through the image. This done for each frame in the time series. The peaks in the histogram are given a dark color and correspond to a high probability of finding a particle at that vertical position. It is seen that these peak positions oscillate in time, which implies that rows of particles oscillate in phase. The frequency of the oscillations increases with increasing shear rate. To clarify the origin of this collective movement additional

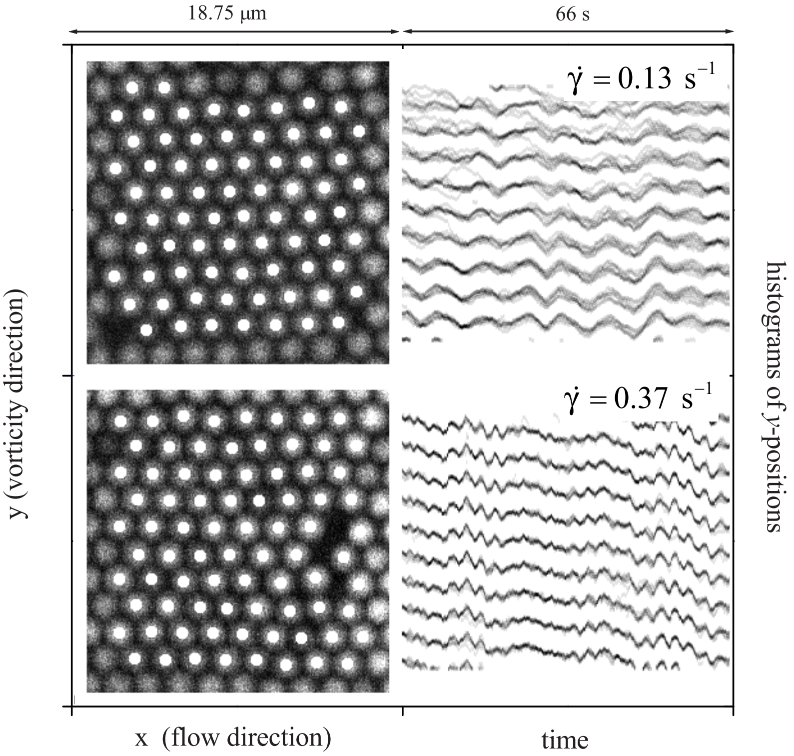

Figure 3.1. Visualization of the collective motion of the layer. Images on the left show a snapshot at time $t = 0$ with the corresponding coordinates on top. On the right the projection of the particle position along the x-axis is shown as function of time. Top panels correspond to a shear rate of 0.13 s^{-1}, bottom panels correspond to 0.37 s^{-1}.

data were taken by capturing time series of an xyz-stack consisting of three xy-frames through the centers of particles in three adjacent layers. In Fig. 3.2 the particle coordinates of these three layers are plotted in one figure. From these figures it can be seen that the observed zigzag motion clearly is an effect that arises via interaction with particles in the neighboring layers. At this high volume fraction there is simply no space for layers to slide over each other in a straight line. As a result a particle follows a zigzag path through the saddles in the landscape formed by the adjacent layers. In each period of the oscillation the particles move over the distance of one interparticle spacing with respect to the adjacent layer. The oscillation frequency should then be proportional to the shear rate. This is confirmed in Fig. 3.3. The trajectory of the center of mass $\vec{r}_{\mathrm{CM}}$ is determined by

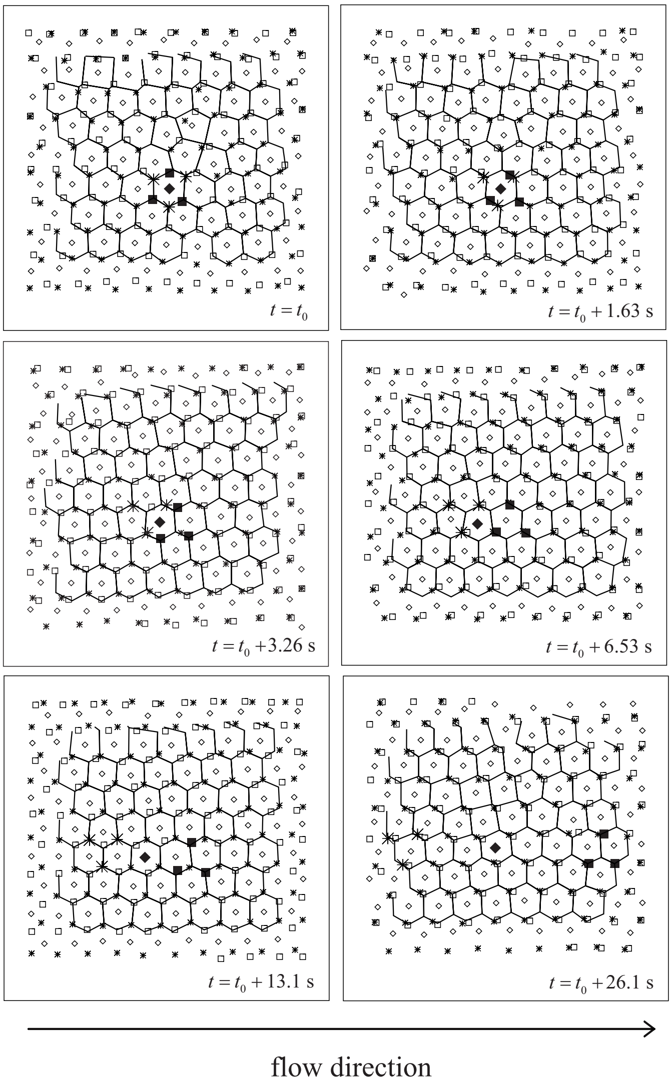

Figure 3.2. Particle positions in three adjacent layers in shear flow ($\dot{\gamma} = 0.08$ s^{-1}) at six different times. A Voronoi construction of the middle layer (diamonds) is shown. Particles in the lower layer (stars) and upper layer (squares) are seen to neatly follow the path formed by the edges of the Voronoi cells. One particle in the middle layer (filled diamond) and its neighbors (larger stars and filled squares) at $t = t_0$ in the adjacent layers are highlighted, so that they can be followed in time.

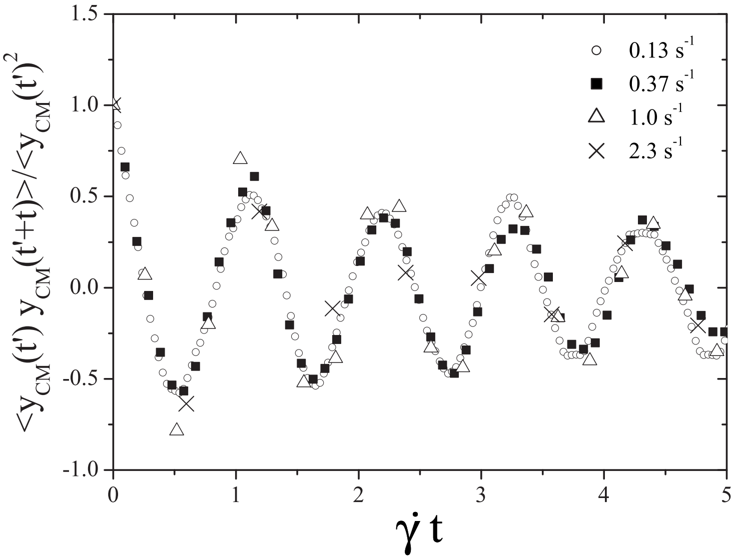

Figure 3.3. Collective zigzag motion in sheared colloidal crystals. Autocorrelation function of the y-coordinate of the center of mass, showing the oscillations of particles in the vorticity direction. Time is normalized with the experimentally independently obtained (local) shear rate.

comparing the average position of those particles in an image appearing in both of two subsequent frames:

$$\vec{r}_{\mathrm{CM}}(t) = \sum_{t'=\Delta t}^{t} \frac{1}{N_{t'}} \sum_{i=1}^{N_{t'}} \left(\vec{r}_i(t') - \vec{r}_i(t'-\Delta t)\right). \tag{3.1}$$

Here, i runs over all particles showing up in two subsequent frames, and Δt is the time interval between those two frames. From this we then calculate the autocorrelation function of its component in the vorticity direction (y_{CM}):

$$g_y(t) = \frac{1}{T} \int_0^T y_{\mathrm{CM}}(t')\ y_{\mathrm{CM}}(t'+t)\ dt', \tag{3.2}$$

where T is the duration of the time series. Plotting this function against time normalized with the shear rate results in a nice overlap of the experiments at different shear rates. The shear rates used in this figure were measured independently by determining the velocity in xy-time series of ∼10 layers around the studied layer, as was discussed in detail in Chapter 2 (Fig. 2.6). In these experiments we directly measured the velocity difference (in μm s^{-1}) between the layers. To find the shear

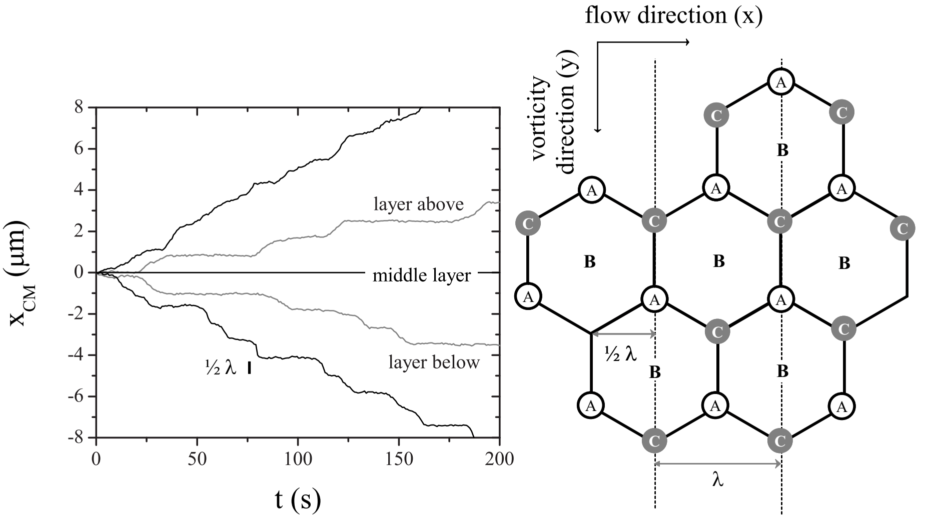

FIGURE 3.4. Hopping at low shear rates. The grey line corresponds to a shear rate of 0.01 s^{-1}, and the black line to a shear rate of 0.03 s^{-1}. We plot the x-position of center of mass relative to the middle layer, showing the displacement in the flow direction. Particles in adjacent layers reside at an 'A' or 'C' position (see sketch) for prolonged periods of time, and spend less time at intermediate positions. Each step the layer moves over a distance of half the interparticle spacing λ (0.9 μm).

rate (in s^{-1}) we assume that the layers are separated by a distance of $\sqrt{6}/3$ times the in-plane interparticle spacing λ. Therefore one period τ is expected to take $\lambda/\Delta v = \lambda/(\dot{\gamma}\Delta z) = 3/\dot{\gamma}\sqrt{6} \approx 1.22/\dot{\gamma}$. However, the period of an oscillation is seen to be only $\tau = 1.14/\dot{\gamma}$. This is close to the expected value, but the difference is statistically significant. A possible explanation is that, to facilitate the sliding of layers, the spacing in between the layers is slightly increased, while in-plane the particles are slightly compressed. To reconcile the expected and measured values halfway (i.e. at $\dot{\gamma}\tau = 1.18$) an expansion of the layer spacing of 3.4 % must be assumed. Such a small expansion is very hard to detect in observations of only up to three layers. Later on we will see, by studying a larger number of layers (Fig. 3.11), that in shear flow the layer spacing is indeed about 3 % increased. The zigzag motion is still observed at a shear rate of 2.3 s^{-1}. At a shear rate of 3 s^{-1} all order was lost and the system was said to have shear melted.

The importance of shear flow, which tends to distort the structure, in comparison to the thermal motion, which tends to restore the equilibrium structure, is usually expressed as the Péclet number $\mathrm{Pe} = \eta\dot{\gamma}\sigma^3/k_BT$ [67]. Here η is the viscosity of the solvent and σ the particle diameter. For these experiments $\mathrm{Pe} \approx 2.3\ \dot{\gamma}$. At very low Pe number ($\ll 0.2$) the zigzag motion becomes very difficult to detect. Particles spend most of the time at a lattice site formed by the adjacent layers. They avoid the interstitial positions as much as possible, and hop to the next site only rarely. Still, when averaging over long enough times the hexagonal layers are seen to move relative to each other, and the velocity profile is on average linear. In Fig. 3.4 we have visualized this 'stick-slip' motion by plotting the x-position of the center of mass relative to the middle layer as a function of time for three adjacent layers. It is seen that a particle moves over half an interparticle spacing at each jump. This corresponds to a move from an 'A' to a 'C' position. The jumps of the first and third layers are not necessarily in step. At higher shear rates the steps progressively smoothen out (compare also Fig. 2.6).

3.3.2. Fluctuations of individual particles

The collective motion of the particles in a layer is to a large extent dictated by the three dimensional character of our suspension. To study the fluctuations of individual particles we have to properly subtract this collective motion. The most straightforward method seems to be by subtracting the center of mass of the layer. Closer inspection of the data shows a disadvantage of this approach: it regularly occurs that a part of the crystalline layer slips with respect to another part (see Fig. 3.5). Then all particles seem to be displaced with regard to the center of mass, while actually only the particles at the boundary move in a different way than their neighbors. This is undesirable especially since we observe that this type of *cooperative* rearrangements [68] become more abundant with increasing shear rate. Obviously, the distinction between the random and collective motion of the particles in a flow field is not that sharp. Interestingly, similar difficulties were encountered in studies of melting of two dimensional systems both in experiments [56] and simulations [69]. Moreover, a truly 2D-crystal does not have long range positional order, and the mean square displacement diverges. We choose for a similar solution: Instead of considering the absolute particle displacements, we calculate the relative displacement of pairs of neighboring particles. The vector between the positions of two neighboring particles is given by $\vec{r}_{ij} = \vec{r}_i - \vec{r}_j$, where $i > j$ are the indices of the neighboring particles. Each unique pair is given an identification number, so that the pair can be tracked in time. In this way a pair is followed for as long as the particles remain nearest neighbors (as calculated by a Delaunay triangulation). The displacements in time t are then calculated for each pair according to $\Delta\vec{r}_{ij}(t) = \vec{r}_{ij}(t' + t) - \vec{r}_{ij}(t')$. Histograms of these

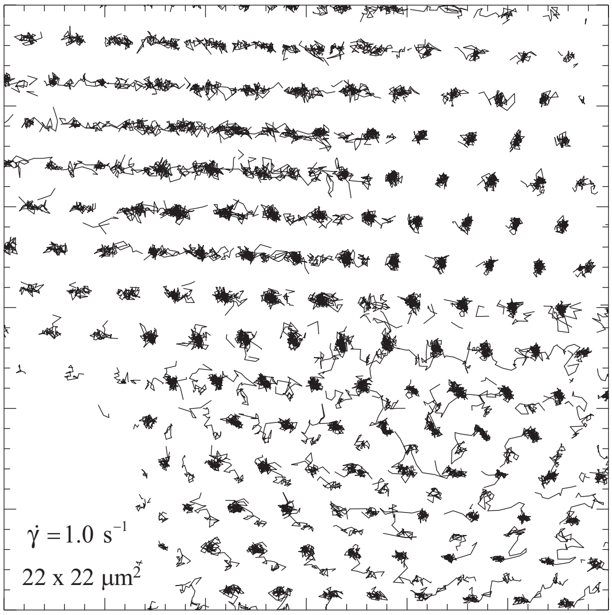

FIGURE 3.5. Particle tracks in the xy-plane of the crystal at shear rate 1.0 s^{-1} after subtracting the center of mass. In this case different parts of the layer slipped relative to each other. All tracks (extending over two or more frames) over a period of 66 s are shown. The time interval between two frames was 0.26 s.

relative displacements in both flow (x-) and vorticity (y-) direction are shown in Fig. 3.6 after different time intervals. The non-sheared system shows a narrow Gaussian distribution, which only slightly widens with time. In shear flow the distribution becomes broader. Also the shape of the distribution is changed: larger displacements occur more frequently than in a pure Gaussian distribution. This is in agreement with the observation that the increased fluctuations are concentrated on a selection of the particles (those at the “boundaries”), while the others -which remain part of a crystalline patch- are much less affected (Fig. 3.5). In Fig. 3.7 the mean square relative displacement

$$\left\langle \Delta r^2 \right\rangle (t) = \left\langle \left(\vec{r}_{ij}\left(t + t'\right) - \vec{r}_{ij}\left(t'\right) \right)^2 \right\rangle \tag{3.3}$$

is plotted as a function of time. Only the displacements in the flow-vorticity plane are taken into account; the displacement in the z-direction can not be extracted from these xy-data. We normalized $\langle \Delta r^2 \rangle$ by $2\sigma^2$. The factor 2 arises because

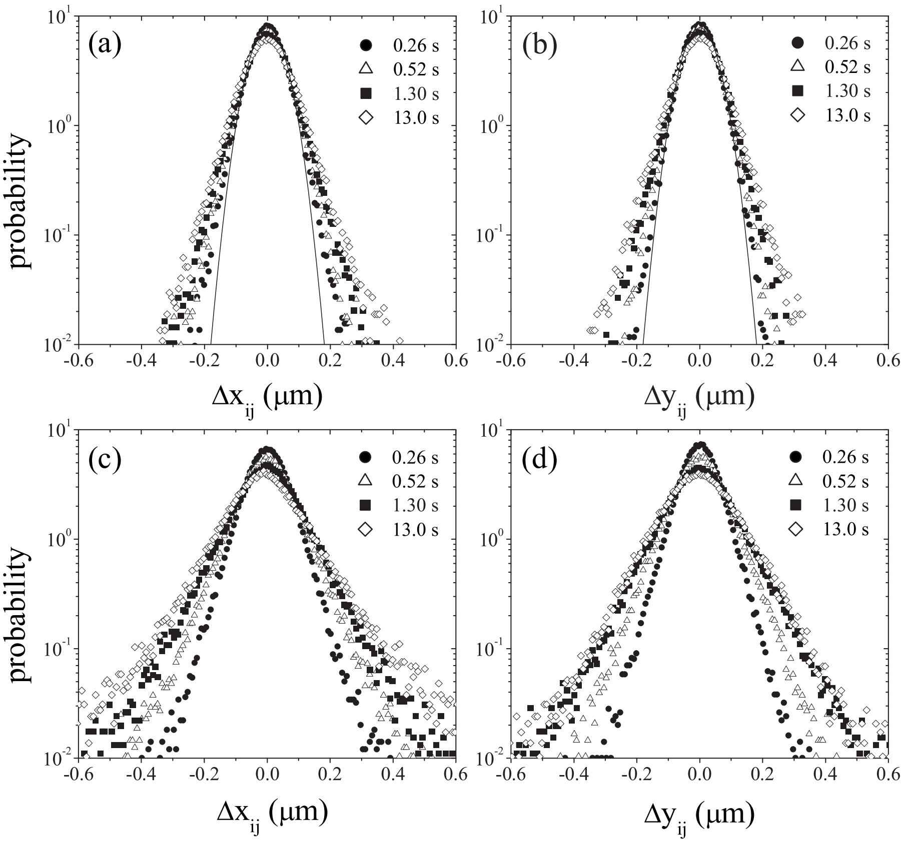

FIGURE 3.6. Histograms of the relative x-displacements after different time intervals for an experiment at zero shear (a) and an experiment at shear rate 0.37 s^{-1} (b). Lines are Gaussian fits to the fluctuation distribution at the smallest time interval.

we are interested in the mean square displacement per particle.[1] It is seen that at zero shear the particles are strongly confined to their lattice site, so that their mean square displacement levels off to a finite value. Within the first few seconds diffusion of the particles in a neighbor cage is observed, while at longer time the cage formed by the neighbors confines the particles. In the absence of shear

---

[1] We have $\langle \Delta r^2 \rangle(t) = \langle (\Delta r_i - \Delta r_j)^2 \rangle = \langle \Delta r_i^2 \rangle + \langle \Delta r_j^2 \rangle - 2\langle \Delta r_i \Delta r_j \rangle$. Displacements average to zero so that $\langle \Delta r_i \Delta r_j \rangle = 0$ and particles are identical so that $\langle \Delta r_i^2 \rangle = \langle \Delta r_j^2 \rangle$. Therefore we must have $\langle \Delta r^2 \rangle = 2\langle \Delta r_i^2 \rangle$.

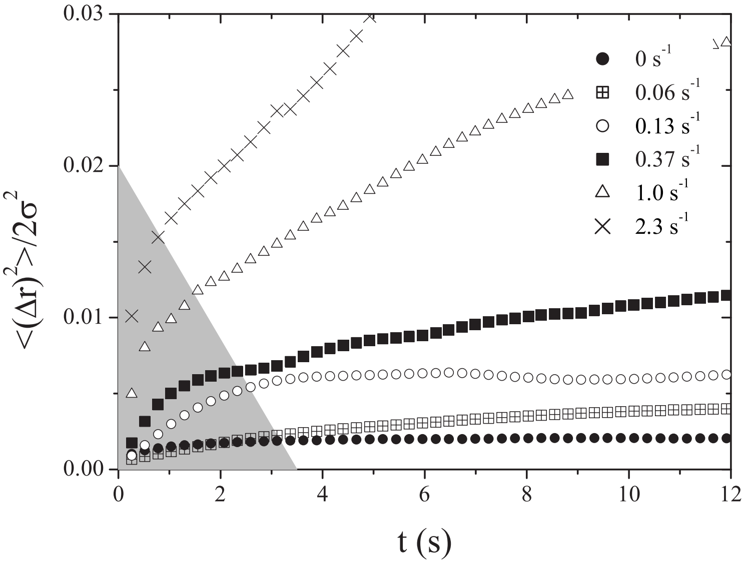

Figure 3.7. Mean square relative displacements in the flow-vorticity plane at different shear rates.

the cage is static and particles cannot escape, at least on the time scale of our experiment. The sheared particles also feel their neighbors after the first (few) second(s), but apparently experience a more dynamic cage from which they still have a chance to escape. Interestingly, at long times the mean square displacement again increases approximately linearly with time.

At long times we see weak oscillations appear. These can be attributed to the different environments a particle experiences while performing their zigzag motion: at the 'A' or 'C' positions a particle has more space to explore, compared to an intermediate position, where its neighbors are even more near.

The shaded part of Fig. 3.7 marks the region where particles still diffuse around their lattice site, before breaking out of their cages. At a shear rate of 2.3 s^{-1} this takes less than a second. On further increasing the shear all crystalline order was lost at $\dot{\gamma} = 3\ \mathrm{s}^{-1}$. The shaded region intercepts the y-axis at a (relative) mean square displacement of 0.02. It is therefore clear from Fig. 3.7 that at the point of shear melting the mean square displacement of particles in their nearest-neighbor cages is approximately $\sqrt{\langle \Delta r^2 \rangle_{\mathrm{melt}}/2\sigma^2} \approx 0.13 \pm 0.01$. In other words, shear increases the random displacements of particles around their lattice positions

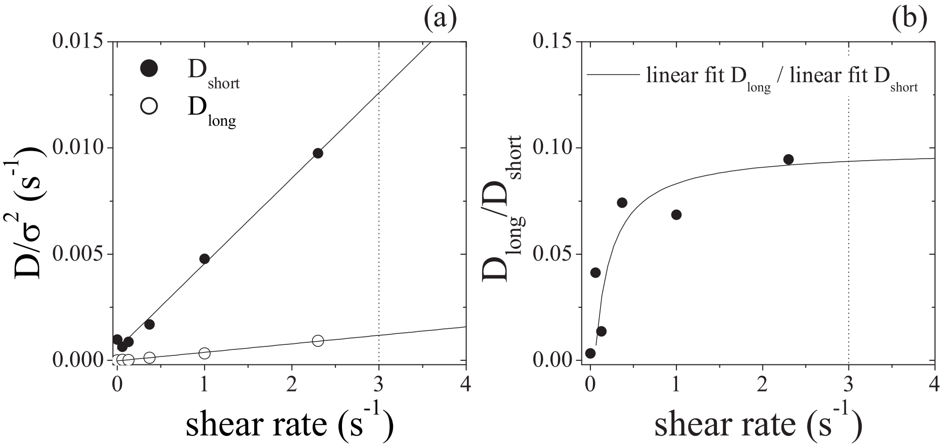

Figure 3.8. Short and long time diffusion coefficients in shear flow as obtained from Fig. 3.7. Total shear melting occurs around a shear rate of 3 s^{-1}. This is indicated by the dotted line. The lines in (a) are linear fits to D_{short} and D_{long}, respectively. The curve in (b) is the ratio of those fits.

until they exceed a value of about 0.13 times the lattice spacing, at which point the crystal shear melts. This is strongly reminiscent of a Lindemann criterion which in this case applies to a nonequilibrium system.[2] It would be very interesting to investigate whether such a criterion also holds in other nonequilibrium systems such as in an electric field.

Based on the arguments above, we can assign two self diffusion coefficients to the sheared systems: One that applies at short time scales, and another which applies at longer times. The best estimate we have for the short time self diffusion coefficient, is the value obtained from the displacements in the shortest experimentally measured time interval: $\langle \Delta r^2 \rangle / 2 = 4 D_{\mathrm{short}} \Delta t$, with $\Delta t = 0.26$ s. At this time scale the colloids display essentially Brownian motion due to the many impacts of solvent molecules. In addition, at these high concentrations, particles influence each other by disturbing the flow field through which they move. Both

---

[2] In the Lindemann criterion also the displacements in z should be included. This increases $\langle \Delta r^2 \rangle_{\mathrm{melt}}$ by an estimated factor 3/2. Furthermore, in the original Lindemann parameter the displacement relative to the ideal lattice position is taken. This is exactly 1/2 as large as the measured mean square displacement (taken relative to the particle's initial position). Thus, our Lindemann parameter should be modified by a factor $\sqrt{3/4}$, which nearly equals unity.

the Brownian character of motion and the effect of hydrodynamic interactions are reflected in the short time self diffusion coefficient. The data obtained are shown in Fig. 3.8a. It is interesting to note that this *short time* diffusion coefficient already increases with the shear rate, and that it does so approximately linearly. Such behavior is exactly that seen in shear induced self diffusion of non-Brownian spheres, which is a purely hydrodynamic effect resulting from the hydrodynamic interactions between the ever-changing configurations of particles under shear [43, 70, 71].

At long time scales particles are further slowed down by direct particle-particle interactions. The long time self diffusion coefficient D_{long} is thus obtained from the linear slope of the long time mean square displacements. In Fig. 3.8a we plot these diffusion coefficients as a function of shear rate. Also D_{long} increases linearly with shear rate. In part this will again be due to hydrodynamic effects. However, here direct interactions between particles, which grow more frequent with increasing shear rate, will contribute to to the increase in D_{long} as well. In Fig. 3.8b, it is seen that, relatively, D_{long} increases faster than D_{short}. Near (or at) shear melting the long time diffusion coefficient is only a factor 10 times smaller than the short time diffusion coefficient.

Interestingly, this ratio $D_{\mathrm{long}}/D_{\mathrm{short}} = 0.1$ was put forward by Löwen *et al.* [52] as a *dynamic* criterion for melting (again in equilibrium systems). This statement was based on the results of Brownian dynamics simulations, and was confirmed by experiments on low density colloidal systems consisting of highly charged soft particles [52, 72] and for slightly soft systems in [73]. Though in these cases the hydrodynamic interactions are less important, the dynamic melting criterion was claimed to apply for concentrated systems where particles do interact through such interactions as well. By taking into account the short time diffusion coefficient which includes hydrodynamic interactions instead of the bare Stokes-Einstein diffusion coefficient, the experimental results for hard sphere crystallization described in Ref. [74] could be explained.

Although obtaining an appropriate value for the short time self-diffusion coefficient remains a challenge, our shear experiments indicate that this dynamic criterion for melting may well be applicable to non-equilibrium systems as well.

3.3.3. Order-disorder on approaching shear melting

Apart from the increased random fluctuations, the shear melting transition is evidently associated with a loss of order. It is seen from time series in the flow-vorticity plane that, locally, the order is sometimes lost to be recovered again later on. This can be quantified by calculating the in-plane (six fold) bond orientational

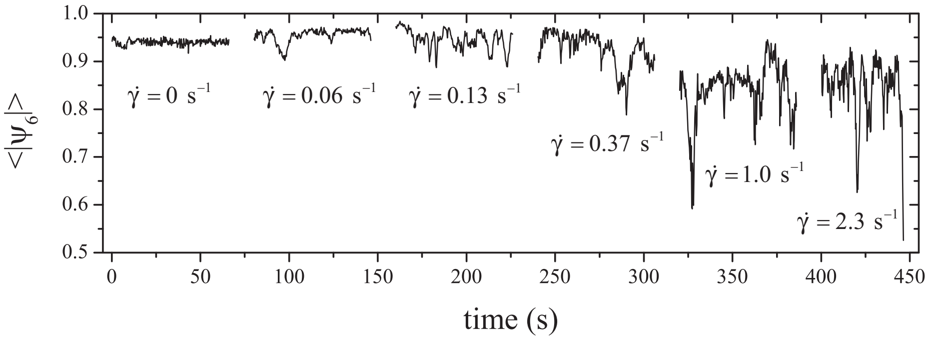

Figure 3.9. The in-plane order expressed as the averaged six fold bond order parameter as a function of time for different shear rates.

order parameter for each particle i:

$$\psi_6(\vec{r_i}) = \frac{1}{N_n}\sum_{j=1}^{N_n} e^{i6\theta(\vec{r}_{ij})}, \tag{3.4}$$

where the summation runs over all nearest neighbors j of that particle, and $\theta(\vec{r}_{ij})$ is the angle between the vector connecting particle i and j and an arbitrary fixed reference axis. We are interested in the global order, and thus take the average of the absolute value of ψ_6 of all particles in a layer at time t. This calculation makes sense only for as long as the particles stay in plane, and is expected to break down close to the melting transition. Still, Fig. 3.9 clearly shows the trend that the average order in the layer decreases with increasing shear rate. Further, it is seen that the order undergoes larger fluctuations. Note that although at the highest shear rate shown we are close to the melting transition, the in-plane order is still considerably high.

To obtain a better insight of the processes going on in the gradient direction, we took time series of the flow gradient plane (snapshots are shown in Fig. 3.10). At zero shear the vertical cross section shows a very regular stacking of layers. When a low shear rate is applied most of the time the layers smoothly slide over each other. Occasionally, it is again observed that a small patch locally melts. Such a disordered region extends over several layers. After a short time crystalline order is restored. These ‘cycles’ were also observed in simulations in which only two layers of particles were sheared (without hydrodynamic interactions) [75]. At higher shear rates the disordered regions become larger and appear more frequently. Finally almost all structure disappears with the exception of a few layers close to the wall. Apparently, the wall promotes the layering [76]. The order-disorder cycles

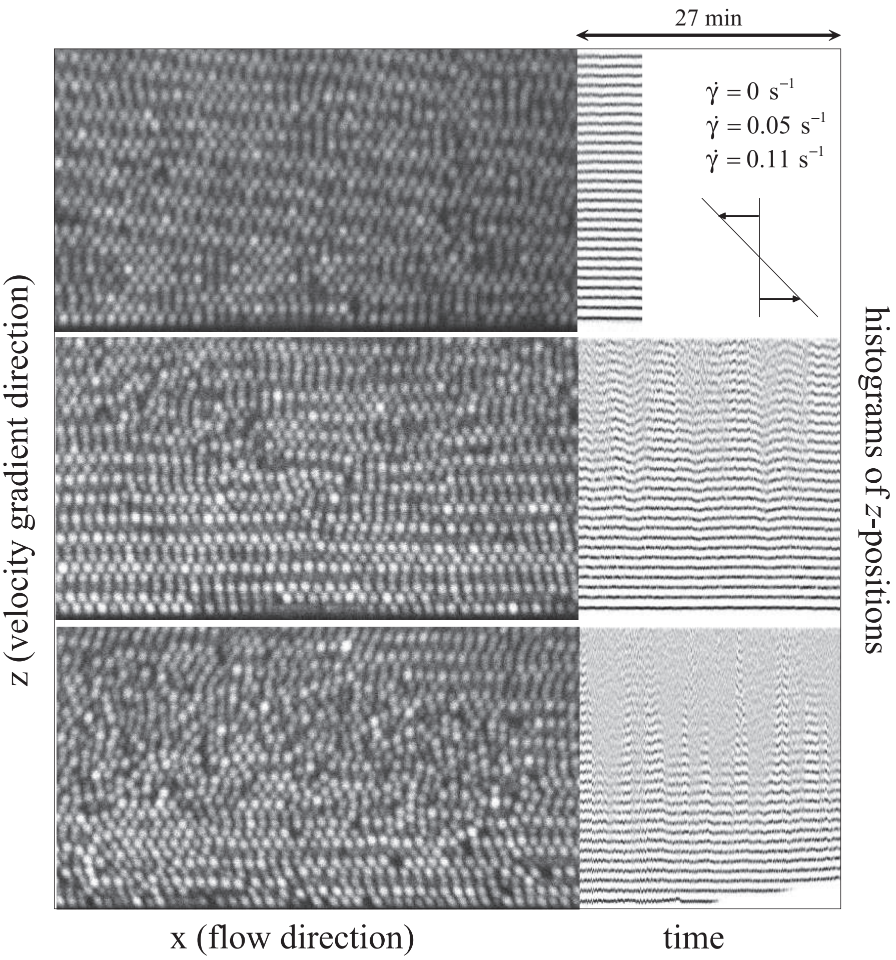

Figure 3.10. (Left) Snapshots (75 x 40 μm^2) of the flow-gradient plane at different shear rates. The time series consisted of 64, 256 and 256 frames respectively with a capturing time per frame of 6.4 s. The apparent elongation of particles in the z-direction is due to the lower z-resolution compared to the xy-resolution. The additional deformation in the lower image results from the fact that the image is scanned line by line and the particles move with the flow during the (slow) scan (see Chapter 2). (Right) The vertical axis is a histogram of the density of particles as a function of height at a given time.

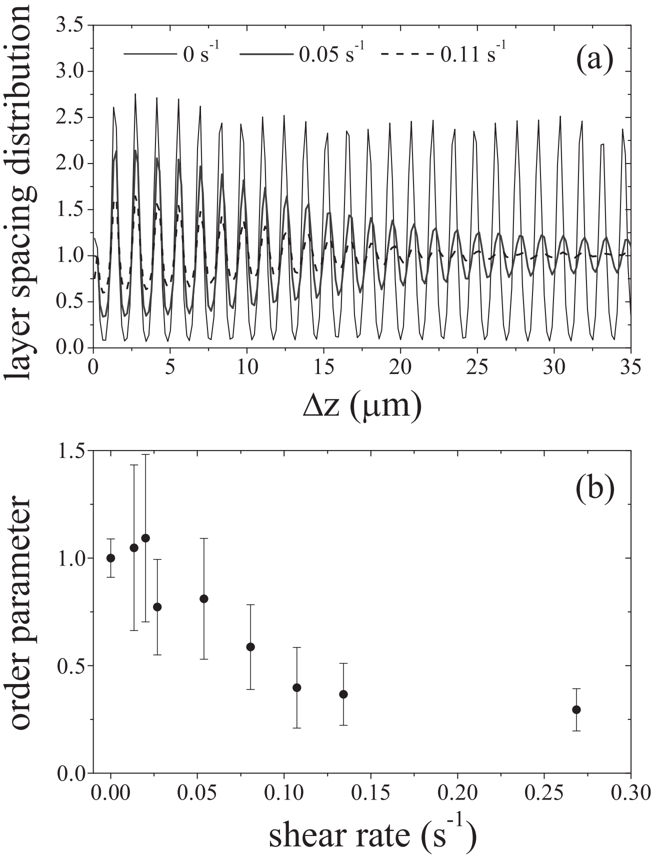

Figure 3.11. Analysis of the degree of layering of the sheared crystals. In (a) we show the height distribution functions (Eq. 3.5) corresponding to the three experiments shown in Fig. 3.10. In (b) an order parameter $\langle|\hat{\rho}^2_{k=2\pi/d}|\rangle(\dot{\gamma})/\langle|\hat{\rho}^2_{k=2\pi/d}|\rangle_{\dot{\gamma}=0}$ with d the inter layer spacing, is given as function of shear rate.

can be seen from the right part of Fig. 3.10, where the particle density is given as a function of height z and time. The histograms of the z-positions are obtained in the same way as in Fig. 3.1. The higher the shear rate the more the layers wander in the z-direction. The fluctuations in z are more pronounced further from the wall.

To quantify these observations we introduce a layer spacing distribution function $g(\Delta z)$. This is done by calculating the histogram of distances between the z-coordinates of every pair of particles in our experiment, and comparing that to a random distribution:

$$g(\Delta z) = \frac{1}{\rho^2} \left\langle \sum_i \sum_{j>i} \delta(z_i)\delta(z_j - \Delta z) \right\rangle , \tag{3.5}$$

where ρ is the average number density. We consider all particle pairs in a frame, and then average over all frames. The results are shown in Fig. 3.11a. Layering is clearly visible. At finite shear rates it is seen that the correlation between layers is gradually lost. The correlation length becomes smaller with increasing shear rate. A closer look at the (summed) layer spacing of these 25 layers further learns that the layer spacing in the sheared system is slightly higher, i.e. 3 %, compared to the non sheared crystal. This now fully explains the period of oscillation measured from Fig. 3.3 as was discussed before.

To quantify the degree of layering we define the following order parameter. We take the power spectrum of the histogram of z-positions of each frame (vertical line in Fig. 3.10), and focus on the peak at the k-value that corresponds to the interlayer spacing d. The height of this peak relative to the peak at zero shear is the order parameter displayed in Fig. 3.11b. The bars represent the standard deviation in the average over frames. They therefore reflect the order-disorder cycles discussed before. At highest measured shear rate the order parameter had not reached zero yet, because still some layering, mostly induced by the wall, remained.

3.4. CONCLUSIONS

In conclusion, we have quantitatively studied colloidal crystals in shear flow in real space by observing both the flow-vorticity plane and flow-gradient plane. We analyzed the collective zigzag motion that the particles perform when hexagonal layers are forced to slide over each other. On top of this collective motion the particles undergo random displacements. Random fluctuations are enhanced by shear flow above those caused by Brownian motion. It was found that those fluctuations cause melting when they become sufficiently large. Similar to equilibrium systems, a Lindemann criterion accurately predicts the melting transition in these non-equilibrium systems. In addition, a dynamic criterion based on the relative importance of the long time diffusion compared to the short time diffusion seems to apply. Finally, we demonstrated that the path to shear melting is accompanied by local and temporary melting of the crystal, as was suggested by recent computer simulations.

ACKNOWLEDGEMENTS

The authors acknowledge all participants in the design of the Wageningen Centre of Food Science (WCFS) shear cell, and especially Jan Dhont. We thank the Instrumentele Groep Fysica (IGF) for the construction of the setup, and Hans Wisman for technical support.

4

Phase Separating Colloid Polymer Mixtures in Shear Flow

Abstract

We study the process of phase separation of colloid polymer mixtures in the (spinodal) two phase region of the phase diagram in shear flow. We use a counter rotating shear cell and image the system by means of confocal laser scanning microscopy. The system is quenched from an initially almost homogeneous state at very high (200 s^{-1}) shear rate to a low shear rate $\dot{\gamma}$. A spinodal decomposition pattern is observed. Initially, the characteristic length scale increases linearly with time. As the structure coarsens, shear imposes a certain length scale onto the structure and a clear asymmetry occurs. The domains become highly stretched along the flow direction, and domain width along the vorticity axis reaches a stationary size, which scales as $\dot{\gamma}^{-1/3}$. Furthermore, by quenching from an intermediate (6.7 s^{-1}) to a low shear rate the elongated structures become Rayleigh unstable and break up into smaller structures. However, the system eventually reaches the same steady state as was found from a direct high to low shear-rate quench through coarsening.

4.1. INTRODUCTION

Fluid-fluid phase separation processes have been the subject of many studies [77], both experimental [78, 79] and theoretical [80, 81]. In part, this is certainly because of the fascinating patterns that spontaneously develop in a system on the way to its most stable state. Understanding this morphology and its kinetics requires answering questions of both hydrodynamic and thermodynamic nature, and is therefore interesting from a fundamental point of view. In this work, we focus on phase separating colloid polymer mixtures in the presence of shear flow. Phase transitions of fluids in shear flow have been reviewed in Refs. [82] and [83]. Insight in the demixing behavior, especially in flow, is also of importance in for example the food industry [84], and polymer processing [85].

Mixtures of colloids and polymers display a rich phase behavior including a colloidal gas phase (poor in colloids, rich in polymers) and a colloidal liquid phase (rich in colloids, poor in polymers). This phase separation occurs at high enough colloid and polymer concentrations, and originates from an effective (depletion) attraction between the colloidal spheres caused by the polymers. The process of phase separation in such mixtures was studied by both small angle light scattering (SALS) [79] and microscopy [79, 86].

The initial stage of demixing is driven by diffusion of individual particles. Since a homogeneous system is unstable in the two phase region of the phase diagram each density fluctuation will have a lower free energy than the initial state and will thus tend to grow further. However, not all wave length fluctuations grow at the same rate, but a fastest growing mode exists, which produces the characteristic length scale of a spinodal structure. With SALS the very initial phase separation can be accessed [79], while microscopy is very suited to study the interfacial tension driven coarsening which immediately follows, after the interfaces have formed on a microscopic scale. As the structures grow larger, gravity is seen to drive the demixing further, leading to the formation of a macroscopic interface as was shown in Ref. [86]. In the present work the phase separation process of the system used for these latter experiments is studied in the presence of a shear flow.

For phase separating polymer-polymer solutions shear experiments were reported by Hashimoto and co-workers [78,87]. Using microscopy techniques a string phase was observed in these systems, where the diameter of a string was seen to decrease with increasing shear rate [78]. On further increasing the shear rate the diameter of those strings approached the interface thickness, at which point the system became homogeneous [87].

In this Chapter we focus on the phase separation of colloid-polymer mixtures in shear flow. First, we describe experiments in which the mixture was brought in a nearly homogeneous state by application of a high shear rate and we investigate the demixing upon quenching to a lower shear rate. The development of the structure was followed in time and compared to experiments in absence of shear. Second, we consider the processes that occur at quenching to low shear rate, when we start off from a non-homogeneous state where highly elongated domains were initially stabilized by an intermediate shear rate.

4.2. EXPERIMENTAL SECTION

We used poly-(methylmethacrylate) (PMMA) spheres with diameter of 50 nm (polydispersity $< 10\%$). They were fluorescently labeled with 7-nitrobenzo-2-oxa-1,3,-diazol (NBD). As polymer we used polystyrene with a radius of gyration of 14 nm. The samples were prepared by mixing stock dispersions of colloids and of polymer, each of which was dispersed in decalin. The resulting colloid and polymer volume fractions in the mixture were $\phi_c = 0.076$ and $\phi_p = 0.50$, respectively. At these concentrations the mixture is in the two phase region of the phase diagram, reasonably near to critical point [88]. After phase separation the volumes of the two phases are roughly equal.

At this state point the system is characterized by an interfacial tension of 2×10^{-7} nN/m and a density difference of 0.053 g/mL as was found by analyzing the thermally induced capillary waves at a freely fluctuating interface [89]. The viscosity was measured by performing rheology experiments on both phases separately, and turned out to be 8 mPas for the gas phase and 31 mPas for the liquid phase [86].

To study the phase separating system under shear a home built counter rotating shear cell was used (Fig. 2.1). This cone-plate shear cell is placed on top of a confocal microscope (Leica TCS SP2) which is used in fluorescence mode (excitation wavelength 488 nm). The colloidal liquid, which contains a high concentration of fluorescent colloids will appear bright, while the colloidal gas phase is darker since the colloid concentration in it is lower. The counter rotating principle of the shear cell allows to locate the stationary layer in the bulk of the cell. We refer to Chapter 2 for further details on the shear cell. In this setup the velocity gradient ∇ is directed along the vertical axis z, parallel to gravity. The flow x and vorticity y direction lie in the horizontal plane. Unless stated otherwise, the images shown are taken in this flow-vorticity plane. A long working distance $20\times$ 0.7 NA objective was used in order to have a large field of view ($750 \times 750\ \mu\text{m}^2$).

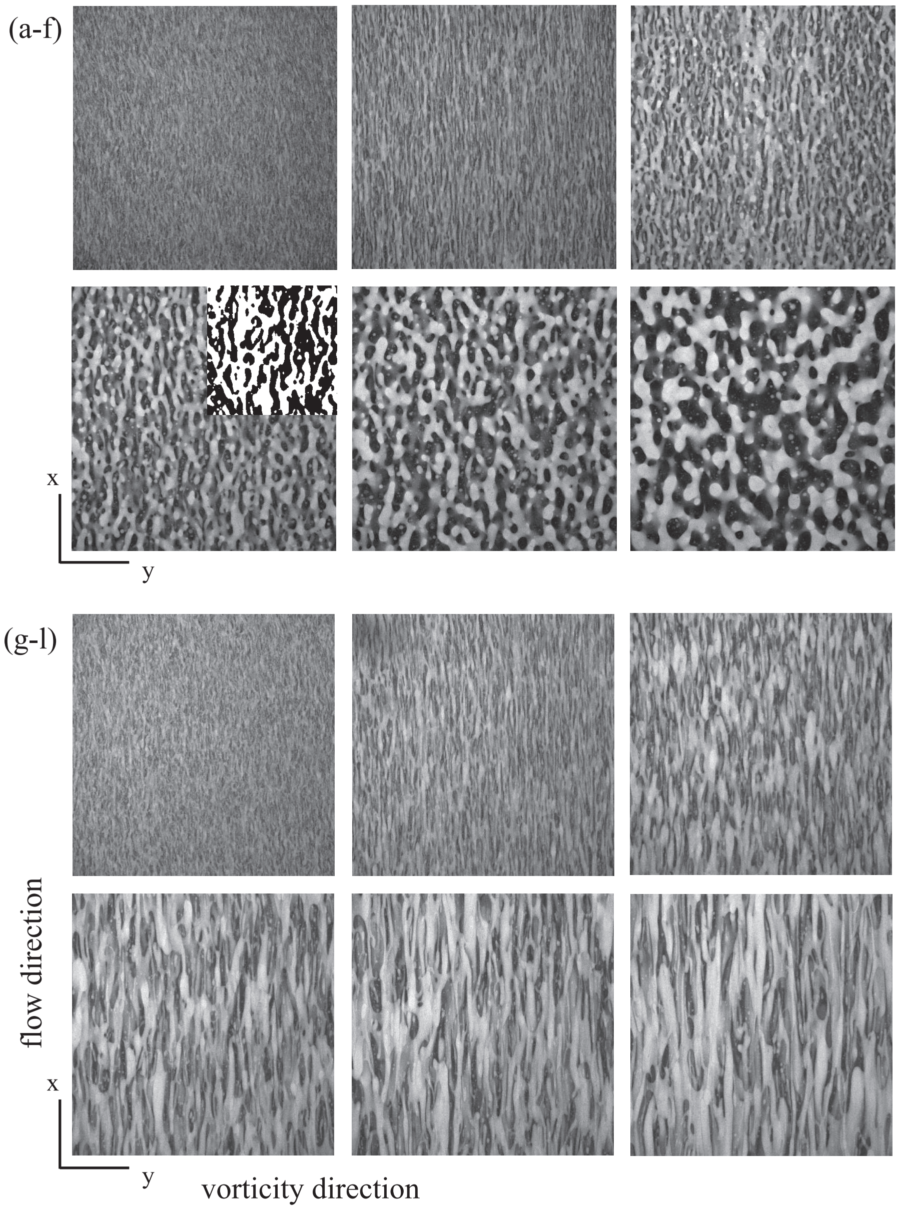

Figure 4.1. Time series showing the process of the demixing after a sudden drop of the shear rate from 200 s^{-1} to no shear (a-f), and to a shear rate of 2.7 s^{-1} (g-l) at $t = 0$ s. Image size is 750 × 750 μm^2. Snapshots correspond to $t = 6.6$ s (a,g), 9.8 s (b,h), 16.4 s (c,i), 21.3 s (d,j), 27.9 s (e,k), and 37.7 s (f,l). The inset in (d) displays part of the image after binarization.

The sample was homogenized (hand shaken) and then brought onto the glass plate of the shear cell. The cone was fixed onto the set up, and brought into measuring position. Immediately after that a high shear rate of 200 s^{-1} was applied. Care was taken to do this procedure quickly in order prevent the system from (macroscopically) phase separating.

4.3. Quenches from high to low shear rate

We applied a high shear of 200 s^{-1} and then followed the process of phase separation after a sudden decrease of the shear rate. The shear cell achieves this drop in about 1 s. Here we first discuss a quench from this high shear rate to no shear at all. A time series was taken immediately after cessation of the shear. In Fig. 4.1 a-f snapshots are shown taken in the first 40 s after the quench. The system is seen to undergo a spinodal decomposition, where a continuous structure coarsens in time. These micrographs do not make it possible to determine whether the system was completely homogenized before the quench. However, it probably was not, since just after the quench the structures are already slightly larger in the flow direction then in the vorticity direction. This indicates that the initial density fluctuations are anisotropic. In time, the system is seen to become more and more isotropic.

In Fig. 4.1 g-l snapshots of a similar quench are shown, but now the final shear rate is 2.7 s^{-1}. The first few seconds the structures resemble the result above, but soon the shear is seen to drastically deform the structure. By imaging vertical cross sections (flow-gradient) we observed that the structures are more or less cylinder-shaped, with two short dimensions (in the vorticity and gradient direction) and one long dimension, along the flow axis (see Fig. 4.7). Interestingly, after about 30 s the length scales in the image appear to remain unaltered, even though the details of the domain structure keep changing continuously. This last observation applies especially to to the vorticity direction. Whether the structures still grow in the flow direction is difficult to tell, since they span over larger distances than the image size.

For this reason we focus our analysis on the length scale in the vorticity direction. We obtain the typical size of a domain directly by binarizing the images: when the intensity of a point is below the average intensity of that image, it is said to belong to the gas phase; when it is above than it is deemed to be part of the liquid phase. The inset in Fig. 4.1d shows an example of such a binarization. Since the contrast between the phases is sufficiently large, the binarized image reproduces the domain structure well. Next, we count in each frame the average number of times an interface is crossed in going from the left to the right. By

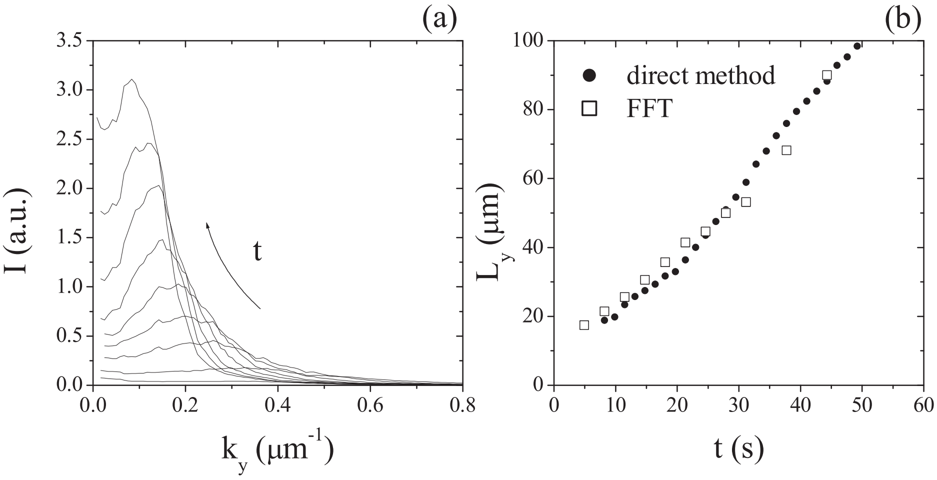

FIGURE 4.2. (a) Analysis of the growth of the characteristic domain size along the vorticity axis of the spinodal structure, which develops after a shear quench from high to zero shear rate (see Fig. 4.1). (b) Both the method using the power spectrum of a Fourier transform and a direct binarization method, in which the number of interfaces along the vorticity direction is counted, lead to a similar curve.

doing this for every horizontal cross-section we obtain the average domain size as a function of time (Fig. 4.2b).

Alternatively, the coarsening rate of phase separation can be found by performing a Fourier transformation (FFT) of confocal images, as was done in Ref. [86], and Chapter 6. This method is analogous to what would be measured in a scattering experiment [79]. The typical size is then obtained from the wave number $k_{\max}$ at the maximum of the power spectrum as shown in Fig. 4.2a.

Both the FFT and the direct method give a similar result, as is shown in Fig. 4.2b, where L_y is defined as the length of a whole period of a fluctuation (including gas and liquid). We find a linear time dependence of the typical structure size, confirming that the coarsening is interfacial tension driven. Moreover, we find that the coarsening rate, obtained from the slope of the graph, is 1.5 - 2 μm/s. This is in agreement with expectations for a sample with this interfacial tension and viscosity as was discussed in Ref. [86].

We use the direct method to find the development of the typical length scales in shear flow. From Fig. 4.3 the difference between the sheared and non-sheared

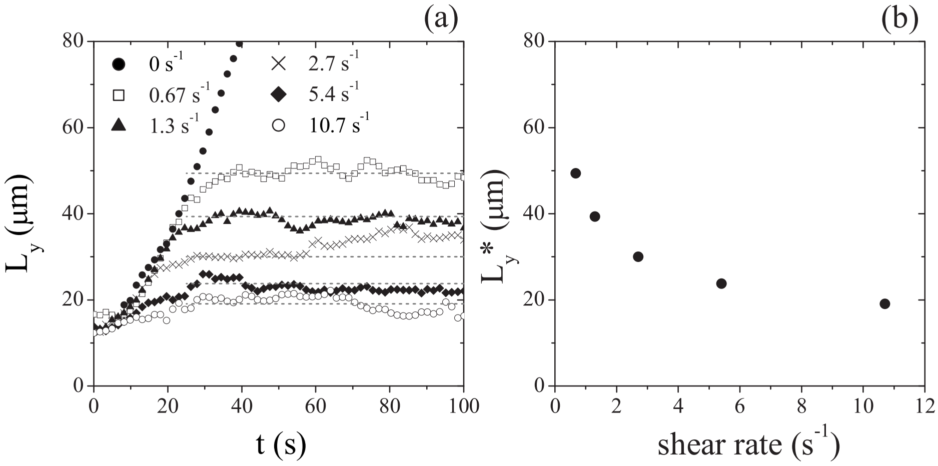

Figure 4.3. (a) Evolution of the characteristic length along the vorticity axis L_y of the spinodal structure (determined by the direct binarization method), which develops after a quench from high (200 s^{-1}) to low shear rate. (b) Final values of L_y after a steady state had been reached.

case becomes clear. While also in the sheared systems the length initially follows a (linear) growth with a shear rate independent growth rate, the length eventually levels off to a constant value. This plateau value is seen to become lower as the shear rate is increased. The gradual change with shear rate from an isotropic structure all the way to very thin threads is visualized in Fig. 4.4, by showing snapshots taken after the plateau value was reached.

The initial phase separation is driven by diffusion processes. In this regime a typical density fluctuation of size L diffuses in a time $t \propto L^2/D$. Here D is its diffusion coefficient, which is given by $D \propto k_B T/\eta L$ with $k_B T$ the thermal energy and η the viscosity. Initially, the typical size of a density fluctuation therefore grows as time to the one-third power [77, 80]:

$$L^3 \propto \frac{k_B T}{\eta} t. \tag{4.1}$$

At this stage the system develops a sharper and sharper interface, with an interfacial tension approaching its equilibrium value σ. It turns out that particles have to diffuse only over a distance in the order of the final interface thickness ($L \propto \sqrt{k_B T/\sigma} \sim \xi$) to develop such an interface. From then on capillary forces will

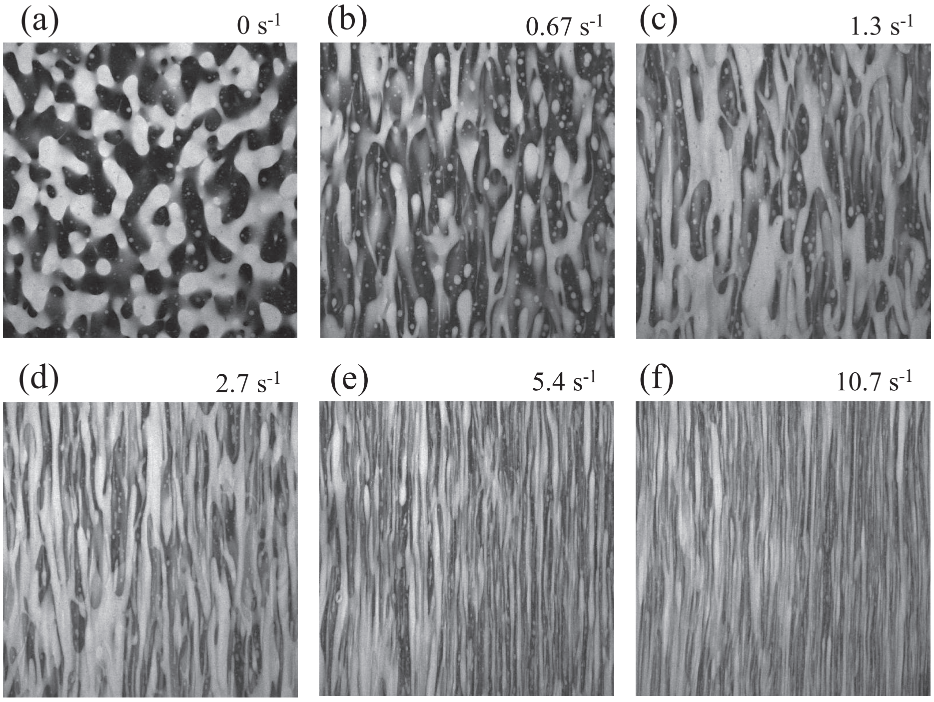

FIGURE 4.4. Snapshots taken 50 s after quenching the system to the shear rate shown. All these images show a steady state, except for the quench to zero shear (a), where in the absence of shear flow the structure continues to coarsen. Image size is 750 ×750 μm^2.

coarsen the structure further, and the free energy is lowered further by reducing the interfacial area. The cross-over occurs already when the structure size is on the order of micrometers, which is the reason why microscopy observes this interfacial tension driven regime and not the diffusive regime.

The coarsening rate in this regime is governed by the Navier Stokes equations [80], and is found by balancing, on one hand, the gradient in pressure over the curved surfaces (∇p) and, on the other hand, the viscous dissipation ($\eta \nabla^2 \vec{u}$). Both quantities can be estimated from the size of the structure L:

$$|\nabla p| \propto \frac{1}{L}\frac{\sigma}{L} \quad \text{and} \quad \eta \nabla^2 u \propto \eta \frac{1}{L^2} u. \tag{4.2}$$

From this we see that, in absence of shear flow, a constant coarsening rate $u \propto \sigma/\eta$ is expected. In shear flow the structure initially coarsens with about the same rate.

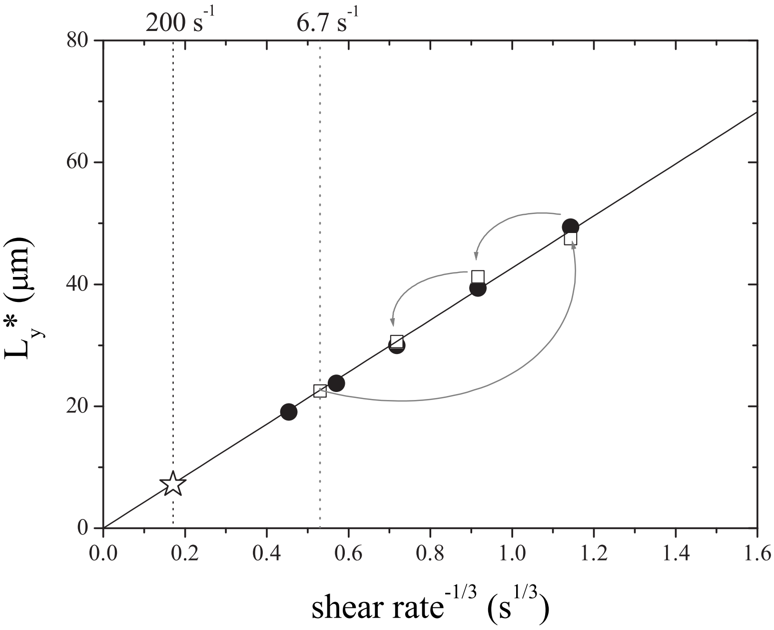

FIGURE 4.5. The plateau value to which the typical domain size along the vorticity direction levels off scales as $\dot{\gamma}^{-1/3}$. (Solid circles) quench from 200 s^{-1}, (open squares) quench from 6.7 s^{-1}.

But, as our experiments show, at a certain point shear begins to strongly affect the spinodal structure and limits the size to which the structure eventually develops in the vorticity and gradient direction.

Can we understand at what length scale this occurs? In the context of polymer-polymer demixing this question was addressed by Onuki [77]. The result he found for the final width along the vorticity direction was:

$$L_y^* \cong \frac{2\pi}{q_m(0)} \left(\dot{\gamma}\tau_\xi\right)^{-\alpha} , \tag{4.3}$$

where $q_m(0)$ is the wave number of the fastest growing mode just after cessation of strong shear, τ_ξ is related to the growth rate of that mode, and $\alpha =$ 1/4 - 1/3. This was also found experimentally in phase separating polymer-polymer mixtures by Hashimoto [78].

In Fig. 4.5 we show that our data indeed scale as $\dot{\gamma}^{-1/3}$. Here the filled circles refer to the quench experiments discussed before. We also indicated the shear rate of 200 s^{-1} from which we quenched. By extrapolating our results to this high shear rate, we can estimate that the typical size connected to the initial structure was ~ 5 μm, which is not quite as thin as the interface (which is the criterium for complete homogenization [87]), but reasonably close.

Qualitatively, we can understand the scaling proposed in Eq. 4.3 by realizing that $2\pi/q_m(0)$ is closely related to the interface thickness ξ, and τ_ξ can be identified with the diffusion time $\tau_D \propto L^2/D$ for $L = \xi$. If we further take $\alpha = 1/3$ as found experimentally, we can rewrite Eq. 4.3 as:

$$L_y^* \propto \left(\frac{k_B T}{\eta\dot{\gamma}}\right)^{1/3}. \tag{4.4}$$

Interestingly, we would have found the same result if we had compared the applied deformation rate $\dot{\gamma}$ to the diffusion time τ_D, directly. The shear controlled regime then starts when $\dot{\gamma}\tau_D > 1$.

4.4. Breakup of elongated domains

Apart from quenching from an initially almost homogeneous state, we can also start at an intermediate shear rate in which we have elongated domains. In Fig. 4.6 we show an example of such an experiment, where we start with bands that are on average 21 μm wide. The process clearly shows different features than before: Thin bands that were initially stable at a shear rate of 6.7 s^{-1}, are seen to break up into droplets after the quench. In fact, the thinnest bands break up immediately, while for wider structures instabilities develop as well, some of which cause break up later on. These instabilities are also observed when we follow a quench in the flow-gradient plane, as is shown in Fig. 4.7.

Finally, when the system coarsens further, the droplets are incorporated into a new continuous structure and the system reaches a steady state again. The domain width we obtain in this way overlaps precisely with the data representing a quench from a high shear rate; see Fig. 4.5. Also, when the shear rate is increased again, as indicated by the arrows, the final size is determined by the scaling we discussed before. From this we conclude that shear drives the system to a unique steady state, although the path which is taken to get there can be different.

The instability of a viscous thread was named after Rayleigh, who was the first to describe this problem correctly. Taylor [41], and Tomokita [90] further analyzed this by taking into account the viscosity of the surrounding fluid. The idea is that a liquid thread becomes unstable to fluctuations in the thickness as a result of differences in Laplace pressure along the length of the thread. The breakup of the droplet into smaller ones is then driven by the decrease of the total interface

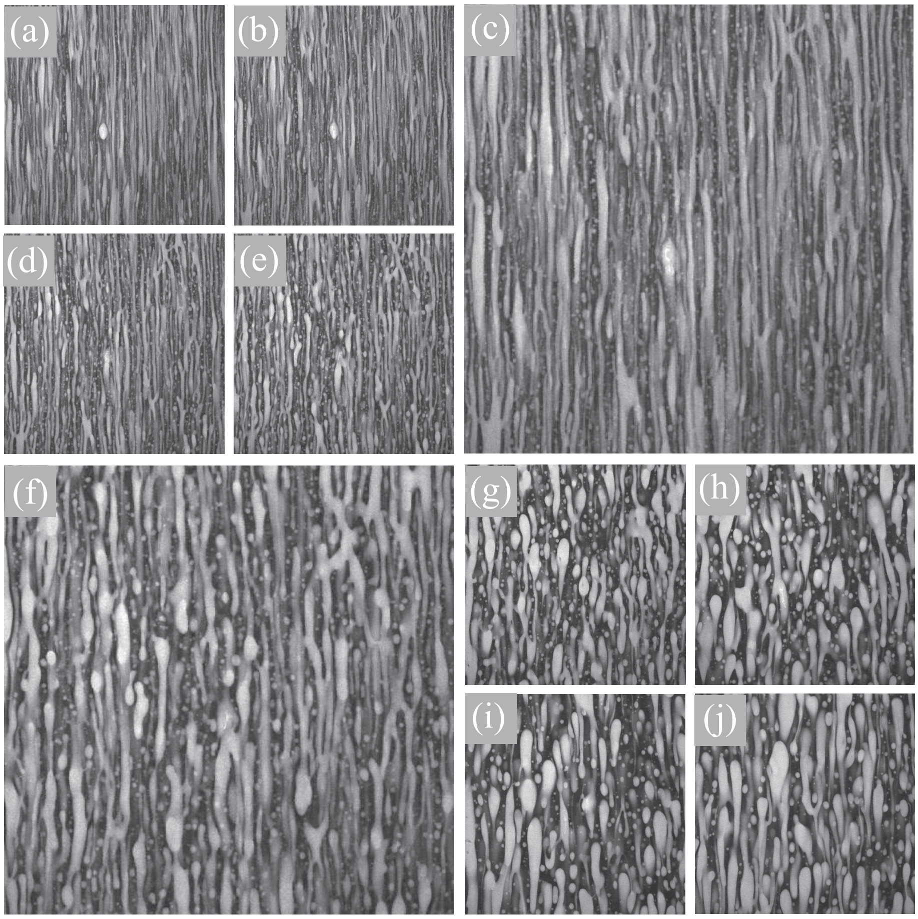

Figure 4.6. Structure evolution after an intermediate-to-low shear rate quench. At $t = 0$ s the shear is dropped from 6.7 s^{-1} to 0.67 s^{-1}. Subsequent images were taken at $t = 1.6$ s (b), 3.3 s (c), 6.6 s (d), 9.8 s (e), 13.1 s (f), 26.2 s (g), 39.4 s (h), 52.5 s (i) and 78.7 s (j).

between two fluids. The fastest growing mode, which determines the size of the resulting droplets, is on the order of the circumference of the thread's cross section.

In colloid-polymer mixtures, the breakup of elongated droplets was studied systematically in a centrifugal field by De Hoog *et al.* [91]. Here a drop of the lower density phase (colloidal gas) was surrounded by the higher density phase (colloidal liquid). The system was brought into a high centrifugal field, in which

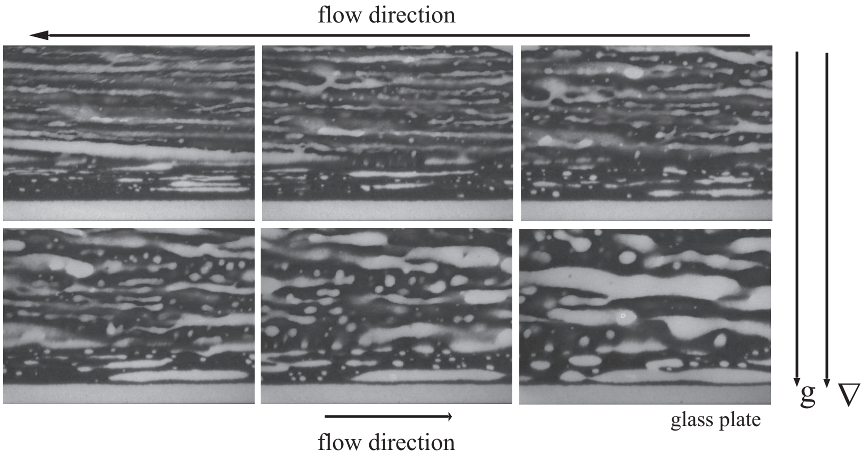

FIGURE 4.7. Snapshots in the flow gradient plane after a quench from high (66 s^{-1}) to a shear rate of 1.3 s^{-1}. Images are taken with 63× oil-immersion objective. Image width is 132 μm; image height is $\sim$ 92 μm.

the droplet was elongated along the spinning axis. The centrifugal rate was then switched to a lower spinning rate. After such a quench in the spinning rate the interface of the cylindrical shaped droplet became unstable, and the wavelength of the fastest growing mode as well as the corresponding growth rate could be determined.

In the present experiments a similar instability takes place in the shear quenches starting from intermediate shear rate. It is clear that the shear modifies the Rayleigh instability. Unfortunately, a theory to describe this phenomenon is not available yet.

4.5. CONCLUSION

The process of phase separation in colloid polymer mixtures under shear was studied in real space by quenching the system from a high shear rate, where the system is almost homogeneous to a much lower shear rate. Initially, the domains are seen to grow linearly in time. Like non sheared systems, coarsening is driven by the interfacial tension that tends to minimize the free energy by reducing the interfacial area. As the domains grow larger there is a point in time, where the spinodal structure begins to be affected by the shear. The domains become highly stretched in the flow direction, while a stationary width is reached in the vorticity direction. The domain width is seen to scale as $\dot{\gamma}^{-1/3}$. This scaling, which has been predicted theoretically and was also experimentally found in polymer-polymer mixtures, is also found in the present experiments. Moreover, we showed that this steady state is unique in the sense that it is eventually reached from any sheared initial state. Finally, when elongated domains are quenched to lower shear rates the growth of the domain widths appears similar to a Rayleigh instability. However, quantitative confirmation of this has to await a theory for the Rayleigh instability under shear.

ACKNOWLEDGMENTS

This work has been performed together with Dirk Aarts. We thank Daniel Bonn for valuable discussions.

5

The Colloidal Gas - Liquid Interface in Shear Flow

ABSTRACT

We investigated the thermal fluctuations of the colloidal gas-liquid interface subjected to a shear flow parallel to the interface. Strikingly, we find that the shear strongly *suppresses* capillary waves, making the interface smoother. This phenomenon can be described by introducing an effective interfacial tension σ_{eff} that increases with shear rate. The increase of σ_{eff} is a direct consequence of the loss of interfacial entropy caused by the flow, which affects especially the slow fluctuations. This demonstrates that the interfacial tension of fluids results from an intrinsic as well as a fluctuation contribution.

5.1. INTRODUCTION

Wind blowing across a lake causes the water surface to ripple. This rippling is resisted by both interfacial tension and gravity. The same forces act at a microscopic scale on capillary waves that exist as a result of thermal agitation [92–94]. In this Chapter we provide the first visual evidence that, contrary to what happens for wind driven waves, flow strongly suppresses thermal interfacial fluctuations. To explain this, we present a simple model based on the idea that shear mostly affects the slow modes, since these couple the strongest to the flow. The observed interface smoothening will have repercussions for the understanding of the flow in, for example, micro- and nanofluidics [23] and during the process of droplet coalescence [95]. In addition, our findings are relevant to studies of shear-induced phase transitions in lamellar systems [96–101].

Thermal capillary waves have been studied extensively in molecular fluids using light [102] and x-ray scattering [103]. Recently they have also been visualized directly with a confocal microscope in a phase separated colloid-polymer mixture [89], where excellent agreement with capillary wave theory was found. This model system has the unique property that the interfacial tension is extremely low: on the order of $10^{-9} - 10^{-6}$ N/m [89, 104–106]. Thus, the amplitudes of the waves are much larger (micrometers versus nanometers) than those on the interface of molecular liquids, while their in-plane correlation length is much shorter (micrometers versus millimeters). Here, we use this system to investigate the effect of a shear flow on a freely fluctuating interface with a recently developed counter-rotating shear cell (see Chapter 2) in real space.

The effect of shear flow has been considered more extensively in the context of lamellar systems in order to explain certain shear-induced phase transitions. In these systems the restoring force is not the surface tension but the bending elasticity of the lamellae or smectic layers. Cates and Milner predicted that, by reducing the undulations of the lamellae, shear can stabilize a lamellar phase relative to an isotropic phase, leading to an increase in the transition temperature [96]. Such an increase was indeed observed in a diblock copolymer melt [100] and a lamellar surfactant solution [99]. Bruinsma and Rabin predicted a similar suppression of undulations for smectic liquid crystals [97]. In the case of a lyotropic lamellar phase this was predicted to cause a reduction of steric repulsions between the layers, ultimately leading to their destabilization. Indirect experimental evidence for this model was obtained by Yamamoto and Tanaka, who observed a reduction of the interlayer spacing with shear and a reduced correlation length perpendicular to the lamellae [98]. Marlow and Olmsted modelled the effect of shear as

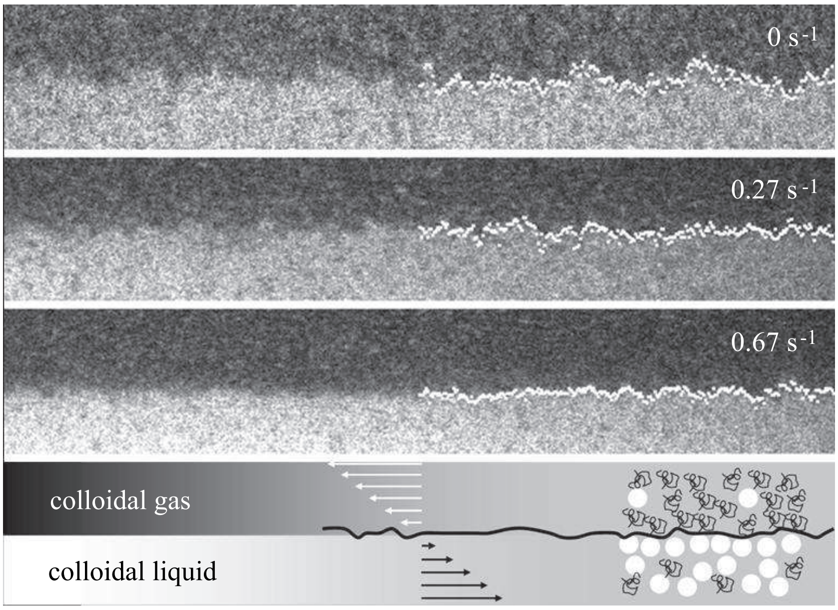

Figure 5.1. Snapshots of the interface of sample A, closest to the critical point, at three shear rates. Each image is 18 × 106 μm^2 and shows a vertical cross section through the interface. The position of the interface is indicated with bright pixels. The bottom panel schematically shows the flow geometry with the plane of zero velocity located at the interface.

an anisotropic tension in the layers resulting from a stretching of the undulations by the flow [107]. Zilman and Granek [101] incorporated the shear as an affine deformation of the thermally excited undulations, and proposed that the ensuing instability could be a mechanism for the lamellar-to-onion transition. In view of these studies it is of significant fundamental interest to study the effect of shear on interface fluctuations, experimentally.

5.2. Methods and materials

We used fluorescently labelled poly(methyl methacrylate) (PMMA) colloidal spheres with radius 71 nm and size polydispersity less than 10% dispersed in decalin. The polymer was polystyrene (Fluka, molecular weight 2×10^6 g/mol) with radius of gyration 43 nm [108, 109]. Samples were prepared by mixing stock dispersions. The phase diagram of this mixture has been determined before [89]. In the present work we used two compositions in the two-phase region of the phase diagram; one was close to the critical point (sample A), the other further removed (sample B). A sample was loaded into the shear cell, which was placed on a Leica TCS-SP2 inverted confocal scanning microscope equipped with a 100× 1.4 NA oil immersion objective, and allowed to fully phase separate for 24 hours. For details of the setup and its performance we refer to Chapter 2. Briefly, the shear cell is a counter-rotating cone-plate cell. The bottom plate consisted of a 6 cm diameter no. 1 cover slip, while the metal cone had an angle of 1 degree. The spacing between plate and cone at the position of the objective was 430 μm. By rotating the cone and plate in opposite directions a simple shear flow was created with a (nearly) horizontal plane of zero velocity (ZVP). Objects in this plane remain stationary with respect to the lab frame while shearing. The vertical position of the ZVP was carefully adjusted to the horizontal gas-liquid interface (at a height of ~ 50 μm above the glass plate) by varying the relative rotational velocities of cone and plate. Thus, a fixed section of the interface remains in focus during the experiment. This is essential for visualizing details of the interface without any blurring caused by the motion. At each shear rate a time series was recorded of the flow-gradient plane for typically 20 minutes at a frame rate of 1.5 Hz (0.67 s/frame).

5.3. EXPERIMENTAL OBSERVATIONS

Snapshots of the interface in a phase separated colloid polymer mixture are shown in Fig. 5.1. The lower ('liquid') phase is dense in fluorescent colloids and thus appears bright, while the upper ('gas') phase is poor in colloids. The particles are too small to be resolved individually by the microscope, but the rough interface separating the phases can be clearly observed. Though the applied shear is too small to significantly affect the thermal motion of individual particles (Pe $= \eta\dot{\gamma}d^3/k_BT < 0.1$ for all experiments), the interfacial roughness is visibly reduced as the shear rate $\dot{\gamma}$ is increased. This situation is stationary in time. Turning off the shear immediately restores the equilibrium fluctuations. The vertical location of the interface $h(x)$ is determined for each column of pixels in a frame by fitting the pixel value $I(z)$, which is proportional to the local colloid concentration, to a van der Waals profile

$$I(z) = a + b\tanh\left(\left(z - h(x)\right)/c\right). \tag{5.1}$$

The position thus found is shown in Fig. 5.1 and is seen to describe the interface well. We obtain the probability distributions of the interface height for different shear rates (Fig. 5.2 a,b). Under shear, these remain Gaussian but have a reduced width reflecting the strong suppression of the roughness. This is confirmed in

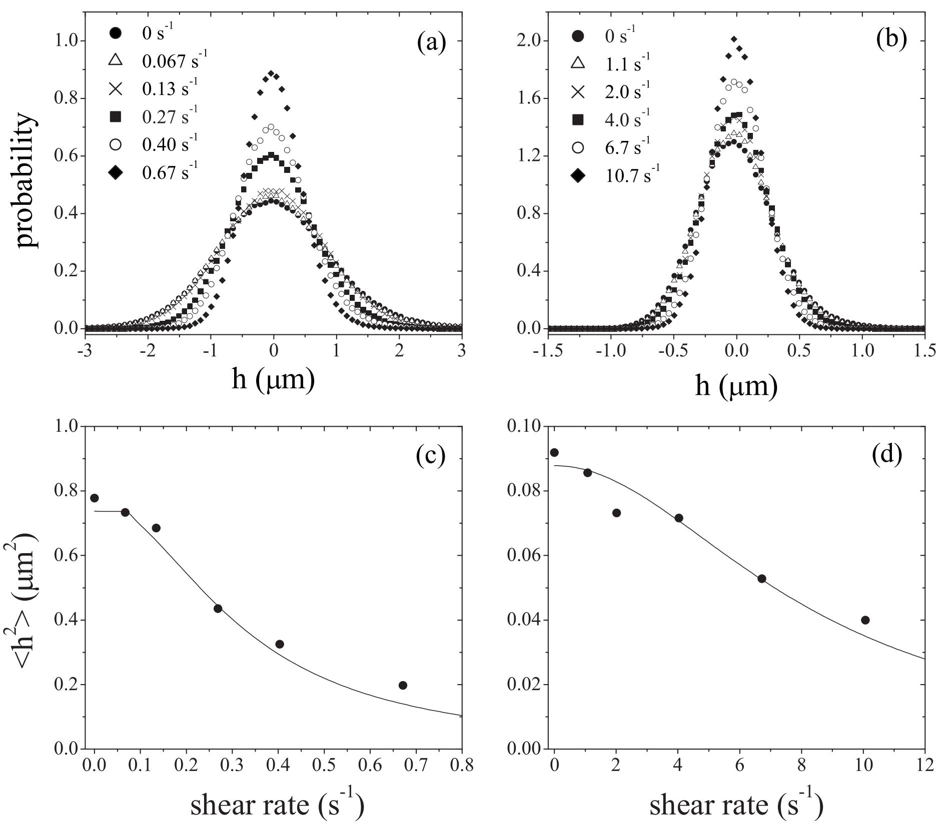

FIGURE 5.2. Analysis of the interfacial roughness of gas-liquid interfaces in shear flow. Graphs (a) and (b) show the height distribution for state point A and B. In (c) and (d) the mean square interfacial height is plotted against the shear rate.

Fig. 5.2 c,d where the mean square interfacial height $\langle h^2 \rangle$ is plotted against the shear rate. Sample B, further from the critical point, shows a smaller roughness than A and requires larger shear rates to reduce the roughness.

Next, we calculate the autocorrelation function of the interface height $g_h(x) = \langle h(x+x')h(x') \rangle$, where the angular brackets denote averaging over the primed quantities (see Fig. 5.3). For a non-sheared system the theory of independent capillary wave fluctuations [110] predicts

$$g_h(x) = \frac{k_B T}{2\pi\sigma} K_0\left(x/\xi\right), \tag{5.2}$$

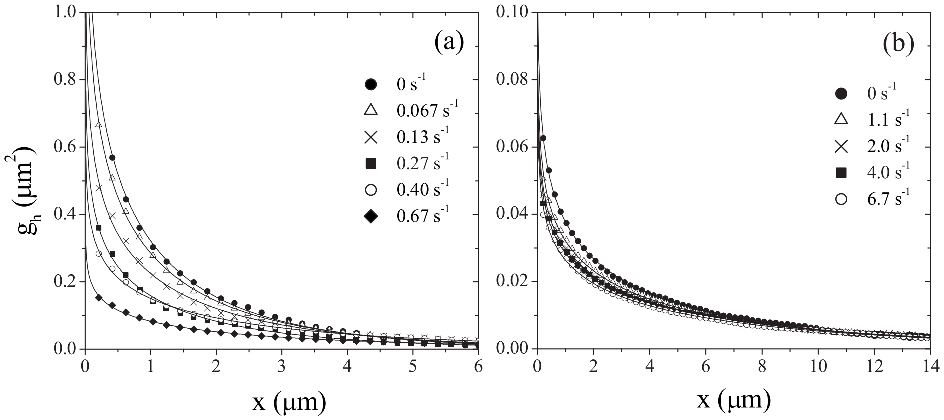

FIGURE 5.3. Static correlation functions of the interfacial height for state point A (a) and B (b) fitted with Eq. 5.2.

where K_0 is the modified Bessel function of the second kind. The interfacial tension σ determines the mean-square height, or roughness, of the interface and the in-plane correlation length ξ equals the capillary length $L_{\mathrm{cap}} = \sqrt{\sigma/g\Delta\rho}$, with g the acceleration of gravity and $\Delta\rho$ the density difference between the phases. From a fit we find these equilibrium properties for the two state points under study (Table 5.1).

TABLE 5.1. Physical properties of the equilibrium system at state point A, near the critical point, and state point B, away from the critical point. The interfacial tension σ, capillary length L_{cap} and the capillary time τ_{cap} are directly obtained from the correlation functions of the interface height at zero shear. The density difference $\Delta\rho$ and viscosity η are calculated from these values.

		state point A	state point B
σ	(nN/m)	2.5	36
L_{cap}	(μm)	2.6	8
τ_{cap}	(s)	13	6
$\Delta\rho$	(g/mL)	0.038	0.057
η	(mPa s)	13	28

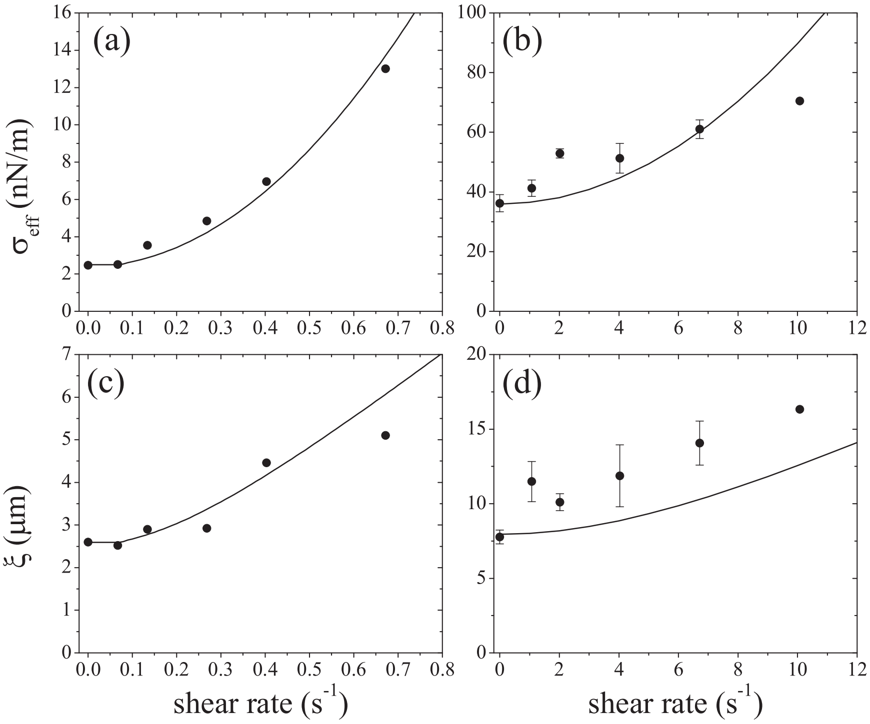

Figure 5.4. The effective interfacial tension σ_{eff} (a) and (b), and the in plane correlation length ξ (c) and (d) as obtained by the fits in Fig. 5.3, for state point A and B, respectively.

Interestingly, we find that also for the sheared interfaces the shape of the correlation function obeys Eq. 5.2, only with different parameters characterizing its decay (Fig. 5.3). This leads to the surprising conclusion that, in the experiment, the interface under shear cannot be distinguished from an equilibrium interface with a different interfacial tension. Hence, to the sheared systems, we can assign an *effective* interfacial tension σ_{eff} and a correlation length ξ, which is not necessarily equal to the capillary length. Clearly, both the effective interfacial tension and the correlation length increase significantly with shear rate (Fig. 5.4).

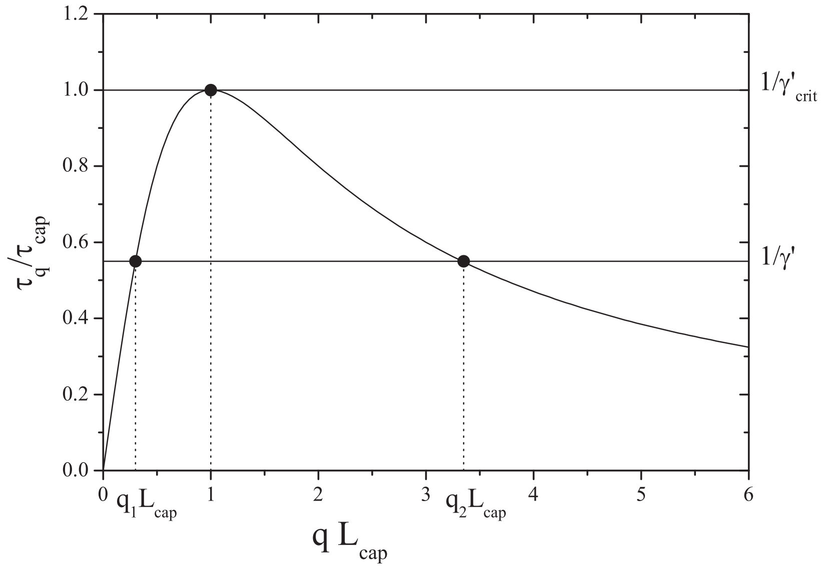

FIGURE 5.5. Dispersion relation of the relaxation times of capillary waves in the overdamped regime (Eq. 5.3). Below a critical shear rate $\dot{\gamma}_{\rm crit} = 1/\tau_{\rm cap}$ no significant shear effect is expected. At higher shear rates $\dot{\gamma} > \dot{\gamma}_{\rm crit}$ the effect of shear will be larger as the number of slow modes ($q_1 < q < q_2$) increases.

5.4. THE EFFECTIVE INTERFACIAL TENSION

Why shear would increase the measured interfacial tension can be understood as follows. The interface will start to feel the presence of a shear when the applied shear rate approaches the relaxation rate of the fluctuating waves (see Fig. 5.5). We determine the lifetime of the capillary wave fluctuations from the dynamical height autocorrelation functions $g_h(t) = \langle h(t+t')h(t')\rangle$ at zero shear, as described previously [89]. These experimentally measured time correlation functions are plotted in Fig. 5.6 for both state points in equilibrium. Capillary wave theory in the overdamped regime predicts [111] that a mode with wave vector q decays exponentially in a time

$$\tau_q = \tau_{\rm cap}\frac{2qL_{\rm cap}}{1+q^2L_{\rm cap}^2}. \tag{5.3}$$

Here the capillary time $\tau_{\rm cap}$ equals $\eta L_{\rm cap}/\sigma$ and η is the sum of the viscosities of the two phases. From this dispersion relation an expression for the dynamic

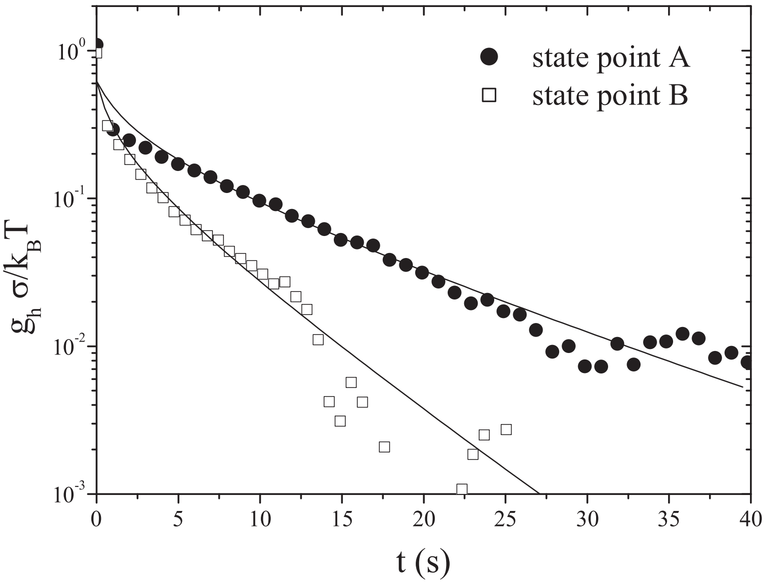

Figure 5.6. Experimental dynamical correlation functions of the interfacial height of the interface at equilibrium. From the fits with theory (lines) [89, 111] we obtain the capillary time τ_{cap}.

height correlation function was derived [89] to which our experimental data are fitted. The obtained capillary times are listed in Table 5.1. We thus expect that if $\dot{\gamma}\tau_{\text{cap}} > 1$ the fluctuations begin to be affected. Solving $\dot{\gamma}\tau_q > 1$ leads to two solutions, q_1 and q_2, bounding the range of wave numbers affected by shear (see Fig. 5.5).

How do these shear-affected waves translate into an effectively higher interfacial tension? The usual model of a fluid interface is that of an intrinsic profile, as calculated for instance in the mean-field theory of van der Waals [112], supplemented with fluctuations described by capillary wave theory [93, 94]. Buff, Lovett and Stillinger [113] find that the measurable interfacial tension σ is then a sum of a "bare" interfacial tension σ_0 and a negative contribution to the surface free energy due to the entropy of the capillary wave fluctuations:

$$\sigma = \sigma_0 - \frac{3}{16\pi} k_B T q_{\text{max}}^2. \tag{5.4}$$

Here, q_{max} corresponds to a microscopic cut-off length. This result can be found by assigning $\frac{1}{2}k_B T$ to each mode using the equipartition theorem and subsequently integrating over all modes. When shear is present, we assume that the shear-affected waves no longer contribute to the entropic lowering of the interfacial tension. Thus, we perform the integration leading to Eq. 5.4, but exclude the range $q_1 < q < q_2$. This results in a smaller reduction of the interfacial tension. The *effective* interfacial tension that follows from this calculation is:

$$\sigma_{\mathrm{eff}}(\dot{\gamma}) = \sigma + \frac{3k_BT}{4\pi}\frac{\dot{\gamma}\tau_{\mathrm{cap}}}{L_{\mathrm{cap}}^2}\sqrt{(\dot{\gamma}\tau_{\mathrm{cap}})^2 - 1}, \tag{5.5}$$

with σ the interfacial tension at zero shear.[1] All parameters going into Eq. 5.5 are determined from the experiment at zero shear rate (Table 5.1). This allows for a direct comparison with the data. Without any adjustable parameters we find good agreement for both state points (Fig. 5.4 a,b). Note that the second term in Eq. 5.5 is independent of our choice for q_{max} and depends, approximately, quadratically on the shear rate. Interestingly, a similar quadratic increase was found in recent simulations of homogeneous nucleation of colloidal crystals under shear [114]. In our model a change in the interfacial tension will also result in an increased correlation length, since $\xi(\dot{\gamma}) = \sqrt{\sigma_{\mathrm{eff}}(\dot{\gamma})/g\Delta\rho}$, where the density difference between the two phases is assumed to be the same as in equilibrium. Again, this is seen to be the case for state point A (Fig. 5.4c); for state point B (Fig. 5.4d) the trend is similar while the departure is possibly due to difficulties of determining a relatively large L_{cap} in a limited observation window. Since the mean square interfacial roughness is inversely proportional to the interfacial tension ($\langle h^2\rangle_{\dot{\gamma}=0} \propto k_BT/\sigma$), the model predicts that the amplitude of the capillary waves depends on the shear rate as $\langle h^2\rangle(\dot{\gamma}) = (\sigma/\sigma_{\mathrm{eff}}(\dot{\gamma}))\langle h^2\rangle_{\dot{\gamma}=0}$ (Fig. 5.2 c,d). Here we ignore a small logarithmic correction caused by the change in correlation length. We find that this simple calculation provides excellent quantitative agreement with the experimental data, without any adjustable parameters. Remarkable is the huge impact of shear when approaching the critical point. According to our model a lower interfacial tension, a longer capillary time, and a shorter capillary length all work to increase $\sigma_{\mathrm{eff}}/\sigma$. Experimentally, this is exactly what we find, leading to a reduction of the mean square roughness of up to a factor 5.

---

[1] To obtain Eq. 5.5 we used thermodynamic arguments to exclude slow waves from contributing to σ_{eff}. Alternatively, the effect of shear on interfacial fluctuations can be estimated by calculating the free energy cost of capillary waves deformed by shear. For this, we refer to the appendix of this Chapter. Interestingly, such a derivation results into an expression for an effective surface tension as well. Moreover, it includes the same physical parameters as we found here, and differs only in the numerical pre-factor.

5.5. THE EXPERIMENTAL INTERFACE IN MORE DETAIL

5.5.1. Measuring the velocity profile over the gas-liquid interface

In the preceding discussion we presumed each experiment to occur at a certain, applied, shear rate. Since we focus on the interface dividing two different phases, it will be informative to actually measure the flow profile over the interface experimentally. In the previous chapters it was required to observe individual particles, and track their displacements between subsequent frames. This is not possible in the present system. However, here we have density (intensity) fluctuations which could be tracked if they are sufficiently pronounced. In addition, these bulk fluctuations should move over less than the bulk correlation length in the time interval between two frames. Furthermore, this time interval should be (considerably) shorter than the typical life time of such a bulk density fluctuation. These criteria are met for the data for state point A, as is seen qualitatively by eye: When playing the time series as a movie, the fluctuations in the upper gas phase flow leftwards, whereas those in the lower liquid phase are seen to move to the right. This observation can in a straightforward way be quantified by dividing each image into horizontal slices with height Δh, and cross-correlating each such slice in two successive frames. The location of the maximum of this cross-correlation function

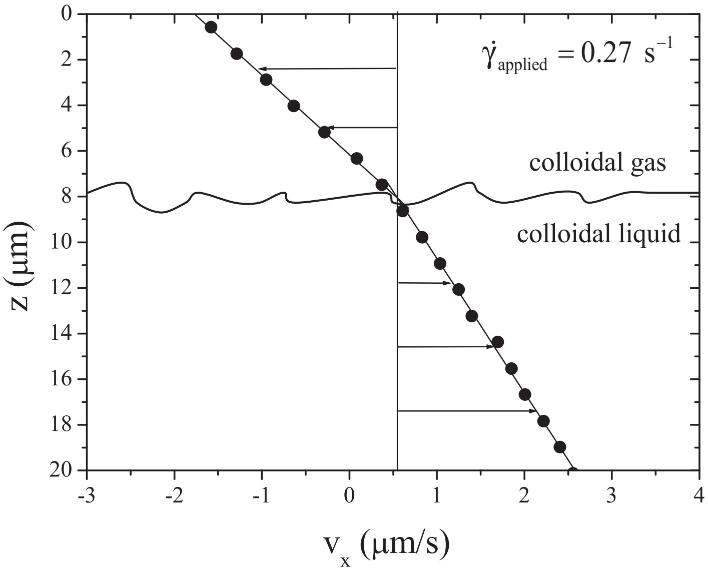

FIGURE 5.7. Measured velocity profile in sample A while a shear rate of 0.27 s^{-1} was applied. A slight kink in the velocity gradient is observed at the gas-liquid interface.

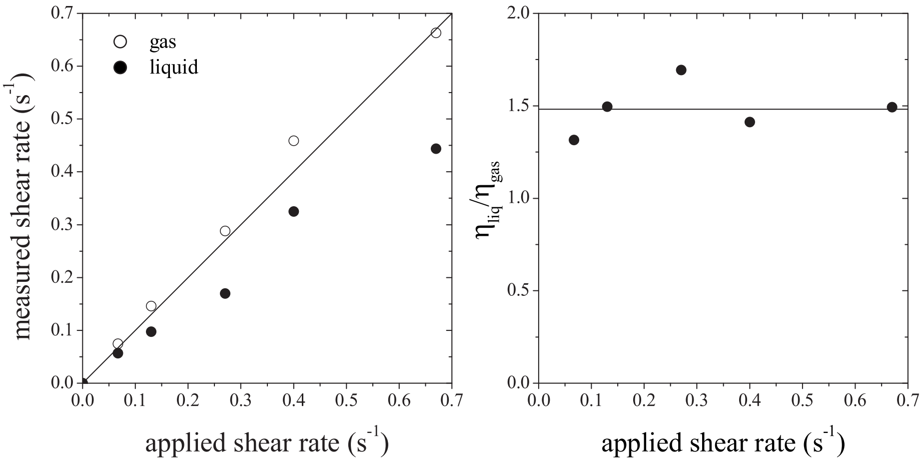

FIGURE 5.8. (Left) Measured shear rate in both the gas and liquid phase as a function of the applied shear rate. (Right) The corresponding viscosity ratio of liquid and gas phase.

is then directly proportional to horizontal velocity at that height. Repeating this exercise for slices at different heights results in the velocity profile $v_x(z)$, as shown in Fig. 5.7 for an applied shear rate of 0.27 s^{-1}. Note, that the zero velocity plane (ZVP) was located close to, but not exactly at, the interface (indicated by the wavy line). The interface flows with velocity of $\sim$ 0.5 μm/s, while the ZVP lies 1.5 μm higher, in the gas phase.

The most interesting observation seen from Fig. 5.7 is that the velocity profile is nicely linear, but with a kink at the gas-liquid interface. In fact this is in accordance with the Navier-Stokes equations when taking into account the appropriate boundary conditions. For a homogeneous fluid in our shear cell configuration there is no gradient in pressure which reduces the Navier-Stokes equations to $\eta\nabla^2\vec{v} = 0$, resulting in a constant velocity gradient over the gap of the cell. Since our system consists of two phases, an extra boundary condition comes into play where those two phases meet. The boundary condition at a fluid-fluid interface (for incompressible fluids) states that there is no in-plane stress difference present at this interface [111, 115]. This continuity of the stress in the horizontal direction then gives: $\tau^G_{xz} = \tau^L_{xz}$, where $\tau_{ij} = \eta(dv_i/dj + dv_j/di)$ and G and L refer to the gas and liquid phase, respectively. Clearly, the velocity in the z-direction averages out to zero. Thus, the ratio of the velocity gradients of the two phases is inversely proportional to the ratio in viscosities:

$$\eta_G\dot{\gamma}_G = \eta_L\dot{\gamma}_L. \qquad (5.6)$$

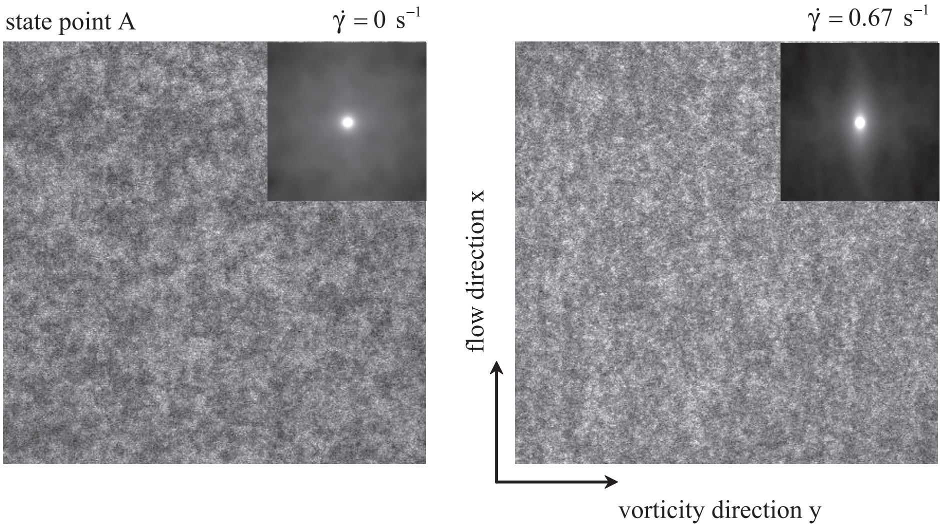

Figure 5.9. Cross-sections through the interface of sample A in rest (left) and undergoing shear flow with $\dot{\gamma} = 0.67\ \mathrm{s}^{-1}$ (right). Image size is $83 \times 83\ \mu\mathrm{m}^2$. Bright regions indicate the liquid phase, dark regions the gas phase. The insets show the autocorrelation function averaged over a time series of 100 frames.

In Fig. 5.8 we show that at all applied shear rates a lower shear rate is measured in the liquid than the gas phase. From these results and Eq. 5.6 we find that the viscosity of the liquid phase is approximately 1.5 times larger than that in the gas phase. Such a small viscosity difference in a near-critical sample, is in accordance with previous rheology measurements on the two phases separately on similar samples [86].

5.5.2. Flow-vorticity anisotropy

An additional interesting factor (that was not considered in the model described above) accompanying the application of shear to an interface is the possible breaking of the in-plane symmetry. Recalling the observations described in Chapter 4, it is actually to be expected that fluctuations will be affected differently in the flow direction than in the direction perpendicular, i.e. the vorticity direction. To obtain a qualitative idea whether there is such an effect, time series were recorded in this flow-vorticity plane, by focussing in (the middle of) the interface. Typical images are presented in Fig. 5.9. Higher and lower intensities correspond to the liquid (where the focal plane is locally above the interface) and the gas (interface locally below the focal plane), respectively. It is seen that in shear flow indeed a slight anisotropy is observed. This is highlighted by the 2D-autocorrelation functions in the insets. From the ratio in correlation length l along the flow direction and the vorticity direction, we estimate a value for the anisotropy of $l_{\text{flow}}/l_{\text{vort}} \approx 1.5$. Clearly, more work is needed to study the shear rate dependence of this anisotropy.

5.6. CONCLUSIONS

In conclusion, we find that a shear flow with its gradient applied perpendicular to a fluctuating interface reduces thermal capillary waves, in clear contrast with wind driven waves. A similar phenomenon is predicted to play a key role in flow-induced phase transitions in membrane systems [96–101]. We show that the suppression of thermal fluctuations at a fluid interface can be understood from a coupling of the flow with the fluctuations. Interestingly, the experimental correlation functions can be accurately described by the theoretical result for the equilibrium case, indicating that all fluctuation modes still appear in the same relative proportions. Assuming that too slow modes, while still present, no longer contribute to the entropy of the interface allows prediction of an effective interfacial tension, correlation length and interfacial roughness. This produces quantitative agreement with our experimental data. The success of equilibrium theory and the formulation of a more complete hydrodynamic theory of the flow-fluctuation coupling are now clearly put as theoretical challenges. We hope that elucidating experimental details of the sheared interface, such as the observed kink in velocity profile at the interface and an anisotropy of flow and vorticity direction, might contribute in finding such a description. Perhaps the most important conclusion is that assuming a partial suppression of the fluctuations leads to an increase in the effective surface tension. This is to our knowledge the first direct experimental confirmation of the dual nature of fluid interfaces, with a high surface tension due to the intrinsic density profile that is lowered by the entropy of the fluctuations. Further investigation is necessary to see whether our findings allow to completely reconcile the two models, a central point for our understanding of fluid interfaces.

ACKNOWLEDGMENTS

The work described in this Chapter was performed together with Dirk Aarts, Daniel Bonn and Henk Lekkerkerker, whom we gratefully thank for the nice collaboration. Furthermore, we would like to thank Denis Bartolo, Andrea Fortini, Jos Zwanikken, René van Roij and Jacques Meunier for fruitful discussions.

Appendix: An alternative description of the sheared interface

Here, we aim to understand what happens to a rough interface subjected to shear at a microscopic level. Therefore we extend the capillary wave model with a shear term. This term accounts for the fact that a wave gives a larger contribution to the microscopic area of a certain amplitude corresponds to a larger microscopic interfacial area when it is deformed by shear, than it would in equilibrium. Since this corresponds to a larger free energy the system will try to lower its free energy by reducing the amplitudes of the capillary waves.

Shear deformation of a wave

A certain (sinusoidal) undulation of the interface will change shape in the presence of shear flow. In case the original wave is described by $h(x)$, then shear will cause a horizontal translation of each point, such that:

$$(x, h(x)) \mapsto (x + \alpha h(x), h(x)) \,. \tag{5.7}$$

Here $\alpha = \dot{\gamma} t$ is the strain, and $\dot{\gamma}$ is the shear rate and t the time during which the wave is exposed to shear. x now serves to parameterize the wave.

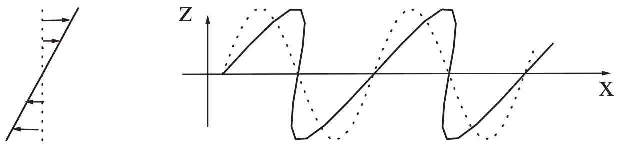

The strain α changes the arc length of the wave:

$$\begin{aligned} dl &= \sqrt{(dx + \alpha dh)^2 + (dh)^2} \\ &= \sqrt{\left(1 + \alpha \frac{dh}{dx}\right)^2 + \left(\frac{dh}{dx}\right)^2}\, dx. \end{aligned} \tag{5.8}$$

Initially, the length of an ascending slope will be extended, while the descending slope will be shortened. Due to the parametrization this expression is still valid when the deformed waves “overhang”.

This has consequences for the interfacial area as well. We include the vorticity direction y to find the (microscopic) area S of a strained 2D interface. An infinitesimal area dS is given by the magnitude of the cross product of the vectors $(dx + \alpha dh, 0, dh)$ and $(0, dy, dh)$:

$$dS = \sqrt{\left(1 + \alpha \frac{dh}{dx}\right)^2 + \left(\frac{dh}{dx}\right)^2 + \left(1 + \alpha \frac{dh}{dx}\right)^2 \left(\frac{dh}{dy}\right)^2}\, dxdy. \tag{5.9}$$

From this equation we see that shear deformation will become significant when $\alpha = (dh/dx)^{-1}$. Expanding Eq. 5.9 in a Taylor series up to the 4th order term gives:

$$\frac{dS}{dxdy} = 1 + \alpha h_x + \frac{1}{2} h_x^2 + \frac{1}{2} h_y^2 - \frac{\alpha}{2} h_x^3 + \frac{\alpha}{2} h_x h_y^2 - \frac{1}{8} h_x^4 - \frac{1}{8} h_y^4 - \frac{1}{4} h_x^2 h_y^2 + \frac{\alpha^2}{2} h_x^4. \tag{5.10}$$

Capillary wave theory extended with shear

To create a perturbed and strained interface requires work to be performed against interfacial tension ($dF_c = \sigma dS$) and gravity ($dF_g = \frac{1}{2} g\Delta\rho h^2 \; dxdy$). Here σ is the interfacial tension, and $\Delta\rho$ the density difference between the two phases. Integrating over the total interface area gives:

$$\Delta F_c = \frac{1}{2}\sigma \int\int dxdy \; \left[\left(\frac{dh}{dx}\right)^2 + \left(\frac{dh}{dy}\right)^2 + \alpha^2 \left(\frac{dh}{dx}\right)^4\right] \tag{5.11}$$

$$\Delta F_g = \frac{1}{2} g\Delta\rho \int\int dxdy \; h^2. \tag{5.12}$$

Here we used $\int\int dxdy \; \alpha h_x = 0$ and $\int\int dxdy \; \alpha h_x^3 = 0$, since the interface is horizontal on average. It might seem that we take into account only one 4th order term and the others not. However, this term will become of the same size as the leading $(dh/dx)^2$ terms as soon as $\alpha^2 = (dh/dx)^{-2}$ while the others remain negligible.

When the function $h(x, y)$ is developed in a Fourier series $h(x, y) = \sum_q h_q \mathrm{e}^{i(q_x x + q_y y)}$, we can write the total work $\Delta F = \Delta F_c + \Delta F_g$ necessary to create (strained) perturbations on an interface as:

$$\begin{aligned} \Delta F = \frac{1}{2}\int\int dxdy \\ & \sigma \sum_{q_1,q_2} \vec{q}_1 \cdot \vec{q}_2 \; h_{q_1} h_{q_2} \; \mathrm{e}^{i(\vec{q}_1+\vec{q}_2)\cdot\vec{r}} + \\ + & \sigma \sum_{q_1,q_2,q_3,q_4} \alpha^2 q_{1x} q_{2x} q_{3x} q_{4x} h_{q_1} h_{q_2} h_{q_3} h_{q_4} \; \mathrm{e}^{i(\vec{q}_1+\vec{q}_2+\vec{q}_3+\vec{q}_4)\cdot\vec{r}} + \\ + & g\Delta\rho \sum_{q_1,q_2} h_{q_1} h_{q_2} \mathrm{e}^{i(\vec{q}_1+\vec{q}_2)\cdot\vec{r}}. \end{aligned} \tag{5.13}$$

By integrating over the area we find that only those terms for which $\vec{q}_1 = -\vec{q}_2$ give a contribution. This reduces the double sum in the first and second term in Eq. 5.13 to a single sum. For the last term it still leaves us with 3 summations. Apparently all modes are coupled. We can proceed by assuming that the coupling is weak, so that waves are uncorrelated. Thus when: averaged over the interface $\langle h_{q_1} h_{q_2} h_{q_3} h_{q_4}\rangle = \langle h_{q_1}\rangle\langle h_{q_2}\rangle\langle h_{q_3}\rangle\langle h_{q_4}\rangle = 0$. Decoupling will be a good approximation if the shear is small. The result will be that there are only contributions if $\vec{q}_1 = -\vec{q}_2 \wedge \vec{q}_3 = -\vec{q}_4$. There are three such combinations, so that:

$$\Delta F = \frac{1}{2}\sigma L^2 \sum_q q^2 |h_q|^2 + \frac{3}{2}\sigma L^2 \sum_{q,q'} \alpha^2 q_x^2 q_x'^2 |h_q|^2 |h_{q'}|^2 + \frac{1}{2} g\Delta\rho L^2 \sum_q |h_q|^2$$

$$\Delta F = \frac{1}{2}\sigma L^2 \sum_q q^2 |h_q|^2 \left(1 + \frac{3}{4}\sum_{q'} \alpha^2 q'^2 |h_{q'}|^2\right) + \frac{1}{2} g\Delta\rho L^2 \sum_q |h_q|^2, \tag{5.14}$$

where we use $\sum q_x^2 |h_q|^2 = \frac{1}{2} \sum q^2 |h_q|^2$.

In the zero shear situation ($\alpha = 0$), this gives the familiar expression

$$\Delta F = \frac{1}{2} L^2 \sum_q |h_q|^2 \left(\sigma q^2 + g \Delta \rho \right), \tag{5.15}$$

where the spectrum of h is found by applying the equipartition theorem:

$$\langle |h_q|^2 \rangle = \frac{k_B T}{L^2} \frac{1}{\sigma q^2 + g \Delta \rho}. \tag{5.16}$$

In the case of shear ($\alpha \neq 0$), it is, in spite of the approximations we already made, not very probable that the problem with a Hamiltonian as in Eq. 5.14 can be solved. However, if we consider the factor in between brackets as a perturbation, then the h_q can be approximated by their equilibrium (non-sheared) values. This factor can be included into an effective surface tension:

$$\Delta F = \frac{1}{2} L^2 \sum_q |h_q|^2 \left(\sigma_{\text{eff}} q^2 + g \Delta \rho \right), \tag{5.17}$$

with

$$\sigma_{\text{eff}} = \sigma \left(1 + \frac{3}{4} \sum_q \alpha^2 q^2 |h_q|^2 \right). \tag{5.18}$$

It is clear that $\sigma_{\text{eff}} > \sigma$, as it is found experimentally. Again we can apply equipartition to find:

$$\langle |h_q|^2 \rangle = \frac{k_B T}{L^2} \frac{1}{\sigma_{\text{eff}} q^2 + g \Delta \rho}. \tag{5.19}$$

This will also lead to a correlation function of similar form as for the non sheared case, and the in plane correlation length will follow the change in surface tension as $\xi = \sqrt{\sigma_{\text{eff}}/g\Delta\rho}$.

Strain and relaxation of waves

To calculate σ_{eff} we have to find out to what extent the waves are actually stretched, i.e. what is the strain α? It is clear that it should depend on the life time τ of the modes in some way.

To find α we consider the work that is performed on the interface by the shear. From Eq. 5.14 this work is:

$$\Delta F_{\text{shear}} = \frac{3}{8} \sigma L^2 \alpha^2 \left(\sum_q q^2 |h_q|^2 \right)^2 \equiv \frac{1}{2} G \alpha^2. \tag{5.20}$$

We may look at this as an elastic energy, with a rather complicated "spring" constant G. But it is a "lossy spring": the added energy is dissipated continuously by the decay of wave amplitudes h_q. In a steady state the dissipation rate must equal the rate with which shear supplies the energy:

$$\frac{d\Delta F_{\text{shear}}}{dt} = \frac{1}{2}G\frac{d\alpha^2}{dt} + \frac{1}{2}\alpha^2\frac{dG}{dt} = 0. \tag{5.21}$$

Here the first term is the energy that is gained in shear flow and the second term the dissipation. The first term can be calculated in a straightforward way:

$$\left(\frac{d\Delta F_{\text{shear}}}{dt}\right)_{\text{supplied}} = \frac{1}{2}G\frac{d\alpha^2}{dt} = G\alpha\frac{d\alpha}{dt} = G\alpha\dot{\gamma}. \tag{5.22}$$

To find the dissipation rate we have to differentiate $G = \frac{3}{4}\sigma L^2\left(\sum_q q^2|h_q|^2\right)^2$ with respect to time. This can be done by using $h_q = h_{q0}\mathrm{e}^{-t/2\tau_q}$, thus:

$$\begin{aligned}
\left(\frac{d\Delta F_{\text{shear}}}{dt}\right)_{\text{dissipated}} &= \frac{1}{2}\alpha^2\frac{dG}{dt} \\
&= \frac{3}{8}\sigma L^2\alpha^2 2\left(\sum_q q^2|h_q|^2\right)\frac{d}{dt}\left(\sum_q q^2|h_q|^2\right) \\
&= \alpha^2 G\frac{\frac{d}{dt}\sum_q q^2|h_q|^2}{\sum_q q^2|h_q|^2} \\
&= -\alpha^2 G\frac{\sum_q \frac{1}{\tau_q}q^2|h_q|^2}{\sum_q q^2|h_q|^2} \\
&= -\alpha^2 G\left\langle\frac{1}{\tau_q}\right\rangle.
\end{aligned} \tag{5.23}$$

The average strain is found by combining those results (Eqs. 5.21, 5.22 and 5.23):

$$\alpha = \dot{\gamma}\left\langle\frac{1}{\tau_q}\right\rangle^{-1}. \tag{5.24}$$

Thus, the strain is simply the ratio of the shear rate and the average decay rate of capillary waves. Finally, we can work out those sums using Eq. 5.3 for τ_q:

$$\begin{aligned}
\sum_q \frac{1}{\tau_q}q^2|h_q|^2 &= \frac{L_{\text{cap}}}{2\tau_{\text{cap}}}\frac{k_BT}{\sigma L^2}\sum_q\frac{q^2+L_{\text{cap}}^{-2}}{q}q^2\frac{1}{q^2+L_{\text{cap}}^{-2}} \\
&= \frac{L_{\text{cap}}}{2\tau_{\text{cap}}}\frac{k_BT}{\sigma L^2}\left(\frac{L}{2\pi}\right)^2 2\pi\int_q dq\; q^2 \\
&= \frac{k_BT}{12\pi\sigma}\frac{L_{\text{cap}}}{\tau_{\text{cap}}}q_{\text{max}}^3,
\end{aligned} \tag{5.25}$$

and

$$
\begin{aligned}
\sum_q q^2 |h_q|^2 &= \frac{k_B T}{\sigma L^2} \sum_q q^2 \frac{1}{q^2 + L_{\text{cap}}^{-2}} \\
&= \frac{k_B T}{\sigma L^2} \left(\frac{L}{2\pi}\right)^2 \pi \int_{q^2} dq^2 \frac{q^2}{q^2 + L_{\text{cap}}^{-2}} \\
&= \frac{k_B T}{4\pi\sigma} \int_{q^2} dq^2 \left(1 - \frac{L_{\text{cap}}^{-2}}{q^2 + L_{\text{cap}}^{-2}}\right) \\
&= \frac{k_B T}{4\pi\sigma} \left(q_{\max}^2 - L_{\text{cap}}^{-2} \ln(1 + q_{\max}^2 L_{\text{cap}}^2)\right) . \qquad (5.26)
\end{aligned}
$$

The logarithmic term is for state point A only 5% and for state point B much less. This means we can safely ignore this term and we end up with:

$$
\sigma_{\text{eff}} = \sigma \left(1 + \frac{9}{4} \frac{3}{4\pi} \dot{\gamma}^2 \frac{k_B T}{\sigma} \frac{\tau_{\text{cap}}^2}{L_{\text{cap}}^2}\right) . \qquad (5.27)
$$

Note that this expression is identical to Eq. 5.5 (for $\dot{\gamma} > \dot{\gamma}_{\text{crit}}$) apart from the numerical factor 9/4.

6

Phase Separating Systems of Shear-aligned Rod-like Viruses

ABSTRACT

We investigate the kinetics of phase separation for a mixture of rod-like viruses (*fd*) and polymer (dextran), which effectively constitutes a system of attractive rods. This dispersion is quenched from a flow-induced fully nematic state into the region where the nematic and the isotropic phase coexist. We show experimental evidence that the kinetic pathway depends on the overall concentration. When the quench is made at high concentrations, the system is meta-stable and we observe typical nucleation-and-growth. For quenches at low concentration the system is unstable and the system undergoes a spinodal decomposition. At intermediate concentrations we see the transition between both demixing processes, where we locate the spinodal point.

6.1. INTRODUCTION

Systems that are quenched into a state where at least one order parameter is unstable undergo spinodal phase separation. Here, the initially homogeneous system is unstable against fluctuations of arbitrary small amplitude, and phase separation sets in immediately after a quench. In the initial stage of phase separation an interconnected "labyrinth structure" of regions with somewhat higher and lower values of the order parameter is observed. For quenches where the system becomes meta-stable, phase separation is initiated by fluctuations with a sufficiently large amplitude. Since such fluctuations have a small probability to occur, phase separation sets in after a certain delay time, referred to as the induction time. Here, nuclei are formed throughout the volume which grow when they are sufficiently large. The two different mechanisms of phase separation (spinodal decomposition and nucleation-and-growth) can thus be distinguished during the initial stages of phase separation from (i) the difference in morphology (interconnected structures versus growth of isolated nuclei) and (ii) the delay time before phase separation sets in (no delay time for spinodal decomposition and a finite induction time for nucleation-and-growth).

As Onsager showed in 1949 [14], when the particles are not spherical in shape, i.e. disk-like or elongated particles, the system can become unstable or meta-stable with respect to fluctuations in *orientation.* These orientational fluctuations drive concentrations differences, resulting in a phase with high concentration and orientational order, the *nematic* phase, and a phase with low concentration and no orientational order, the *isotropic* phase. For very long and thin rods with short-ranged repulsive interactions, the binodal concentrations, i.e. the concentrations of the isotropic and nematic phases in equilibrium after phase separation is completed, have been determined using different approximations in minimizing Onsager's functional for the free energy (see Ref. [116] and references therein), while for shorter rods computer simulations have been performed to obtain binodal concentrations [117,118]. Also the spinodal concentration where the isotropic phase becomes unstable has been found [14,119].

Binodal points are relatively easy to determine experimentally, since they are given by the concentrations of the bottom and top phase after phase separation. In contrast, it is not at all straightforward to obtain spinodal points, since one would ideally like to perform a concentration quench from low or high concentration into the two-phase region, where the initial state is isotropic or nematic, respectively. In a recent paper such a kind of 'quench' was performed by inducing polymerization of short actin chains [120], and tactoids and spinodal structures were observed.

Signatures of spinodal decomposition have also been obtained for boehmite rods, by homogenizing a phase separated system and sequential polarization microscopy and small angle light scattering measurements [121]. Alternatively, external fields like shear flow [122] and a magnetic field [123, 124] can be applied to prevent a system from phase separation and to stabilize the nematic phase. After cessation of such an external field the nematic phase will become unstable or meta-stable, depending on the constitution of the sample, and phase separation sets in. In this paper we induce a fully nematic phase with a well defined director by imposing shear flow to a dispersion of colloidal rods. We use *fd*-viruses as system, since the equilibrium phase behavior concerning the binodal points, has been well understood on the basis of Onsager theory [125, 126]. Polymer is added to the dispersion in order to widen the region of isotropic-nematic phase coexistence, which facilitates the phase separation experiments [127]. We perform quenches of a flow aligned initial state to zero shear, which renders the system unstable or meta-stable to fluctuations in the orientation, depending on the concentration of rods. As a consequence phase separation sets in, which we observe by confocal scanning laser microscopy (CSLM). We perform this experiment for different concentrations, throughout the region of phase coexistence. Our results illustrate the difference between nucleation-and-growth and spinodal decomposition in the case of demixing elongated particles, and result in the determination of the nematic-isotropic spinodal point.

6.2. ON THE INSTABILITY OF INITIAL STATES

A convenient way to analyze the stability of a homogeneous initial state is by introducing an order parameter P_2, which measures the degree of alignment [81]. For the isotropic state $P_2 = 0$, while for a perfectly aligned state $P_2 = 1$. Subsequently, a stability analysis of stationary solutions of the equation of motion is made on the basis of a bifurcation diagram [119], where the order parameter P_2 for stationary solutions is plotted against the concentration. A schematic bifurcation diagram is given in Fig. 6.1. The two solid lines represent stable stationary solutions of the equation of motion, while the dotted lines represent unstable stationary solutions. The isotropic state ceases to be stable above the concentration indicated as C_i^{spin}, while the nematic state becomes unstable at concentrations lower than C_n^{spin}. Above C_i^{spin}, the isotropic state is still a stationary solution , but is now unstable. Below C_n^{spin}, on the contrary, there is no unstable nematic state that is a stationary solution of the equation of motion. The two spinodal concentrations C_i^{spin} and C_n^{spin} are connected by a so-called separatrix (indicated by the dotted line) which separates the basins of attraction for the isotropic and nematic

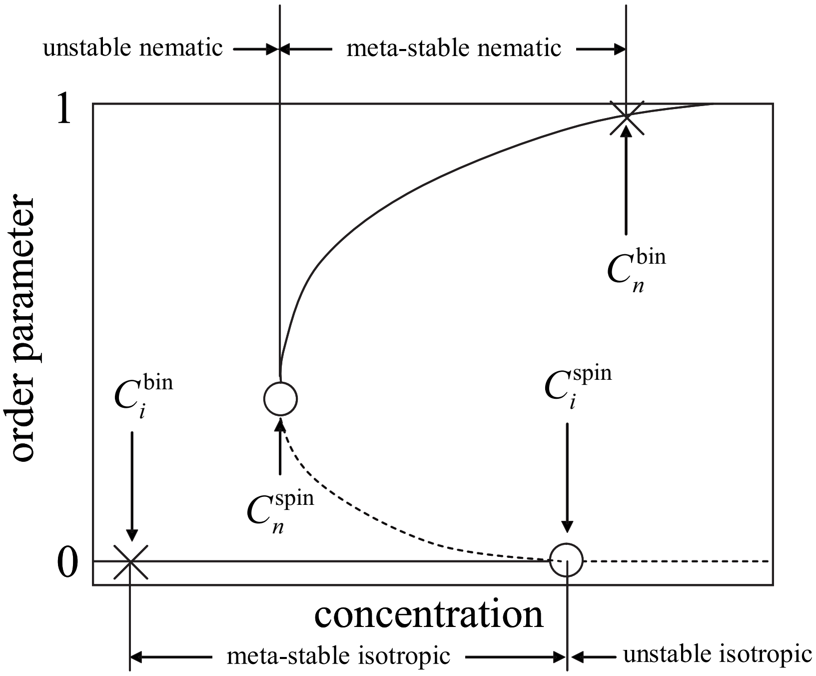

FIGURE 6.1. The bifurcation diagram, where the orientational order parameter P_2 is plotted against concentration. Indicated are the various meta- or unstable regions for the two different initial states of the homogeneous suspension. The points marked by X and O are spinodal and binodal points, respectively.

state. A homogeneous initial state above this separatrix develops a higher degree of alignment, while an initial state below the separatrix becomes more isotropic.

Note that the bifurcation diagram relates to homogeneous systems. In an experiment, starting from a homogeneous state, inhomogeneities develop simultaneously with a change of the order parameter of the otherwise homogeneous system. In equilibrium, after completion of phase separation, there is an isotropic phase with concentration C_i^{bin} in coexistence with a nematic phase with concentration C_n^{bin}. One can either start from a stationary state, or from a non-stationary state, like a nematic state with a concentration lower than C_n.

In this paper we prepare an initial nematic state by shearing a suspension at large enough shear rate such that the induced nematic phase is stable against phase separation (see Ref. [128] for a discussion of the bifurcation diagram for sheared systems), and then quench to zero shear rate. For this initial state it is expected

Table 6.1. Overview of the used samples.

Code	φ^5_{nem}	φ^4_{nem}	φ^3_{nem}	φ^2_{nem}	φ^1_{nem}
fd (mg/mL)	29.5	28.1	25.8	23.6	19.3
φ_{nem}	0.96	0.85	0.68	0.52	0.18

that spinodal decomposition occurs at lower concentrations, while nucleation and growth is observed at higher concentrations. For an isotropic initial state this would be reversed: spinodal decomposition at high concentrations and nucleation and growth at lower concentrations. The observed phase separation kinetics thus depends crucially on the preparation of the initial state of the suspension.

6.3. Materials and methods

As model colloidal rods we use *fd*-virus particles which were grown as described elsewhere [127]. A homogeneous solution of 22.0 mg/mL *fd*-virus and 12.1 mg/mL of Dextran (507 kd, Sigma-Aldrich) in 20 mM tris buffer at pH 8.15 with 100 mM NaCl is allowed to macroscopically phase separate. This concentration of *fd*-virus is exactly in the biphasic region, which is very small when no polymer is added, namely between 21 and 23 mg/mL. Due to the added polymer, the binodal points shift to 17 and 30 mg/mL, respectively. New dispersions are prepared by mixing a known volume of the coexisting isotropic and nematic bulk phases. The relative volume of nematic phase in this new dispersion is denoted as φ_{nem}.

For the microscopic observations we used a home-built counter rotating cone-plate shear cell, placed on top of a Leica TCS-SP2 inverted confocal microscope. This cell has a plane of zero velocity in which objects remain stationary with respect to the microscope while shearing. For details of the setup we refer to Chapter 2. For the measurements described here we used confocal reflection mode at a wavelength of 488 nm. Quench experiments were done as follows. Samples were first sheared at a high rate of 10 s^{-1} for several minutes. The shear was then suddenly stopped, after which images were recorded at regular time intervals. These images were parallel to the flow-vorticity plane. The table gives an overview of the concentrations where quench experiments have been performed.

6.4. Results

In the left column of Fig. 6.2 we show micrographs of the initial stage of phase separation for five different concentrations taken after a shear rate quench from

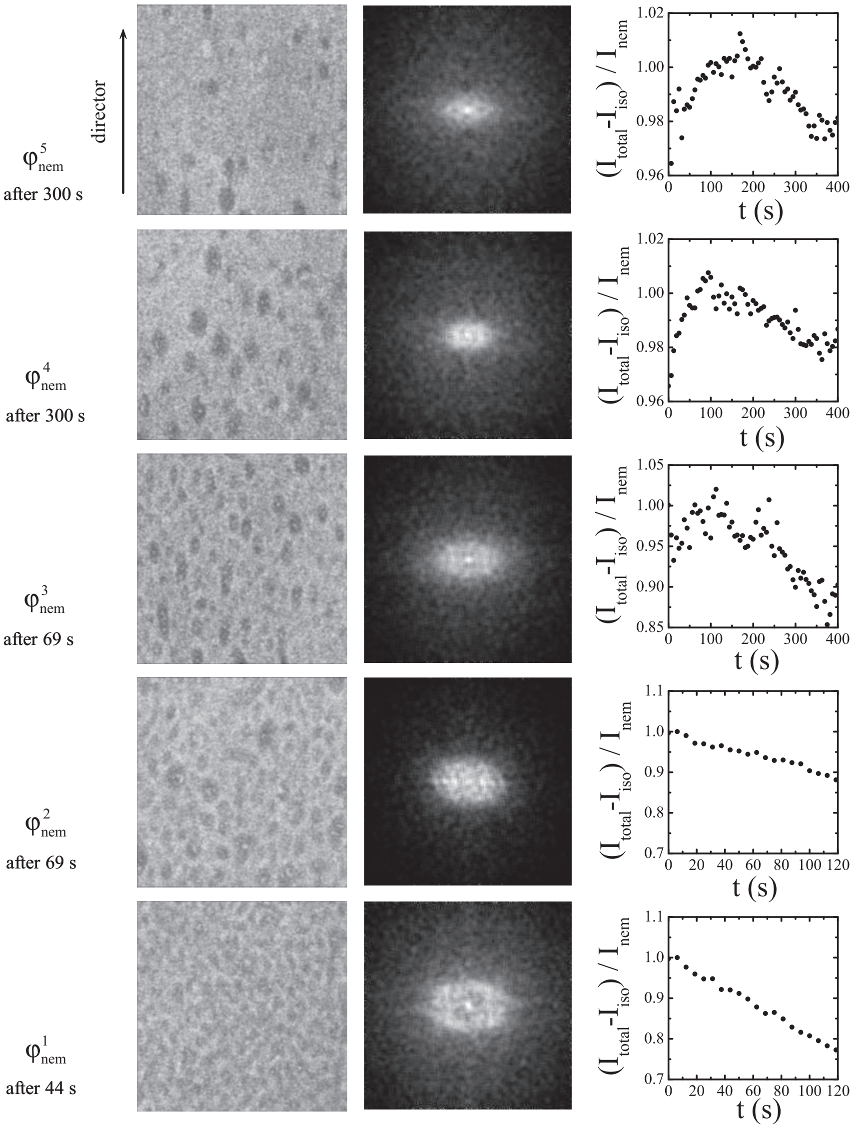

FIGURE 6.2. The initial stages of phase separation for five different concentrations after a quench from a flow aligned nematic phase to zero shear. The left column shows the micrographs taken by reflection confocal scanning laser microscopy (field of view = 110 μm); the middle column shows the fourier transform of the micrographs; the right column plots the mean intensity of the micrographs minus the mean intensity for the isotropic phase, normalized by the initial intensity of the nematic phase.

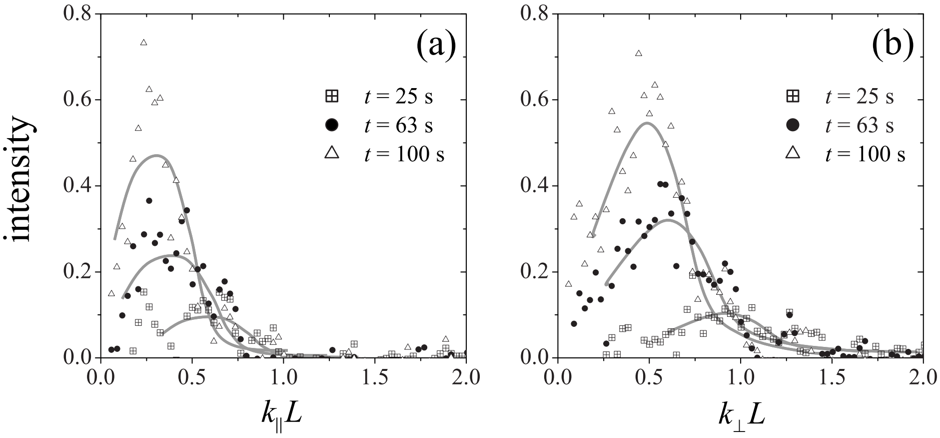

FIGURE 6.3. The cross section of the Fourier transform parallel (a) and perpendicular (b) to the director for φ^1_{nem} (lines to guide the eye). The length is scaled by the rod length L.

a high shear rate, where the nematic state is stable for each concentration, to zero shear. These images show the flow (vertical) - vorticity (horizontal) plane at a given time after the quench. Thus the director of the initial nematic phase lies in the vertical direction. Fourier transforms of the images are plotted in the second column of Fig. 6.2. The background is corrected for by subtracting the Fourier transform of the first frame. The right column plots the development of the total intensity of the images minus the intensity in the isotropic phase, as determined from an isolated isotropic region, normalized by the initial nematic intensity. Qualitatively the difference between the concentrations is obvious. In the first two images, i.e. the two highest concentrations, isolated dark ellipsoidal structures can be seen on a bright back ground. These are droplets of the isotropic phase referred to as tactoids. The number of tactoids increases when the concentration is decreased (b and c) until the structures become interconnected (d and e). This also follows from the Fourier transform of the pictures where a ring is detected for the lowest concentration and a constant increasing intensity towards $\vec{k} = 0$ for the highest concentration. The time scale at which the inhomogeneities are formed also changes. As can be seen in the third column of Fig. 6.2, the high concentrations all show an induction time before the phase separation sets in, while for the low concentrations phase separation sets in immediately. Note also the times at which the images in Fig. 6.2 were taken. The isolated nuclei and

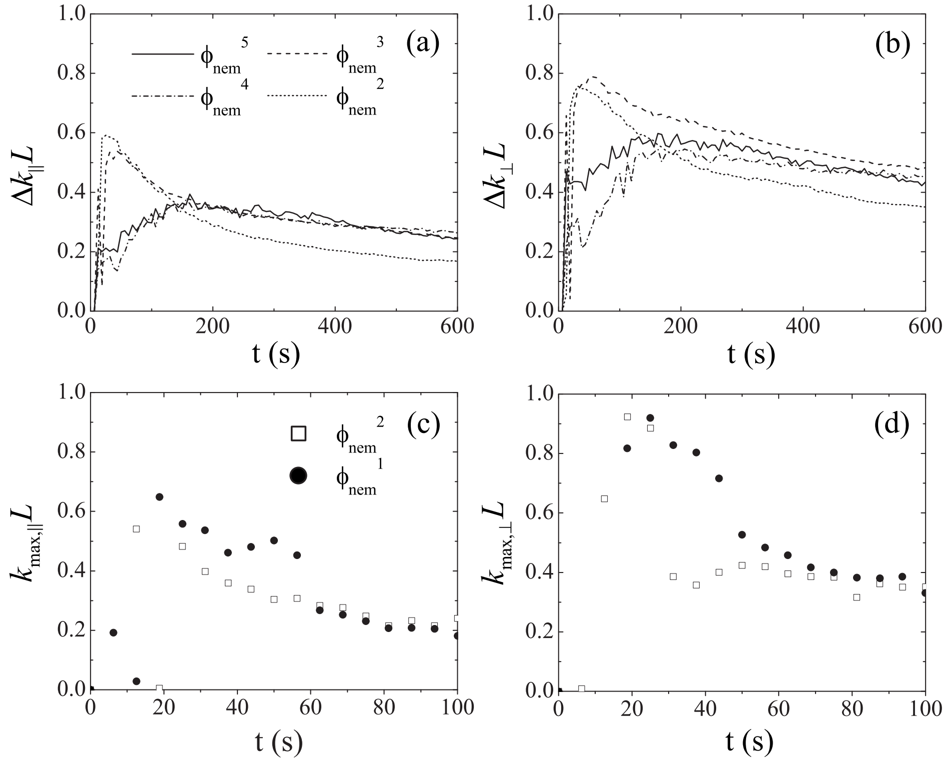

FIGURE 6.4. Width of the 2-D gaussian fit, ΔkL , of the Fourier transform parallel (a) and perpendicular (b) to the director for the higher concentrations for the higher concentrations. Wavevector $k_{\max}L$ where the intensity is maximum for the cross sections parallel (c) and perpendicular (b) to the director for the lower concentrations.

the induction time are typical for nucleation-and-growth, while the interconnected structures and immediate phase separation are typical for spinodal decomposition.

We use the Fourier transform of the images as shown in Fig. 6.2 to quantify the phase separation processes. The interesting quantity for nucleation-and-growth is the width of the Fourier transform, Δk, which is a measure for the anisotropic form factor of the nuclei. Alternatively one could determine the average size of the features in real space, but due to the low contrast this is difficult. For spinodal decomposition the interesting quantity is the wave vector at which the fourier transform reaches its maximum, $k_{\max}$, quantifying the fastest growing concentration fluctuation. In both cases the fit of the Fourier transform should be performed in two dimensions, since the initial state is anisotropic. Therefore we took cross

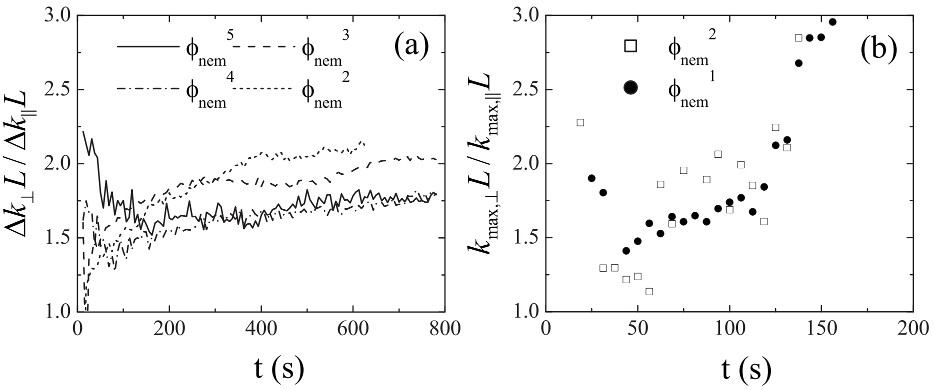

FIGURE 6.5. (a) The ratio $\Delta k_\perp L/\Delta k_\| L$ for the higher concentrations and (b) the ratio $k_{\max,\perp} L/k_{\max,\|} L$ for the lower concentrations.

sections parallel and perpendicular to the director in the Fourier domain, i.e. the vertical and horizontal in Fig. 6.2 middle row, to determine $k_{\max}$. Typical cross sections are shown in Fig. 6.3, where the wave vector k is scaled by the rod length L. To determine Δk, we performed a 2-D gaussian fit around the origin of the Fourier transforms. Results of a 2-D gaussian fit of the Fourier transform around the origin are shown for the higher concentrations in Fig. 6.4a and b, plotting the width in the direction of the director and perpendicular to the director, respectively. $k_{\max}$ as found from fits of the cross sections parallel and perpendicular to the director are given in Fig. 6.4 c and d, respectively. Both fit procedures result in an anisotropic morphology as can be seen in Fig. 6.5, where we plotted $\Delta k_\perp L/\Delta k_\| L$ and $k_{\max,\perp} L/k_{\max,\|} L$.

The late stages of the different phase separation processes also show some interesting phenomenology, as can be seen in Fig. 6.6 and Fig. 6.7. For spinodal decomposition (Fig. 6.6) we observe first a growing of the interconnected structures, which then break down into tactoids. Later on tactoids coalesce, and they become more spherical with increasing size. Note that these tactoids contain the nematic phase and not the isotropic phase, as observed for the nucleation-and-growth process at higher concentrations. In the late stage of nucleation-and-growth, i.e. at high concentrations, we see that coalescence of tactoids containing the isotropic phase as shown in Fig. 6.7 is favorable when two tactoids meet somewhat from the middle. In this case the rod orientation near both features is similar and the barrier which has to be overcome for coalescence is low.

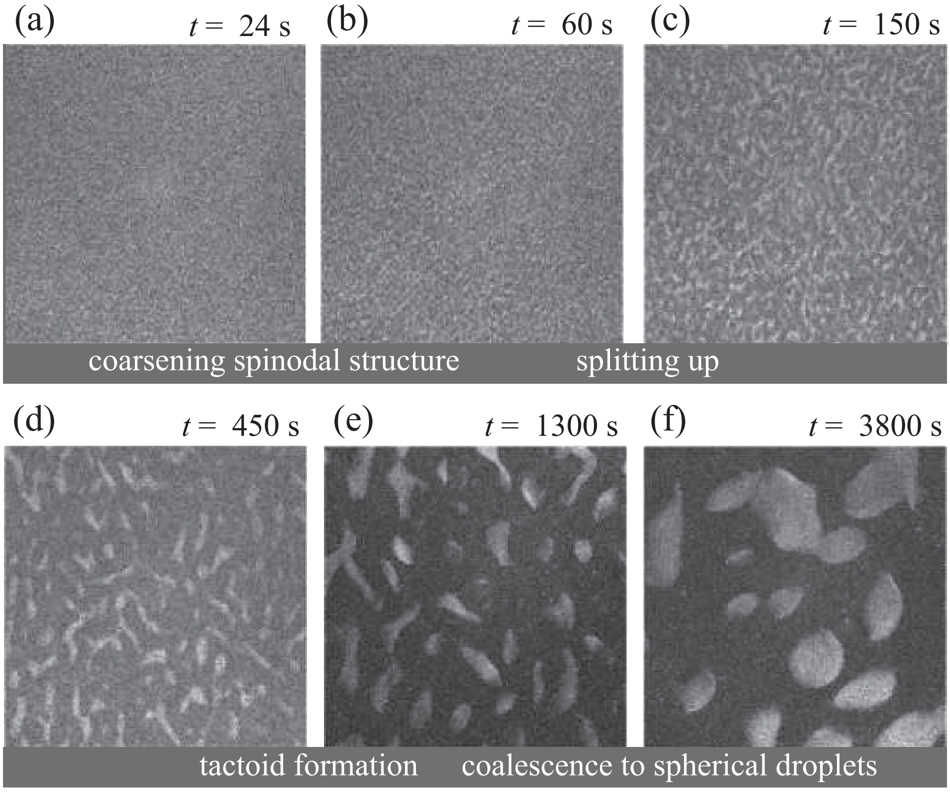

FIGURE 6.6. The late stages for spinodal decomposition (φ^1_{nem}, field of view = 375 μm) involve coarsening, splitting up of the spinodal structure, and finally tactoid formation and coalescence to spherical drops.

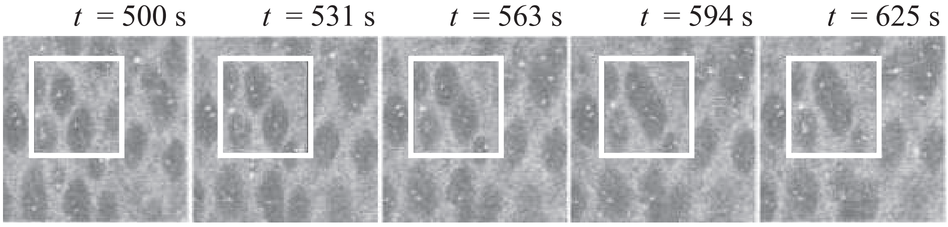

FIGURE 6.7. The late stages of nucleation and growth are characterized by the coalescence of tactoids (φ^5_{nem}, field of view = 73 μm).

6.5. DISCUSSION

On the basis of these observations we can now locate the metastable region, i.e. where the system has to overcome a free energy barrier, and the unstable region, where there is no such barrier. At the high concentrations (φ^5_{nem}, φ^4_{nem}) the system is meta-stable, which is reflected by the observed isolated structures formed (top row in Fig. 6.2) and the induction time (bottom row in Fig. 6.2). With decreasing concentration the system approaches the unstable region: the number of nuclei increases while the induction time decreases and finally vanishes. The lowest concentration φ^1_{nem} is clearly unstable after cessation of the flow. It shows all the features typical for spinodal decomposition: phase separation immediately sets in throughout the whole sample, with a typical length scale which is characterized by the scattering ring observed in the Fourier transform. It can be shown, in fact, that the observed phase separation process for the lowest concentration has features typical for the spinodal decomposition of rods, as derived recently from a microscopic theory by one of the authors [81]. This will be the subject of a following paper [129].

In the intermediate region it is difficult to judge from the morphology if nucleation-and-growth takes place or spinodal decomposition, since it is difficult to distinguish between a high number of tactoids and an interconnected structure. However, φ^3_{nem} shows a short induction time after the quench after which clearly separated tactoids are formed, while for φ^2_{nem} phase separation immediately sets in showing ellipsoidal structures which clearly 'influence' each other. Moreover, Fig. 6.4 shows that the size of the structures formed in φ^3_{nem} coincides after some time with the clearly nucleated structures of φ^4_{nem} and φ^5_{nem}, while the size of the structures formed in φ^2_{nem} coincides with samples which clearly show spinodal decomposition. Thus, we locate the transition from meta-stable to unstable, i.e. the spinodal point, between at 23.5 mg/mL and 25.8 mg/mL. This is the first experimental observation of the spinodal point in a rod-like system. We should mention at this point that in fact our sample consists of a mixture of rods and polymer. Addition of the polymer causes a widening of the biphasic region [127], i.e. a shift of the binodal points. It is now interesting to see that the high concentration binodal shifts as much as from 23 mg/mL to 30 mg/mL. In contrast, the high concentration binodal point, C_n^{bin}, shifts from a concentration between 21 mg/mL and 23 mg/mL to somewhere between 23.5 mg/mL and 25.8 mg/mL. This leads to the interesting conclusion that the shift of the high concentration binodal point, C_n^{bin}, due to the attraction between the rods, is considerable compared to the shift of the high concentration spinodal point, C_n^{spin}. In other words, making the rods attractive causes a widening of the meta-stable region, while the unstable region remains unaffected. Addition of more polymer will result in more complex kinetics as described in reference [130].

Interestingly, for all concentrations we observe that the morphology of the phase separating system is anisotropic. This is most clear for the highest concentrations, where the tactoids all point upwards, i.e. in the direction of the director of the surrounding nematic phase. Also the Fourier transforms for the lower concentrations show deformed intensity rings in fourier space (most right FFT image in Fig. 6.2). Moreover, also the kinetics of the phase separation is fastest in the direction of the nematic director. This follows for instance from the ratio of $k_{\max\perp}/k_{\max\|}$ as plotted in 6.5b, which increases in time. In other words, for all concentrations phase separation is anisotropic, due to residual alignment after the quench of the initially strongly sheared suspension, and not isotropic as is the case for spheres [88].

The length of the first observed tactoids just below C_n^{bin} is about 12 times the rod length, while just above C_n^{spin} it is seven times the rod length. The thickness is about two third of the length in both cases. Typical length scales for the initial spinodal morphology are not more than six rod lengths. These sizes seem to be quite small, considering also the random orientation of the rods in the isotropic phase, but it is in accordance with a the microscopic theory for spinodal decomposition of rods [81]. It does suggest that we really image the initial stage. The breaking up of the spinodal structure into nematic tactoids and the sequential growth in the late stage of spinodal decomposition seems surprising since for dispersions of spheres only coalescence and macroscopic phase separation would be observed. However, a similar order of events has been observed for polymer mixtures with thermotropic liquid crystals [131]. Simulations on such mixtures show that the break down is due to the effect of the flow-alignment coupling, and not primarily due to elastic effects [132]. An explanation in the same line was given by Fukuda in a numerical treatment of time-dependent Ginzburg-Landau equations of liquid crystalline polymers [133]. The volume dependence of the morphology in the final stage can be explained by the competition between the interfacial tension and nematic elasticity of the tactoids [134].

6.6. Conclusion

We studied the kinetics of the nematic-isotropic phase transition of a dispersion of *fd*-virus particles with added polymer after shear quenches into the two-phase region. By varying the equilibrium rod concentration φ_{nem} we were able to detect a nucleation-and-growth mechanism for high φ_{nem}, spinodal decomposition for low φ_{nem}, and the transition between the two processes. In this way we were able to trace for the first time the nematic-isotropic spinodal point C_n^{spin}. Thus, we found that addition of polymer widens the meta-stable region greatly. Furthermore, we showed that the phase separation is strongly influenced by the director of the initial nematic state. The nematic phase also influences the late stages of spinodal decomposition, causing a splitting up of the interconnected structures.

ACKNOWLEDGEMENTS

We gratefully thank Pavlik Lettinga, Kyongok Kang and Jan Dhont (Forschungszentrum Jülich), with whom this work was performed.

Bibliography

[1] R. Brown. *Phil. Mag.*, 4:161, 1828.

[2] A. Einstein. *Ann. Phys. (4th Series)*, 17:549, 1905.

[3] R. J. Hunter. *Foundations of Colloid Science Vol. I.* Oxford University Press, Oxford, 1986.

[4] M. E. Leunissen, C. G. Christova, A.-P. Hynninen, C. P. Royall, A. I. Campbell, A. Imhof, M. Dijkstra, R. van Roij, and A. van Blaaderen. *Nature*, 437:235, 2005.

[5] N. F. Carnahan and K. E. Starling. *J. Chem. Phys.*, 51:635, 1969.

[6] B. J. Alder, W. G. Hoover, and D. A. Young. *J. Chem. Phys.*, 49:3688, 1968.

[7] W. W. Wood and J. D. Jacobsen. *J. Chem. Phys.*, 27:1207, 1957.

[8] B. J. Alder and T. E. Wainwright. *J. Chem. Phys.*, 27:1208, 1957.

[9] W. G. Hoover and F. H. Ree. *J. Chem. Phys.*, 49:3609, 1968.

[10] P. N. Pusey and W. van Megen. *Nature*, 320:340, 1986.

[11] B. J. Ackerson. *Journal of Rheology*, 34 (4):553, 1990.

[12] S. Asakura and F. Oosawa. *J. Chem. Phys.*, 22:1255, 1954.

[13] A. Vrij. *Pure Appl. Chem.*, 48:471, 1976.

[14] L. Onsager. *Annals of the New York Academy of Science*, 51:62, 1949.

[15] Z. Dogic and S. Fraden. In G. Gompper and M. Schick, editors, *Soft Matter Vol. 2: Complex Colloidal Suspensions*, chapter 1. Wiley-VCH, Weinheim, 2006.

[16] W. Stöber, A. Fink, and E. Bohn. *Journal of Colloid and Interface Science*, 26:62, 1968.

[17] L. Antl, J. W. Goodwin, R. D. Hill, R. H. Ottewill, S. M. Owens, S. Papworth, and J. A. Waters. *Colloids and Surfaces*, 17:67, 1986.

[18] G. Bosma, C. Pathmamanoharan, E. H. A. de Hoog, W. K. Kegel, A. van Blaaderen, and H. N. W. Lekkerkerker. *Journal of Colloid and Interface Science*, 245:292, 2002.

[19] R. P. A. Dullens, M. Claesson, D. Derks, A. van Blaaderen, and W. K. Kegel. *Langmuir*, 19(15):5963, 2003.

[20] M. Minsky. *U.S. Patent*, 301467, 1961.

[21] M. Minsky. *Scanning*, 10:128, 1988.

[22] R. M. Amos, J. G. Rarity, P. R. Tapster, T. J. Shepherd, and S. C. Kitson. *Phys. Rev. E*, 61(3):2929, 2000.

[23] M. Moseler and U. Landman. *Science*, 289:1165, 2000.

[24] P. Butler. *Current Opinion in Colloid and Interface Science*, 4(3):214, 1999.

[25] I. W. Hamley. *Current Opinion in Colloid and Interface Science*, 5(5-6):342, 2000.

[26] W. Richtering. *Current Opinion in Colloid and Interface Science*, 6(5-6):446, 2001.

[27] A. van Blaaderen. *MRS Bulletin*, 29(2):85, 2004.

[28] A. van Blaaderen. *Progress in Colloid and Polymer Science*, 104:59, 1997.

[29] W. K. Kegel and A. van Blaaderen. *Science*, 287(5451):290, 2000.

[30] U. Gasser, E. R. Weeks, A. Schofield, P. N. Pusey, and D. A. Weitz. *Science*, 292(5515):258, 2001.

[31] P. N. Pusey, W. van Megen, P. Bartlett, B. J. Ackerson, J. G. Rarity, and S. M. Underwood. *Phys. Rev. Lett.*, 63(25):2753, 1989.

[32] B. J. Ackerson and N. A. Clark. *Phys. Rev. Lett.*, 46(2):123, 1981.

[33] A. Imhof, A. van Blaaderen, and J. K. G. Dhont. *Langmuir*, 10(10):3477, 1994.

[34] T. Palberg and R. Biehl. *Faraday Discussions*, 123:133, 2003.

[35] J. K. G. Dhont, M. P. Lettinga, Z. Dogic, T. A. J. Lenstra, H. Wang, S. Rathgeber, P. Carletto, L. Willner, H. Frielinghaus, and P. Lindner. *Faraday Discussions*, 123:157, 2003.

[36] T. Sawada, Y. Suzuki, A. Toyotama, and N. Iyi. *Jpn. J. Appl. Phys.*, 40:L1226, 2001.

[37] V. A. Tolpekin, M. H. G. Duits, D. van den Ende, and J. Mellema. *Langmuir*, 20:2614, 2004.

[38] P. Varadan and M. J. Solomon. *J. Rheol.*, 47:943, 2003.

[39] H. Hoekstra, J. Vermant, and J. Mewis. *Langmuir*, 19:9134, 2003.

[40] T. Tanaami, S. Otsuki, N. Tomosada, Y. Kosugi, M. Shimizu, and H. Ishida. *Appl. Opt.*, 41:4704, 2002.

[41] G. I. Taylor. *Proc. Roy. Soc. London*, 29:501, 1934.

[42] N. Grizzuti and O. Bifulco. *Rheologica Acta*, 36(4):406, 1997.

[43] V. Breedveld, D. van den Ende, M. Bosscher, R. J. J. Jongschaap, and J. Mellema. *Phys. Rev. E*, 63:21403, 2001.

[44] M. A. Paques, A. Imhof, A. van Blaaderen, and Y. Nicolas. *European Patent Application*, 1312910, 2001.

[45] Y. Nicolas, M. Paques, D. van den Ende, J. K. G. Dhont, R. C. van Polanen, A. Knaebel, A. Steyer, J. P. Munch, T. B. J. Blijdenstein, and G. A. van Aken. *Food Hydrocolloids*, 17(6):907, 2003.

[46] J. C. Crocker and D.G. Grier. *Journal of Colloid Interface Science*, 179:298, 1996.

[47] Y. Nicolas, M. Paques, A. Knaebel, A. Steyer, J. P. Munch, T. B. J. Blijdenstein, and G. A. van Aken. *Review of Scientific Instruments*, 74(8):3838, 2003.

[48] A. Yethiraj and A. van Blaaderen. *Nature*, 421(6922):513, 2003.

[49] C. P. Royall, M. E. Leunissen, and A. van Blaaderen. *Journal of Physics: Condensed Matter*, 15 (48):S3581, 2003.

[50] F. A. Lindemann. *Physik. Zeitschr.*, 11(14):610, 1910.

[51] M. J. Stevens and M. O. Robbins. *Phys. Rev. E*, 48(5):3778, 1993.

[52] H. Löwen, T. Palberg, and R. Simon. *Phys. Rev. Lett.*, 70 (10):1557, 1993.

[53] J. Bongers and H. Versmold. *J. Chem. Phys.*, 104 (4):1519, 1996.

[54] A. Brands, H. Versmold, and W. van Megen. *J. Chem. Phys.*, 110 (2):1283, 1999.

[55] H. M. Lindsay and P. M. Chaikin. *J. Phys. (Paris) Colloque*, 46-C3:269, 1985.

[56] K. Zahn and G. Maret. *Phys. Rev. Lett.*, 85(17):3656, 2000.

[57] E. Cappelaere, J. F. Berret, J. P. Decruppe, R. Cressely, and P. Lindner. *Phys. Rev. E*, 56 (2):1869, 1997.

[58] P. Boltenhagen, Y. Hu, E. F. Matthys, and D. J. Pine. *Phys. Rev. Lett.*, 79 (12):2359, 1997.

[59] T. Palberg and M. Wurth. *J. Phys. I (France)*, 6:237, 1996.

[60] J. Vermant, L. Raynaud, J. Mewis, B. Ernst, and G. G. Fuller. *Journal of Colloid and Interface Science*, 211:221, 1999.

[61] B. J. Ackerson and P. N. Pusey. *Phys. Rev. Lett.*, 61:1033, 1988.

[62] Y. D. Yan and J. K. G. Dhont. *Physica A*, 198:78, 1993.

[63] S. E. Paulin, B. J. Ackerson, and M. S. Wolfe. *Phys. Rev. E*, 55:5812, 1997.

[64] J. Bender and N. J. Wagner. *J. Rheol.*, 40:899, 1996.

[65] I. Cohen, T. G. Mason, and D. A. Weitz. *Phys. Rev. Lett.*, 93 (4):046001, 2004.

[66] P. Schall, I. Cohen, D. A. Weitz, and F. Spaepen. *Nature*, 440:319, 2006.

[67] R. G. Larson. *The Structure and Rheology of Complex Fluids*. Oxford University Press, Oxford, 1999.

[68] B. J. Alder, W. G. Hoover, and T. E. Wainwright. *Phys. Rev. Lett.*, 11:241, 1963.

[69] X. H. Zheng and J. C. Earnshaw. *Europhys. Lett.*, 41(6):635, 1998.

[70] J. Acrivos. *J. Rheol.*, 39:813, 1995.

[71] A. Sierou and J. F. Brady. *J. Fluid. Mech.*, 506:258, 2004.

[72] R. Simon, T. Palberg, and P. Leiderer. *J. Chem. Phys.*, 99 (4):3030, 1993.

[73] A. Imhof, A. van Blaaderen, G. Maret, J. Mellema, and J. K. G. Dhont. *J. Chem. Phys.*, 100 (3):2170, 1994.

[74] A. van Blaaderen, J. Peetermans, G. Maret, and J. K. G. Dhont. *J. Chem. Phys.*, 96 (6):4591, 1992.

[75] M. Das, S. Ramaswamy, and G. Ananthakrishna. *Europhys. Lett.*, 60(4):636, 2002.

[76] M. Dijkstra. *Phys. Rev. Lett.*, 93 (10):108303, 2004.

[77] A. Onuki. *Phase Transition Dynamics*. Cambridge University Press, Cambridge, 2002.

[78] T. Hashimoto, K. Matsuzaka, E. Moses, and A. Onuki. *Phys. Rev. Lett.*, 74 (1):126, 1995.

[79] N. A. M. Verhaegh, J. S. van Duijneveldt, J. K. G. Dhont, and H. N. W. Lekkerkerker. *Physica A*, 230:409, 1996.

[80] E. D. Siggia. *Phys. Rev. A*, 20:595, 1979.

[81] J. K. G. Dhont and W. J. Briels. *Phys. Rev. E*, 72:031404, 2005.

[82] A. Onuki. *J. Phys.: Condens. Matter*, 9:6119, 1997.

[83] C. C. Han, Y. Yao, R. Zhang, and E. K. Hobbie. *Polymer*, 47:3271, 2006.

[84] N. Lorén, A. Alstkär, and A. M. Hermansson. *Macromolecules*, 34:8117, 2001.

[85] H. Tanaka. *J. Phys.: Condens. Matter*, 12:R207, 2000.

[86] D. G. A. L. Aarts, R. P. A. Dullens, and H. N. W. Lekkerkerker. *New Journal of Physics*, 7 (3):40, 2005.

[87] K. Fujioka, T. Takebe, and T. Hashimoto. *J. Chem. Phys.*, 98 (1):717, 1993.

[88] D. G. A. L. Aarts and H. N. W. Lekkerkerker. *J. Phys.: Condens. Matter*, 16:S4231, 2004.

[89] D. G. A. L. Aarts, M. Schmidt, and H. N. W. Lekkerkerker. *Science*, 304:847, 2004.

[90] S. Tomotika. *Proc. Roy. Soc. Lond. Series A*, 150:322, 1935.

[91] E. H. A. de Hoog and H. N. W. Lekkerkerker. *J. Chem. Phys. B*, 105:11636, 2001.

[92] V. G. Levich. *Physicochemical Hydrodynamics*. Dekker, New York, 1962.

[93] M. von Smoluchowski. *Ann. Phys.*, 25:205, 1908.

[94] L. Mandelstam. *Ann. Phys.*, 41:609, 1913.

[95] D. G. A. L. Aarts, H. N. W. Lekkerkerker, Hua Guo, G. H. Wegdam, and D. Bonn. *Phys. Rev. Lett.*, 95:164503, 2005.

[96] M. E. Cates and S. T. Milner. *Phys. Rev. Lett.*, 62:1856, 1989.

[97] R. Bruinsma and Y. Rabin. *Phys. Rev. A*, 45:994, 1992.

[98] J. Yamamoto and H. Tanaka. *Phys. Rev. Lett.*, 74:932, 1995.

[99] J. Yamamoto and H. Tanaka. *Phys. Rev. Lett.*, 77:4390, 1996.

[100] K. A. Koppi, M. Tirrell, and F. S. Bates. *Phys. Rev. Lett.*, 70:1449, 1993.

[101] A. G. Zilman and R. Granek. *Eur. Phys. J. B*, 11:593, 1999.

[102] D. Langevin. *Light Scattering by Liquid Surfaces and Complementary Techniques.* Prentice-Hall, Englewood Cliffs, New Jersey, 1992.

[103] T. Seydel, A. Madsen, M. Tolan, G. Grübel, and W. Press. *Phys. Rev. B*, 63:073409, 2001.

[104] G. A. Vliegenthart and H. N. W. Lekkerkerker. *Prog. Colloid Polym. Sci.*, 105:27, 1997.

[105] E. H. A. de Hoog and H. N. W. Lekkerkerker. *J. Phys. Chem. B*, 103:5274, 1999.

[106] D. G. A. L. Aarts, J. H. van der Wiel, and H. N. W. Lekkerkerker. *J. Phys.: Condens. Matter*, 15:S245, 2003.

[107] S. W. Marlow and P. D. Olmsted. *Phys. Rev. E*, 66:061706, 2002.

[108] B. Vincent. *Colloids Surf.*, 50:241, 1990.

[109] G. C. Berry. *J. Chem. Phys.*, 44:4550, 1966.

[110] B. R. McClain, D. D. Lee, B. L. Carvalho, S. G. J. Mochrie, S. H. Chen, and J. D. Litster. *Phys. Rev. Lett.*, 72:246, 1994.

[111] U.-S. Jeng, L. Esibov, L. Crow, and A. Steyerl. *J. Phys.: Condens. Matter*, 10:4955, 1998.

[112] J. D. van der Waals. *Z. f. Phys. Chem.*, 13:657, 1894.

[113] F. P. Buff, R. A. Lovett, and F. H. Stillinger. *Phys. Rev. Lett.*, 15:621, 1965.

[114] R. Blaak, S. Auer, D. Frenkel, and H. Löwen. *Phys. Rev. Lett.*, 93:068303, 2004.

[115] L. D. Landau and E. M. Lifshitz. *Fluid Mechanics.* Pergamon Press, Oxford, 1975.

[116] G. J. Vroege and H. N. W. Lekkerkerker. *Rep. Prog. Phys.*, 55:1241, 1992.

[117] P. Bolhuis and D. Frenkel. *J. Chem. Phys.*, 106(2):666, 1997.

[118] H. Graf and H. Löwen. *Phys. Rev. E*, 59(2):1932, 1999.

[119] R. F. Kayser and H. J. Raveché. *Phys. Rev. A*, 17:2067, 1978.

[120] J. Viamontes and J. X. Tang. *http://arxiv.org/abs/cond-mat/0506813*, 2005.

[121] M. P. B. van Bruggen, J. K. G. Dhont, and H. N. W. Lekkerkerker. *Macromolecules*, 32:2256, 1999.

[122] T. A. J. Lenstra, Z. Dogic, and J. K. G. Dhont. *J. Chem. Phys.*, 114(22), 2001.

[123] J. Tang and S. Fraden. *Phys. Rev. Lett.*, 71(21):3509, 1993.

[124] B. J. Lemaire, P. Davidson, J. Ferré, J.-P. Jamet, D. Petermann, P. Panine, I. Dozov, D. Stoenescuc, and J.-P. Jolivet. *Faraday Discuss.*, 128:271, 2005.

[125] S. Fraden. *Observation, Prediction, and Simulation of Phase Transitions in Complex Fluids*, volume 460. Kluwer Academic Publishers, Dordrecht, The Netherlands, 1995.

[126] Z. Y. Chen. *Macromolecules*, 26:3419, 1993.

[127] Z. Dogic, K. R. Purdy, E. Grelet, M. Adams, and S. Fraden. *Phys. Rev. E*, 69:051702, 2004.

[128] J. K. G. Dhont and W. J. Briels. *Colloid Surface A*, 213(2-3):131, 2003.

[129] M. P. Lettinga, K. Kang, P. Holqvist, A. Imhof, D. Derks, and J. K. G. Dhont. *Phys. Rev. E*, 73:011412, 2006.

[130] Z. Dogic. *Phys. Rev. Lett.*, 91(16):165701, 2003.

[131] A. Nakai, T. Shiwaku, W. Wang, H. Hasegawa, and T. Hashimoto. *Macromolecules*, 29:5990, 1996.

[132] T. Araki and H. Tanaka. *Phys. Rev. Lett.*, 93(1):015702, 2004.

[133] J. Fukuda. *Phys. Rev. E*, 59(3):3275, 1999.

[134] P. Prinsen and P. van der Schoot. *Phys. Rev. E*, 68:021701, 2003.

Summary

This thesis deals with colloidal suspensions in shear flow. These suspensions consist of (sub)micron-sized solid particles dispersed in a continuous liquid phase. In this work, the effect of shear flow on the microstructure of these soft matter systems is investigated by means of microscopy. For our investigations we use systems of nearly equal sized particles whose interactions are determined by their size, shape, charge, and are further tuned by additives like polymers or salt. In the first Chapter, the three model systems under study are introduced, i.e.: hard-spheres, attractive spheres, and (attractive) rods. Furthermore, here we discuss the synthesis method of the extensively used poly(methyl methacrylate) spheres, and present the working principle of confocal microscopy.

Recently, a new type of shear cell was developed to study flowing suspensions in real space. The key property of this set up is the counter rotating principle of the cone and plate, opening up the possibility to create a stationary layer in the bulk of the cell. In Chapter 2, we elaborate on the details of this setup and its performance. Fluorescence confocal microscopy is used to visualize the sheared suspension, and allows imaging individual particles in a stationary plane for a prolonged time. Moreover, this plane of zero velocity can be moved in the velocity gradient direction while keeping the shear rate $\dot{\gamma}$ constant.

Using this shear cell, the particle positions in a layer of a sheared colloidal crystal can be tracked. The particle dynamics in such a crystal in shear flow is the subject of Chapter 3. Here, the particles interact through a (nearly) hard sphere potential. Our real space observations confirm the alignment of the crystal in the shear field and the collective zig-zag motion, which were also deduced from early scattering experiments. On top of this, we find that random particle displacements increase with shear rate. Those increased fluctuations result in shear induced melting when their root mean square displacement has reached about 13 % of the particle separation. This melting transition is accompanied by local rearrangements that become more and more pronounced with increasing shear rate.

Apart from hard spheres, we investigate mixtures of colloids and polymers in shear flow. The polymers cause an effective attraction between the spheres, which leads to phase separation into a colloid rich (polymer poor) and a colloid poor (polymer rich) phase at sufficiently high colloid and polymer concentration. In Chapter 4, we study the demixing process in the (spinodal) two phase region of

the phase diagram. The system is quenched from an initially almost homogeneous state at very high shear rate to a low shear rate. A spinodal decomposition pattern is observed. Initially, the characteristic length scale increases linearly with time. As the structure coarsens, shear imposes a certain length scale onto the structure and a clear asymmetry occurs. The domains become highly stretched along the flow direction, and the domain width along the vorticity axis reaches a stationary size, which scales as $\dot{\gamma}^{-1/3}$.

In the final stage of phase separation the denser colloidal liquid phase settles on the bottom of the cell, while the gas phase floats on top. The interface between these phases is the topic of Chapter 5. We investigated the thermal fluctuations of the colloidal gas-liquid interface subjected to a shear flow parallel to the interface. Strikingly, we find that the shear strongly suppresses capillary waves, making the interface smoother. This phenomenon can be described by introducing an effective interfacial tension that increases with shear rate. We show that this can be explained as a loss of interfacial entropy caused by the flow, which affects especially the slow fluctuations.

Finally, we consider the demixing process in systems of attractive rods (Chapter 6). A mixture of rod-like viruses (*fd*) and polymer (dextran) is quenched from a flow-induced fully nematic state into the region where the nematic and the isotropic phase coexist (at zero shear). Dependent on the concentration of rods we observe either demixing by nucleation-and-growth (high concentration) or spinodal decomposition (low concentration). At intermediate concentrations we see the transition between both types of demixing processes. At this concentration we locate the spinodal point.

Samenvatting voor iedereen

Het thema van dit proefschrift is, zoals samengevat in de titel, “colloïdale suspensies in afschuifstroming”. Traditionele voorbeelden van colloïdale suspensies zijn melk of verf, en het doorgronden van hun eigenschappen en het gedrag wanneer ze stromen is dan ook van belang in bijvoorbeeld de verf- en zuivelindustrie. Meer tot de verbeelding spreken waarschijnlijk (toekomstige) high-tech toepassingen, die liggen op het gebied van de fotonica waar men schakelingen voor licht (in plaats van electronen) probeert te realiseren, en in de wereld van de microfluïdica waar men op *micro*schaal gebruik maakt van vloeistofstrominkjes, bijvoorbeeld voor gebruik in sensoren. De vragen die we in dit proefschrift beantwoorden leiden niet direct tot deze toepassingen, maar zijn van meer fundamentele aard. Onze motivatie komt voor een groot deel ook voort uit nieuwsgierigheid, de mogelijkheid om in deze niet-evenwicht systemen nieuwe structuren of gedrag te kunnen waarnemen en, tenslotte, de uitdaging om dit te kunnen verklaren.

Colloïdale suspensies bestaan uit deeltjes van ongeveer een micrometer (eenduizendste millimeter) groot, die rondzweven in een moleculaire vloeistof, bijvoorbeeld water. In je bloed zijn het bloedcellen die ronddobberen, in melk zijn het kleine vetdruppeltjes en in ons geval zijn het plexiglazen bolletjes. Anders dan in melk of bloed zijn de bollen in ons systeem allemaal even groot. Bovendien kunnen we door het toevoegen van zout of polymeren afstemmen hoe de deeltjes met elkaar wisselwerken. Hierdoor kunnen de verschillende colloïdale modelsystemen gerealiseerd worden, die we in dit proefschrift tegenkomen. In hoofdstuk **??** introduceren we deze modelsystemen. Ook gaan we in dit hoofdstuk in op de chemische synthese waarmee we de plexiglazen bollen maken en van een fluorescente kleurstof voorzien. Dit laatste vergroot de mogelijkheden om deze deeltjes met een geavanceerde (fluorescentie) microscoop af te beelden en te bestuderen.

Doordat colloïden veel groter en trager zijn dan moleculen is de structuur van een colloïdaal systeem gemakkelijker van buitenaf te manipuleren. In dit onderzoek doen we dat door het aanleggen van een afschuifstroming. Een eenvoudige manier om dit te doen is door de wanden van de container waarin de vloeistof zich bevindt in beweging te brengen. Door de wrijving met de wand en stroperigheid van de vloeistof wordt deze als het ware meegesleept en ontstaat er een stroming. Dit gebeurt bijvoorbeeld als je een vloeistof tussen twee parallelle platen brengt en die platen vervolgens ten opzichte van elkaar gaat schuiven.

Voor ons onderzoek gebruiken we een speciaal ontworpen cel waarin zulke afschuifstroming nauwkeurig aangelegd kan worden en waarin we tegelijkertijd met de microscoop kunnen kijken wat er aan de structuur verandert (zie figuur 2.1 en 2.2). Het tweede hoofdstuk gaat vooral over de werking en de mogelijkheden van deze opstelling. In feite zijn het in ons geval niet twee platen die schuiven, maar een (metalen) kegel en (glas)plaat die in tegengestelde richting rond dezelfde as draaien. Een belangrijke eigenschap van deze opstelling is dat de rotatiesnelheid van zowel de glasplaat als de kegel ingesteld kan worden, zodat er op de gewenste hoogte in de cel een laag is die niet uit het beeld van de microscoop verdwijnt. In deze laag kunnen we de colloïden gedurende een lange tijd volgen. Dit biedt de mogelijkheid om het effect van de stroming op deeltjesniveau te bestuderen.

In hoofdstuk 3 gaan we in op wat er gebeurt als een geordende stapeling van colloïden (een colloïdaal kristal) in zo'n afschuifstroming wordt gebracht. We laten zien hoe de verschillende kristallijne lagen dan over elkaar heen bewegen. Daarbij ontwijken ze deeltjes uit de aangrenzende lagen, wat uiteindelijk resulteert in een zig-zag beweging (figuur 3.2). Ook zijn we geïnteresseerd in hoe en wanneer een dergelijk colloïdaal kristal overgaat in een wanordelijke fase. Kristallen van micrometer-grote plexiglas bollen smelten namelijk zodra er een voldoende hoge afschuifstroming aangelegd wordt. We kunnen dit verklaren doordat de posities van de afzonderlijke bollen −de bouwstenen van het kristal− zodanig grote fluctuaties vertonen, dat het bouwwerk ineenstort. Het blijkt dat het smeltcriterium van een uit evenwicht gebracht colloïdaal kristal verrassende gelijkenis vertoont met dat in moleculaire (evenwichts)systemen.

We vervolgen het onderzoek met het bestuderen van mengsels van colloïden en polymeren (ijle kluwens van ketens). De aanwezigheid van deze polymeren veroorzaakt een effectieve aantrekking tussen de colloïden, waardoor het systeem zich spontaan opsplitst in een fase met veel colloïden en een andere fase met weinig colloïden. In analogie met bijvoorbeeld water en waterdamp, noemen we de colloïd-rijke fase de colloïdale vloeistof en de colloïd-arme fase het colloïdale gas. In hoofdstuk 4 bekijken we de manier waarop het ontmengingsproces plaatsvindt in de aanwezigheid van stroming. Hiertoe brengen we het mengsel eerst in een zodanig snelle stroming dat het zo goed als homogeen wordt. Vervolgens verlagen we de stroomsnelheid aanzienlijk. Het ontmengingsproces blijkt sterk beïnvloed te worden door de stroming: de gas- en vloeistofdomeinen strekken zich uit in de richting van de stroming, tot er een stationaire toestand bereikt wordt. De stroming stabiliseert deze langgerekte structuren. Hoe hoger de stromingssnelheid, hoe langer en dunner de domeinen (zie figuur 4.4).

Als het systeem helemaal ontmengd is, bevindt de zwaardere colloïdale vloeistof zich op de bodem van de cel en daarbovenop drijft het colloïdale gas. Het grensvlak tussen deze twee fasen, dat door de temperatuur altijd in beweging is, is het onderwerp van hoofdstuk 5. De opmerkelijke waarneming die we in dit colloïdale gas-vloeistof systeem doen, is dat stroming deze thermische fluctuaties (zogenaamde capillaire golven) afvlakt (zie figuur 5.1), in tegenstelling tot wind die over een wateroppervlak waait. Een manier om dit te begrijpen is de volgende: in afwezigheid van stroming uit het vrij fluctueren van capillaire golven zich in een lage grensvlakspanning. In het geval van stroming wordt het traagste deel van de golven verhinderd om vrij te fluctueren. Dit kan vervolgens uitgedrukt worden in een effectief grotere grensvlakspanning, wat het gladder vloeistofoppervlak verklaart.

In het voorafgaande waren de colloïden allemaal bolvormige deeltjes. In het laatste hoofdstuk bekijken we echter een systeem dat bestaat uit kleine staafjes. In tegenstelling tot de plexiglazen bollen, zijn dit biologische systemen; namelijk virussen die gekweekt worden door een kolonie van bacteriën te infecteren. Het grote verschil met suspensies van bolvormige deeltjes is dat in zulke anisometrische systemen ook de orientatie van de deeltjes van belang is. Suspensies van colloïdale staafjes kunnen, afhankelijk van de concentratie, ofwel allemaal een willekeurige orientatie aannemen (isotrope fase), ofwel oplijnen in een bepaalde richting (nematische fase). In een bepaald concentratiegebied komen beide fasen tegelijkertijd voor. In dit tweefase-gebied doen wij onze experimenten. Door het aanleggen van een afschuifstroming kunnen we het *gehele* systeem toch in een opgelijnde toestand brengen. Vervolgens bekijken het ontmengingsproces als de stroming gestopt wordt. Er zijn twee verschillende manieren waarop het systeem kan ontmengen (zie figuur 6.2). Welk scenario er gevolgd wordt, is afhankelijk van de concentratie staven en wordt bepaald door de vraag of de opgelijnde fase instabiel danwel meta-stabiel is in afwezigheid van stroming. Deze experimenten geven daarom informatie over het evenwichtsfasegedrag van suspensies van staven, dat zonder het aanleggen van een stroming veel lastiger toegankelijk zou zijn.

List of Publications

This thesis is based on the following publications:

- D. Derks, H. Wisman, A. van Blaaderen and A. Imhof
  Confocal microscopy of colloidal dispersions in shear flow using a counter-rotating cone-plate shear cell
  Journal of Physics: Condensed Matter **16** (38), S3917-S3927 (2004).
  (Chapter 2)

- D. Derks, A. van Blaaderen and A. Imhof
  Real space study of the dynamics in sheared colloidal crystals
  in preparation.
  (Chapter 3)

- D. Derks, D. G. A. L. Aarts and A. Imhof
  Interfacial dynamics in phase separating colloid polymer mixtures under shear
  in preparation.
  (Chapter 4)

- D. Derks, D. G. A. L. Aarts, D. Bonn, H. N. W. Lekkerkerker, and A. Imhof
  Suppression of thermally excited capillary waves by shear flow
  Physical Review Letters **97**, 038301 (2006).
  (Chapter 5)

- M. P. Lettinga, K. Kang, A. Imhof, D. Derks, and J. K. G. Dhont
  Kinetic pathways of nematic-isotropic phase transition as studied by confocal microscopy on rod-like viruses
  Journal of Physics: Condensed Matter **17** (45), S3609-S3618 (2005).
  (Chapter 6)

Other publications:

- M. P. Lettinga, K. Kang, P. Holmqvist, A. Imhof, D. Derks, and J. K. G. Dhont
  Nematic-isotropic spinodal decomposition kinetics of rod-like viruses
  Physical Review E **73**, 011412 (2006).

- A. Lindner, D. Derks and M. J. Shelley
  Stretch flow of thin layers of Newtonian liquids: Fingering patterns and lifting forces
  Physics of Fluids **17** (7), 072107 (2005).

- R. P. A. Dullens, M. Claesson, D. Derks, A. van Blaaderen and W. K. Kegel
  Monodisperse core-shell poly(methyl methacrylate) latex colloids
  Langmuir **19** (15), 5963-5966 (2003).

- D. Derks, A. Lindner, C. Creton and D. Bonn
  Cohesive failure of thin layers of soft model adhesives under tension
  Journal of Applied Physics **93** (3), 1557-1566 (2003).

- J. P. Hoogenboom, D. Derks, P. Vergeer and A. van Blaaderen
  Stacking faults in colloidal crystals grown by sedimentation
  Journal of Chemical Physics **117** (24), 11320-11328 (2002).

Dankwoord

Finalement! Dit is dan het moment om alle fantastische mensen te bedanken die me de afgelopen jaren op wat voor manier dan ook hebben geholpen om dit boekje tot stand te brengen. Ik kijk terug op een hele mooie tijd in Utrecht, en dat heb ik voor het grootste deel te danken aan zulke geweldige vrienden en collega's.

In het bijzonder wil ik Arnout Imhof hartelijk danken. Als co-promotor en dagelijks begeleider, ben je natuurlijk heel dicht bij mijn bezigheden betrokken geweest. Ik waardeer het heel erg dat ik altijd bij je kon binnenlopen, tot en met de laatste dag. Dank voor je enorme opgeruimdheid (in alle betekenissen van het woord). Zeker het laatste jaar was je de perfecte begeleider voor een promovendus die bekend staat om haar −net te laat, is op tijd genoeg− motto. Op deze plek wil ik ook graag mijn promotor Alfons van Blaaderen bedanken: Alfons, dankjewel voor alle nuttige bijdragen die je, iets meer op de achtergrond, geleverd hebt. Ik heb grote bewondering voor de manier waarop je in de loop der jaren zulke geweldige groep om je heen verzameld hebt en het was een hele mooie ervaring om daarvan deel te hebben uitgemaakt.

Samenwerken is veel en veel leuker dan alleen. Zeker, als de persoon in kwestie Dirk Aarts heet. Dirk, wat ben ik blij dat we op een dag onze krachten hebben gebundeld en 'jouw' colloid-polymeer mengsel in 'mijn' shear cell hebben gekiept. Uiteindelijk vormden deze experimenten de basis van een aanzienlijk deel van dit proefschrift en ik wil je dan ook hartelijk danken voor jouw (belangrijke) aandeel hierin. Behalve van het werk, heb ik ook genoten van onze activiteiten daarnaast: ik zou geen van de ontelbare telefoontjes, etentjes en squash-partijtjes (behalve dan de $> 9-0$s) hebben willen missen. Samenwerken deed ik ook met drie fantastische mensen uit Jülich: Jan Dhont, Pavlik Lettinga, en Kyong Kang. Ik noemde zonet dan wel 'mijn' shear cell, maar de eerste drie jaar gebruikte ik eigenlijk die van jullie. Heel veel dank voor het lenen van deze hoofdrolspeler van dit proefschrift. Verder bewaar ik goede herinneringen aan onze gemeenschappelijke metingen: met z'n vieren achter één microscoop... zo gezellig was het alleen als jullie er waren. In het bijzonder dank ik Pavlik, zonder jou was een niet-bollen-hoofdstuk absoluut onmogelijk geweest.

Verder dank ik ook Henk Lekkerkerker. Ik vind het heel mooi dat je via de shear-experimenten aan grensvlakken ook een beetje bij dit proefschrift betrokken raakte. Onze wegen kruisten elkaar natuurlijk al eerder, en dat die weg in mijn geval in de richting van (−terug-en-weer-naar−) Parijs leidde, heb ik mede aan jouw advies te danken. Hartelijk dank daarvoor. En dat brengt me vanzelf bij Daniel Bonn. Daniel, dank je wel voor je betrokkenheid en aanstekelijk enthousiasme, ook tijdens mijn promotietijd. Nu ga ik weer terug naar het honk, waaraan ik vijf jaar geleden al verslingerd geraakt ben. Geweldig, dat je het allemaal mogelijk hebt gemaakt.

De afgelopen jaren werden opgeluisterd door het aangename gezelschap van verschillende kamergenoten. Het was gezellig bij ons in OL018, en het schijnt dat onze buren dat kunnen bevestigen... Af en toe een (a)muzikale uitspatting moet kunnen en gelukkig behoort dit tot één van de vele talenten van Mirjam Leunissen. Mirjam, het was me een waar genoegen. Volgens mij hadden we een perfecte balans tussen zinnige en onzinnige (maar altijd vermakelijke) conversaties te pakken. Al vóór dag één legden we een goede basis door onze onvergetelijke reis naar Boulder, Colorado. Nu, alweer vier jaar later, wens ik je heel veel succes met het afronden van je proefschrift. Ik ben bij voorbaat al erg benieuwd naar je New-York-avonturen. Krassimir Velikov, our time as officemates was short, but fortunately we always meet at cheerful occasions... Let's keep that tradition in honor! Dirk Vossen, dank je wel voor al je wijze raad, die ik jammer genoeg niet opgevolgd heb... (zodat ik nu in blessuretijd dit dankwoord zit te typen). Finally, Ahmet Faik Demirôrs, thanks for supporting me the last couple of months. Go on as you started, I think you're doing great!

In en om het Ornsteinlab bevonden zich vele mensen van wie op uiteenlopende gebieden veel te leren viel. Om te beginnen dank ik Carlos van Kats, die me snel en vakkundig inwijdde in de geheimen (en mysteries) van het brouwen van PMMA. Carlos, jij bent niet alleen de spil van ons chemisch lab, maar ook van een groot deel van het sociale gebeuren rond de hele groep. Kortom, je bent een top-collega en dat is heel wat waard (250 euro namelijk...). Over bollenbakken gesproken, dat is ook een mooie aanleiding om Roel Dullens te bedanken (cursus voor gevorderen). Roel, daarnaast ook bedankt voor alle andere (vaak data-analyse gerelateerde) discussies en hulp. Maar het allermeest dank ik je voor je bemoedigende woorden en schouderklopjes, altijd precies op het goeie moment. From the simulation and theory side, I'd like to thank Andrea Fortini, Jos Zwanikken and René van Roij for all our nice discussions about interfaces in flow. Andrea, I'm curious what your simulation results will further learn us.

Dan zijn er heel veel labgenoten, en oudlabgenoten, die allemaal hebben bijgedragen aan een hele goeie werksfeer. In het bijzonder noem ik Carmen Zoldesi (lekker belangrijk! zo'n proefschrift...). Echt super om straks samen met jou een feestje te bouwen. De gezamenlijke voorpret had ik alvast niet willen missen. Christina Christova, your sweet support meant a lot to me. Paddy Royall, many thanks for all the good times we spend together, both when you were still in Utrecht and during your visits. Yu Ling Wu, my partner in shear: we zijn nog lang niet uitgepraat over bananen en kamelen... Shear ze!! Astrid van der Horst, wat een tijd, hè.. Alvast alle geluk toegewenst in Canada! Joan Penninkhof, Esther Vermolen, Peter van Oostrum, Marjolein Dijkstra, Job Thijssen, Dannis 't Hart, Antti-Pekka Hynninen, Patrick Johnson, Matthias Schmidt, (and a little bit of) Teun Vissers, Andy Campbell, Slava Savenko, Alejandro Cuetos, Eduardo Sanz, Michiel Hermes, Matthieu Marechal, Catherine Quilliet, Jacob Hoogenboom, Alexander Moroz, Christina Graf, (bijna groepsgenoot) Dave van den Heuvel, en María Delgado Flores, ook jullie wil ik allemaal hartelijk bedanken!

Mijn experimenten zouden niet mogelijk geweest zonder mensen voor de techniek en er zijn er velen die me op verschillende momenten geholpen hebben. Vaak was het Hans Wisman die met raad en daad veel probleempjes oploste. Klasse, Hans. Soms was het ook Gerard van Lingen, vooral als het ging om het grove werk als er weer 'ns iets rigoreus vastgelopen was (m'n fiets incluis). Ik dank ook de Instrumentele Groep Fysica: met name Joost en Jos, Mari en Gerard. Ik sta elke keer weer verbaasd van wat jullie allemaal kunnen tekenen en maken. Op deze plek wil ik ook Yves Nicolas, Marcel Paques en Els de Hoog van het Wageningen Centre for Food Science, de bakermat van de shear cell, bedanken.

Met mijn 'roots' als Utrechts chemicus, heb en hou ik natuurlijk altijd een zwak voor het Van 't Hoff lab en zijn bewoners: Bedankt dat jullie me ook een beetje deel van jullie club lieten voelen... Ook toen Dirk en Roel vertrokken, waren er altijd nog Volkert, Maurice, Stefano, Mark en Willem. Het zelfde geldt eigenlijk voor de bovenburen van de Condensed Matter and Interfaces groep: Floris, Peter, Sander, Arjan, Rianne, Paul, John en natuurlijk Hans. Dankjulliewel allemaal. Speciaal wil ik nog Rik Wensink en Floris van Driel noemen: het was een eer om jullie paranimf te zijn.

Ten slotte, dank ik ook (de rest van) mijn dierbare vrienden (onder andere Eveline, Salima, Marieke, Felix, Gabby, Maryam, Anke...), met wie ik van harte hoop de 27e een heel mooi feestje te vieren. Speciale dank gaat uit naar Lisa Janssen voor onze waardevolle vriendschap. Fijn dat je mijn paranimf wilt zijn!! En dat geldt ook voor jou, Huub. Lieve broer: je bent een held (...), en ik vind het super dat je straks achter mij staat. Verder, dank ik mijn (voltallige) surrogaatfamilie van de Biltstraat. En natuurlijk mijn echte familie: lieve Pap en Mam, Koos en Huub, dank voor alle vertrouwen en het bieden van zo'n warme thuishaven in het zuiden des lands. Keifijn, dat jullie zo mee hebben geleefd.

Didi

Curriculum Vitae

De auteur van dit proefschrift werd geboren op 29 augustus 1978 te Oploo. Vanaf 1990 bezocht zij “Scholengemeenschap Jerusalem” in Venray. In 1996 werd het gymnasium diploma behaald aan deze school, die inmiddels gefuseerd was tot Raayland College. In september van dat jaar werd begonnen aan een studie scheikunde aan de Universiteit Utrecht. In augustus 2001 studeerde zij (cum laude) af met als hoofdvak vaste stof chemie en bijvak fysische en colloïd chemie. Tevens werd tijdens haar studie zes maanden onderzoek gedaan aan de Ecole Normale Supérieure in Parijs in het kader van een Erasmus project. Dit project werd na het afstuderen voortgezet tot februari 2002.

In maart 2002 trad de auteur als onderzoeker in opleiding in dienst van de Stichting voor Fundamenteel Onderzoek der Materie (FOM). Het promotieonderzoek werd uitgevoerd in de Soft Condensed Matter groep van het departement Natuur- en Sterrenkunde aan de Universiteit Utrecht. De resultaten van dit onderzoek, waaraan zij onder begeleiding van dr. Arnout Imhof en prof. dr. Alfons van Blaaderen werkte, staan beschreven in dit proefschrift. Vanaf oktober 2006 gaat de auteur aan de slag als post-doctoraal onderzoeker aan het Laboratoire de Physique Statistique van de Ecole Normale Supérieure te Parijs.